Towards entanglement generation between Cesium-133 atomic ensemble and nanomechanical membrane resonator

M.Sc. Physics
Master Thesis

Marius Gaudesius

QUANTOP, Niels Bohr Institute
University of Copenhagen

December 1st, 2015

Supervisor: Prof. Eugene S. Polzik

Abstract

This thesis presents an experimental setup that can be used for entanglement generation between Cesium-133 atomic ensemble and nanomechanical membrane resonator, and measurements performed on this setup that demonstrate how by coupling the two systems one is led to reduction of classical light back-action noise of the measurement. Measurements of this kind define the very first steps on our group's quest towards atom-membrane entanglement. In addition, experimental work characterizing the atomic part of this setup is presented.

Acknowledgments

The following acknowledgments are in order:

1. To Eugene Simon Polzik for opening the door and welcoming me to the club.

2. To Georgios "MacGyver" Vasilakis for always finding time to answer all sorts of weird questions and ... for being a MacGyver.

3. To Kasper Jensen for being knowledgeable about the lab's experiments and the theory surrounding them.

4. To Rodrigo Adriano Thomas for finding ways of being confusing in a good sense of the word and for being a motivated person.

5. To Anne Fabricant for always being helpful around the lab.

6. To Christoffer Bo Møller for being an expert in optomechanics.

6. To Bing Chen, Boris Albrecht, Karsten Bjerrum Dideriksen, Heng Shen, Yeghishe Tsaturyan, Michael Viktor Alban Zugenmaier, William Hvidtfelt Padkær Nielsen for being the homeboy crew.

7. ... and the rest of the QUANTOP group for being quantum and optical.

The data seen in figures 21, 22 and 23 was plotted by Georgios Vasilakis, Rodrigo Adriano Thomas and Christoffer Bo Møller, and for that I would like to acknowledge this work.

Table of contents

Introduction

Through technological advances sensitivity of measurements of e.g. gravitational waves, distance, and time shift is approaching the standard quantum limit (SQL) set by the Heisenberg uncertainty principle. Overcoming the SQL would, in principle, lead to measurements with vanishing uncertainty. Among the ideas surrounding SQL-circumventing measurement schemes we can find ones that are based on e.g. quantum variational measurements [37], two-tone measurements [40], or use of non-classically correlated light [38, 39].

This thesis considers a protocol proposed by K. Hammerer et al. [12], dealing with entanglement generation between Cesium-133 atomic ensemble and nanomechanical membrane resonator. Succeeding in entanglement generation between these two systems can find applications in measurements of acceleration and magnetic fields below the SQL [13].

The work presented in this thesis is divided into four main chapters.

Chapter 1 presents a theoretical basis serving to explain the atom-membrane entanglement protocol [12], which is also presented in chapter 2.

Chapter 2 presents the entanglement protocol. In this chapter it is seen how the entanglement protocol reveals practical considerations common to experimental systems that in principle can be used for satisfying the entanglement protocol.

Chapter 3 describes the main experimental components of our group's owned experimental setup that, via laser light, interfaces a Cesium-133 atomic ensemble contained inside our specially designed microcells and our specially designed nanomechanical membrane resonator that is part of a cryogenic optomechanical system. This is done in order to see how good our setup can be at tackling the practical considerations implied by the entanglement protocol. A big focus in this thesis is put on the atomic part of the atom-membrane interfacing experimental setup, and for that reason experiments characterizing this part of the setup are presented.

Chapter 4 explains why our atom-membrane interfacing experimental setup can allow us to satisfy the entanglement protocol, and also presents and explains measurements done using this setup. It is demonstrated how by coupling the two systems we are led to reduction of classical light back-action noise of the measurement. Measurements of this kind define the very first steps on our quest towards atom-membrane entanglement.

In the *summary of the main results and outlook* I summarize the main results of the thesis and give an outlook on the future of our atom-membrane entanglement experiment.

Chapter 1: Light's interaction with Cesium-133 atomic ensemble, and cavity optomechanics

In this chapter I present the necessary theory related to the protocol described in chapter 2, dealing with entanglement generation between Cesium-133 atomic ensemble and nanomechanical membrane resonator.

The first half of this chapter deals with the quantum nature of light's interaction with Cesium-133 atomic ensembles, and the second half of this chapter deals with the quantum nature of light's interaction with a mechanical resonator that is part of a cavity optomechanical system.

The main result of the first half of this chapter is summarized by the propagation equations showing the interplay between operators characterizing the quantum nature of respectively Cesium-133 atoms and light, and the main result of the second half of this chapter is summarized by the input-output relations for operators that describe light that is transmitted by a cavity optomechanical system.

1.1 The energy structures of the ground and the first excited state of a Cesium-133 atom

In this section I will describe the energy structures of the ground and the first excited state of a Cesium-133 atom, which is the only stable isotope of a Cesium atom, and is an alkali atom, which is an atom characterized by having a single valence electron.

In order to be able to describe the energy structures of the ground and the first excited state of (the valence electron of) a Cesium-133 atom, let us first understand how the electron spin angular momentum operator $\hat{\mathbf{s}}$ couples to the electron orbital angular momentum operator $\hat{\boldsymbol{\ell}}$, and also how the electron total angular momentum operator $\hat{\mathbf{j}}$ couples to the nuclear total angular momentum operator $\hat{\mathbf{i}}$, and what the respective couplings result in.

The magnetic interaction between the magnetic dipole moment operators associated with, respectively, the operator $\hat{\mathbf{s}}$ and the operator $\hat{\boldsymbol{\ell}}$ results in an energy splitting of the gross energy levels into the fine structure energy levels. The electron total angular momentum operator $\hat{\mathbf{j}}$ and the electron total angular momentum quantum number j then satisfy the relations

$$\hat{\mathbf{j}} = \hat{\boldsymbol{\ell}} + \hat{\mathbf{s}} \quad , \tag{1.1.1.a}$$

$$\mathrm{j} = |\ell - \mathrm{s}|, |\ell - \mathrm{s}| + 1, \dots, \ell + \mathrm{s} \quad , \tag{1.1.1.b}$$

where s is the electron spin angular momentum quantum number, and ℓ is the electron orbital angular momentum quantum number.

The magnetic interaction between the electron and the nucleus couples the operator $\hat{\mathbf{j}}$ with the operator $\hat{\mathbf{i}}$ and results in an energy splitting of the fine structure energy levels into the hyperfine structure energy levels. The atomic total angular momentum operator $\hat{\mathbf{f}}$ and the atomic total angular momentum quantum number f then satisfy the relations

$$\hat{\mathbf{f}} = \hat{\mathbf{j}} + \hat{\mathbf{i}} \quad , \tag{1.1.2.a}$$

$$\mathrm{f} = |\mathrm{j} - \mathrm{I}|, |\mathrm{j} - \mathrm{I}| + 1, \ldots, \mathrm{j} + \mathrm{I} \quad , \tag{1.1.2.b}$$

where I is the nuclear total angular momentum quantum number.

Now, the gross energy levels of (the valence electron of) an alkali atom, such as a Cesium-133 atom, are labeled as $\mathrm{n}^{2s+1}\ell$, the fine structure energy levels are labeled as $\mathrm{n}^{2s+1}\ell_{\mathrm{j}}$, and the hyperfine structure energy levels are labeled as f. Here n is the electron principal quantum number.

Now:

1. For the ground state of a Cesium-133 atom one has $\ell = 0$, $\mathrm{s} = 1/2$, then according to eq. (1.1.1.b) $\mathrm{j} = 1/2$; and since $\mathrm{n} = 6$ for the ground state and $\ell = 0$ is labeled with a letter S, then the ground state gross energy level is $6^2\mathrm{S}$ with the fine structure energy level being $6^2\mathrm{S}_{1/2}$. Additionally, since for Cesium-133 one has $\mathrm{I} = 7/2$, then according to eq. (1.1.2.b) $6^2\mathrm{S}_{1/2}$ is split into two hyperfine structure energy levels $\mathrm{f} = 3$ and $\mathrm{f} = 4$.

2. For the first excited state of a Cesium-133 atom one has $\ell = 1$, $\mathrm{s} = 1/2$, then according to eq. (1.1.1.b) $\mathrm{j} = 1/2$ and $\mathrm{j} = 3/2$; and since $\mathrm{n} = 6$ for the first excited state and $\ell = 1$ is labeled with a letter P, then the first excited state gross energy level is $6^2\mathrm{P}$, which is split into two fine structure energy levels $6^2\mathrm{P}_{1/2}$ and $6^2\mathrm{P}_{3/2}$. Additionally, since $\mathrm{I} = 7/2$, then according to eq. (1.1.2.b) $6^2\mathrm{P}_{1/2}$ is split into two hyperfine structure energy levels $\mathrm{f}' = 3$ and $\mathrm{f}' = 4$, and $6^2\mathrm{P}_{3/2}$ is split into four hyperfine structure energy levels $\mathrm{f}' = 2$, $\mathrm{f}' = 3$, $\mathrm{f}' = 4$ and $\mathrm{f}' = 5$.

Note that throughout this thesis, the hyperfine structure energy levels of the ground state are marked without a prime, and the hyperfine structure energy levels of the first excited state are marked with a single prime.

The magnetic interaction between an externally applied static magnetic field and the magnetic dipole moment associated with $\hat{\mathbf{f}}$ results in an energy splitting of the hyperfine structure energy levels into the Zeeman energy levels. The Zeeman energy levels are labeled by the atomic total angular momentum projection quantum numbers $\mathrm{m_f}$, where $\mathrm{m_f} = -\mathrm{f}, -\mathrm{f} + 1, \ldots, \mathrm{f}$. Note that for the first excited state we have $\mathrm{f} \to \mathrm{f}'$ in $\mathrm{m_f}$. For e.g. the Zeeman energy levels $\mathrm{m_f}$ of the energy levels $6^2\mathrm{S}_{1/2}, \mathrm{f} = 3$ and $6^2\mathrm{S}_{1/2}, \mathrm{f} = 4$ of a Cesium-133 atom the amount of the splitting in energy for a given external static magnetic field strength can be seen in figure A1, which is a result of a more detailed treatment of the effect of an externally applied static magnetic field on a Cesium-133 atom seen in appendix A.

The gross energy levels 6^2S and 6^2P of a Cesium-133 atom are three-fold degenerate, and all the degeneracies are lifted by the combined effect of the fine structure splitting, the hyperfine structure splitting and the Zeeman splitting.

The summary of the different energy level structures that were considered in this section can be seen in figure 1.

The $6^2S_{1/2} \rightarrow 6^2P_{1/2}$ and $6^2S_{1/2} \rightarrow 6^2P_{3/2}$ transitions are called *the D line transitions* (*of Cesium-133 atom*) with $6^2S_{1/2} \rightarrow 6^2P_{1/2}$ called the D_1 line transition and $6^2S_{1/2} \rightarrow 6^2P_{3/2}$ called the D_2 line transition. The D_1 line transition can be induced by light of frequency of approximately 895 nm, and D_2 line transition − of approximately 852 nm [43].

Note that all experiments described in this thesis deal with near room temperature Cesium-133 atoms that are contained inside our specially designed microcells, which are described in section 3.2. Also, the role of the D line transitions is understood in section 3.1, where it is explained how the laser system used in the performed experiments works.

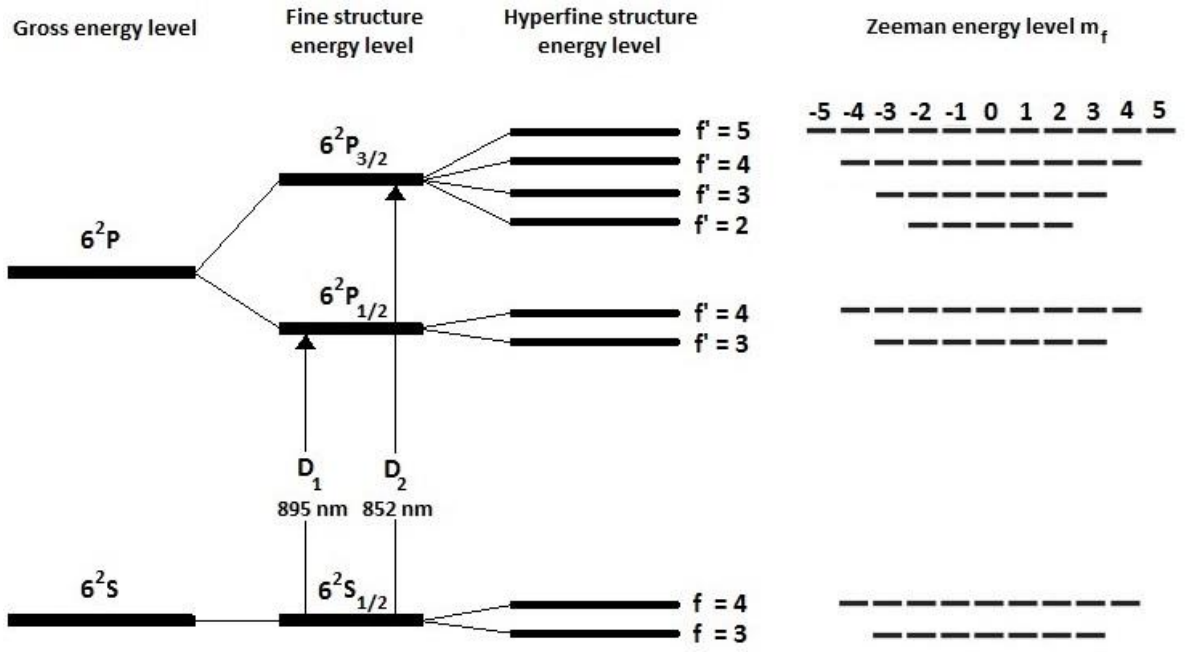

Figure 1. The gross, fine structure, hyperfine structure and the Zeeman energy structures for the ground and the first excited state of the valence electron of a Cesium-133 atom. When the fine structure splitting effect is present, the frequencies of light that can induce the $6^2S_{1/2} \rightarrow 6^2P_{1/2}$ transition, called the D_1 line transition, and the $6^2S_{1/2} \rightarrow 6^2P_{3/2}$ transition, called the D_2 line transition, are approximately 895 nm and 852 nm, respectively [43]. Note that the different splittings of the levels are not to scale.

1.2 The coherent spin states of Cesium-133 atom

Consider an ensemble of $N_a \in \mathbb{N}$ atoms of same element.

The atomic ensemble total angular momentum vector operator $\hat{\mathbf{J}}$ [1] is defined as a sum of the atomic total angular momentum vector operators $\hat{\mathbf{f}}_n$, where n denotes the n'th atom in the ensemble, i.e.

$$\hat{\mathbf{J}} \equiv \sum_{n=1}^{N_a} \hat{\mathbf{f}}_n \quad , \tag{1.2.1}$$

where in three spatial dimensions one has

$$\hat{\mathbf{J}} = \left(\hat{J}_x, \hat{J}_y, \hat{J}_z\right) \quad , \tag{1.2.2.a}$$
$$\hat{\mathbf{f}} = \left(\hat{f}_x, \hat{f}_y, \hat{f}_z\right) \quad , \tag{1.2.2.b}$$

where $\hat{J}_x, \hat{J}_y, \hat{J}_z$ are atomic ensemble total angular momentum operators along the mutually orthogonal x-, y- and z-axes, respectively, and $\hat{f}_x, \hat{f}_y, \hat{f}_z$ are atomic total angular momentum operators along x-, y- and z-axes, respectively; they satisfy the commutation relations

$$\left[\hat{J}_q, \hat{J}_w\right] = i\hbar \sum_{r=1}^{3} \epsilon_{qwr} \hat{J}_r \quad , \tag{1.2.3.a}$$
$$\left[\hat{f}_q, \hat{f}_w\right] = i\hbar \sum_{r=1}^{3} \epsilon_{qwr} \hat{f}_r \quad , \tag{1.2.3.b}$$

where q, w, r = 1, 2, 3 (1 for x, 2 for y, 3 for z), and ϵ_{qwr} is the three-dimensional permutation symbol.

According to the principles of quantum mechanics, if one chooses the quantization-axis of the vector operator $\hat{\mathbf{f}}$ to be the z-axis, then the operator $\hat{f}_z$ must satisfy

$$\hat{f}_z |f, m_f> = \hbar m_f |f, m_f> \quad , \tag{1.2.4}$$

where $|f, m_f>$ is an eigenstate of $\hat{f}_z$, and $m_f = -f, -f+1, \ldots, f$, and the remaining operators $\hat{f}_x$ and $\hat{f}_y$ must according to the generalized Heisenberg uncertainty principle

$$\mathrm{Var}(\hat{C})\mathrm{Var}(\hat{Z}) \geq \left(\frac{1}{2i}\langle[\hat{C}, \hat{Z}]\rangle\right)^2 \tag{1.2.5}$$

for two operators $\hat{C}$ and $\hat{Z}$, satisfy

$$\mathrm{Var}(\hat{f}_x)\mathrm{Var}(\hat{f}_y) \geq \left(\frac{1}{2i}\langle[\hat{f}_x, \hat{f}_y]\rangle\right)^2 = \left(\frac{1}{2i}\langle i\hbar \hat{f}_z\rangle\right)^2 = \left(\frac{i\hbar}{2i}\langle \hat{f}_z\rangle\right)^2 = \left(\frac{i\hbar}{2i}\langle f, m_f|\hat{f}_z|f, m_f\rangle\right)^2$$
$$= \left(\frac{i\hbar}{2i}\hbar m_f\right)^2 = \frac{\hbar^4}{4} {m_f}^2 \quad , \tag{1.2.6}$$

which is obtained by observing eqs. (1.2.3.b) and (1.2.4).

Note that in this thesis we will call the state $|f, m_f>$ a *spin state*.

Now, with z-axis being the quantization-axis, define the ladder operator $\hat{f}_+$ and its hermitian conjugate $\hat{f}_-$ as

[1] The reason, why $\hat{\mathbf{J}}$ is used to stand for the atomic ensemble total angular momentum vector operator instead of the more obvious $\hat{\mathbf{F}}$, is conventional.

$$\hat{f}_{\pm} \equiv \hat{f}_x \pm i\hat{f}_y \quad ; \tag{1.2.7}$$

they satisfy

$$\hat{f}_{\pm}|f, m_f> = \hbar\sqrt{f(f+1) - m_f(m_f \pm 1)}\ |f, m_f \pm 1> \quad , \tag{1.2.8}$$

Using now eq. (1.2.8) one sees that for the spin states $|f, m_f = \pm f> = |f, \pm f>$ one obtains

$$\hat{f}_{\pm}\ |f, \pm f> = 0 \quad ; \tag{1.2.9}$$

and thus it follows that for the expectation values $\langle f, \pm f|\hat{f}_i|f, \pm f\rangle$ and $\langle f, \pm f|(\hat{f}_i)^2|f, \pm f\rangle$, where i = x, y, that

$$\langle f, \pm f|\hat{f}_x|f, \pm f\rangle = \left\langle f, \pm f\left|\frac{1}{2}(\hat{f}_+ + \hat{f}_-)\right|f, \pm f\right\rangle = 0 \quad , \tag{1.2.10.a}$$

$$\langle f, \pm f|\hat{f}_y|f, \pm f\rangle = \left\langle f, \pm f\left|\frac{1}{2i}(\hat{f}_+ - \hat{f}_-)\right|f, \pm f\right\rangle = 0 \quad , \tag{1.2.10.b}$$

$$\langle f, \pm f|(\hat{f}_x)^2|f, \pm f\rangle = \left\langle f, \pm f\left|\left(\frac{1}{2}(\hat{f}_+ + \hat{f}_-)\right)^2\right|f, \pm f\right\rangle = \frac{\hbar^2}{2}f \quad , \tag{1.2.10.c}$$

$$\langle f, \pm f|(\hat{f}_y)^2|f, \pm f\rangle = \left\langle f, \pm f\left|\left(\frac{1}{2i}(\hat{f}_+ - \hat{f}_-)\right)^2\right|f, \pm f\right\rangle = \frac{\hbar^2}{2}f \quad ; \tag{1.2.10.d}$$

and since the variance $\mathrm{Var}(\hat{A}) \equiv E\left((\hat{A})^2\right) - \left(E(\hat{A})\right)^2$, where $E(.)$ refers to the expectation value, then for $|f, \pm f>$ the following holds:

$$\mathrm{Var}(\hat{f}_x) = \mathrm{Var}(\hat{f}_y) \quad . \tag{1.2.11}$$

The spin states $|f, m_f>$ for which the equality in eq. (1.2.11) holds, are called *the coherent spin states of Cesium-133 atom*; and since by observing eqs. (1.2.10.a-d) one has that for the spin states $|4, \pm 4>$ the equality in eq. (1.2.11) holds, then, by definition, $|4, \pm 4>$ are the coherent spin states of Cesium-133 atom.

For $C_a \in \mathbb{N}$ Cesium-133 atoms in the coherent spin state $|4, 4>$ one obtains from eqs. (1.2.1), (1.2.3.a), (1.2.5) and (1.2.11) the equality

$$\mathrm{Var}(\hat{J}_x)\mathrm{Var}(\hat{J}_y) = \left(\frac{1}{2i}\langle[\hat{J}_x, \hat{J}_y]\rangle\right)^2 = \left(\frac{i\hbar}{2i}\langle\hat{J}_z\rangle\right)^2 = \left(\frac{i\hbar}{2i}\langle\sum_n^{C_a}\hat{f}_{z,n}\rangle\right)^2 = \left(\frac{i\hbar}{2i}\langle 4,4|\sum_n^{C_a}\hat{f}_{z,n}|4,4\rangle\right)^2 = \left(\frac{i\hbar}{2i}C_a\hbar 4\right)^2 =$$
$$= \frac{\hbar^4}{4}{C_a}^2 4^2 = \frac{\hbar^4}{4}J_{z,C_a}^2 \quad , \tag{1.2.12}$$

where $J_{z,C_a} \equiv 4C_a$.

Now, eqs. (1.2.4) and (1.2.6) are mathematical formulations of the statement that tells us that if one chooses the quantization-axis of the vector operator $\hat{\mathbf{f}}$ to be the z-axis, then measurements of the operators $\hat{f}_x$, $\hat{f}_y$ and $\hat{f}_z$ will yield projections of $\hat{\mathbf{f}}$ along x-, y- and z-axes given by the values M_x, M_y

and M_z, respectively, where $M_z \equiv \hbar m_f$ with $m_f \in \{-f, -f+1, \ldots, f\}$, and M_x and M_y may both be equal to any real number as long as the product of variances of measurements of $\hat{f}_x$ and $\hat{f}_y$ is larger or equal to $\frac{\hbar^4}{4} {m_f}^2$; and thus one may argue that in cases, where a great amount of Cesium-133 atoms reside in the coherent spin state $|4,4>$, where $m_f = 4$, the operator $\hat{J}_z$ can be treated as a macroscopic quantity such that $\hat{J}_z \to \langle 4,4|\hat{J}_z|4,4\rangle = C_a \hbar 4 = \hbar J_z$, where $J_z \equiv J_{z,C_a}$ where C_a is *large*. This is a valid argument, because for C_a Cesium-133 atoms in the coherent spin state $|4,4>$ we have from eq. (1.2.12) that the ratio between the standard deviations of measurements of $\hat{J}_x$ and $\hat{J}_z$, and also $\hat{J}_y$ and $\hat{J}_z$ is $\frac{\sqrt{\mathrm{Var}(\hat{J}_x)}}{\hbar J_{z,C_a}} = \frac{\sqrt{\mathrm{Var}(\hat{J}_y)}}{\hbar J_{z,C_a}} = \frac{\sqrt{\frac{\hbar^2 J_{z,C_a}}{2}}}{\hbar J_{z,C_a}} = \frac{\sqrt{\frac{\hbar^2 J_{z,C_a}}{2}}}{\hbar J_{z,C_a}} = \frac{\sqrt{\frac{\hbar^2 (4C_a)}{2}}}{\hbar (4C_a)} = \frac{1}{\sqrt{8C_a}}$.

Note that in section 3.2.2 we observe that the performed experiment on atomic density of Cesium-133 vapor inside the microchannel of one of our specially designed microcells suggests that we are dealing with a great amount of Cesium-133 atoms, because for that particular experiment we obtain a number of atoms that is on the order of 10^7. In this case the ratio between the standard deviations of measurements of $\hat{J}_x$ and $\hat{J}_z$ (and also $\hat{J}_y$ and $\hat{J}_z$) becomes $\frac{1}{\sqrt{8C_a}} \approx 10^{-4}$, which is small enough for us to rightfully assume that here $\hat{J}_z$ can be treated as a macroscopic quantity.

Note that when the equality $\mathrm{Var}(\hat{J}_x)\mathrm{Var}(\hat{J}_y) = \frac{\hbar^4}{4} J_z^2$ holds, it is said the noise of the operators $\hat{J}_x$ and $\hat{J}_y$ is at the so-called *projection-noise* level.

1.3 Characterizing the polarization of light

Consider an ensemble of photons of the same frequency propagating along the x-axis.

By decomposing the electric field operator associated with the ensemble of photons into two components along the y- and z-axes we have that such electric field operator can be written as

$$\hat{\mathbf{E}}_{\mathrm{ensemble}}(x) = \sqrt{\frac{\hbar\omega}{2\varepsilon_0 A_{cs} L_q}} \left(\left(\hat{a}_y \mathbf{e}_y + \hat{a}_z \mathbf{e}_z \right) e^{ikx} + \left(\hat{a}_y^\dagger \mathbf{e}_y^* + \hat{a}_z^\dagger \mathbf{e}_z^* \right) e^{-ikx} \right) \quad , \tag{1.3.1}$$

where ε_0 is the vacuum permittivity, A_{cs} is the transverse cross-sectional area of the photonic beam, L_q is the quantization length along the x-axis, k is the angular wave number along the x-axis, which is related to the electric field angular frequency ω as $k \equiv \omega/c$, $\mathbf{e}_y$ and $\mathbf{e}_z$ are the (complex) Cartesian basis vectors along y- and z-axes, respectively, which describe the direction of polarization, which is perpendicular to k, $\hat{a}_j(t)$ and $\hat{a}_j^\dagger(t)$, where j = y, z, are the photonic annihilation and creation operators for j-polarized photons in the ensemble, respectively, that satisfy the commutation relation

$$\left[\hat{a}_j, \hat{a}_{j'}^\dagger \right] = \delta_{j,j'} \quad . \tag{1.3.2}$$

The Stokes four-vector operator characterizing the ensemble of photons is defined as

$$\hat{\mathbf{S}}_{st} \equiv \left(\hat{S}_0, \hat{\mathbf{S}}\right) = \left(\hat{S}_0, \hat{S}_x, \hat{S}_y, \hat{S}_z\right) \quad , \tag{1.3.3}$$

where

$$\hat{\mathbf{S}} \equiv (\hat{S}_x, \hat{S}_y, \hat{S}_z) \quad , \tag{1.3.4}$$

is the Stokes three-vector operator, and

$$\hat{S}_0 \equiv \frac{1}{2}\left(\hat{n}_y + \hat{n}_z\right) = \frac{1}{2}(\hat{a}_y^\dagger \hat{a}_y + \hat{a}_z^\dagger \hat{a}_z) \quad , \tag{1.3.5.a}$$

$$\hat{S}_x \equiv \frac{1}{2}\left(\hat{n}_y - \hat{n}_z\right) = \frac{1}{2}(\hat{a}_y^\dagger \hat{a}_y - \hat{a}_z^\dagger \hat{a}_z) \quad , \tag{1.3.5.b}$$

$$\hat{S}_y \equiv \frac{1}{2}(\hat{n}_{+45^\circ} - \hat{n}_{-45^\circ}) = \frac{1}{2}(\hat{a}_y^\dagger \hat{a}_z + \hat{a}_z^\dagger \hat{a}_y) \quad , \tag{1.3.5.c}$$

$$\hat{S}_z \equiv \frac{1}{2}\left(\hat{n}_{\sigma_+} - \hat{n}_{\sigma_-}\right) = \frac{1}{i2}(\hat{a}_y^\dagger \hat{a}_z - \hat{a}_z^\dagger \hat{a}_y) \quad , \tag{1.3.5.d}$$

are the Stokes operators, where in the last equality of eqs. (1.3.5.c) and (1.3.5.d) the relations

$$\hat{a}_{+45^\circ} \equiv \frac{\hat{a}_y + \hat{a}_z}{\sqrt{2}}, \quad \hat{a}_{-45^\circ} \equiv \frac{\hat{a}_y - \hat{a}_z}{\sqrt{2}} \quad , \tag{1.3.6.a}$$

$$\hat{a}_{\sigma_+} \equiv \frac{\hat{a}_y - i\hat{a}_z}{\sqrt{2}}, \quad \hat{a}_{\sigma_-} \equiv \frac{\hat{a}_y + i\hat{a}_z}{\sqrt{2}} \quad , \tag{1.3.6.b}$$

were used, where $\hat{n}_p \equiv \hat{a}_p^\dagger \hat{a}_p$ with p = y, z, $+45^\circ$, $-45°$, σ_+, σ_- is a photon number operator for y-, z-, $+45^\circ$-, $-45°$-, right-circularly-, left-circularly-polarized photons in the ensemble, with $\hat{a}_p^\dagger$, $\hat{a}_p$ being the corresponding creation and annihilation operators, respectively.

$\hat{S}_0$, $\hat{S}_x$, $\hat{S}_y$, $\hat{S}_z$ in eqs. (1.3.5.a-d) satisfy the commutation relations

$$\left[\hat{S}_q, \hat{S}_w\right] = i\sum_{r=1}^{3} \epsilon_{qwr} \hat{S}_r \quad , \tag{1.3.7.a}$$

$$\left[\hat{S}_0, \hat{S}_w\right] = 0 \quad , \tag{1.3.7.b}$$

where q, w, r = 1, 2, 3 (1 for x, 2 for y, 3 for z), and ϵ_{qwr} is the three-dimensional permutation symbol.

From eqs. (1.3.5.a-d) we see that the expectation value of the Stokes operator $\hat{S}_0$ gives us half the number of the photons in the photonic ensemble, i.e. $\langle \hat{S}_0 \rangle = \frac{1}{2}\langle \hat{n}_y + \hat{n}_z \rangle = \frac{C_{ph,tot}}{2}$, where $C_{ph,tot} \in \mathbb{N}$ is the number of photons in the photonic ensemble, and the Stokes operators $\hat{S}_x$, $\hat{S}_y$, $\hat{S}_z$ can be used to count the differences in photon numbers for polarized photons of the different orthogonal bases; $\hat{S}_x$, $\hat{S}_y$, $\hat{S}_z$ can thus be said to *characterize the polarization of light*.

Assuming now that almost all of the photons in the photonic ensemble are linearly-polarized along the z-direction we have that the Stokes operator

$$\hat{S}_x \to S_x, \tag{1.3.8}$$

where $S_x \equiv \langle \hat{S}_x \rangle = \langle \frac{1}{2}(\hat{n}_y - \hat{n}_z) \rangle \approx -\frac{1}{2}\langle \hat{n}_z \rangle$ is a real number.

Note that the light emitted by the probe laser that we use in the experiments is assumed to be linearly-polarized. Assuming that the light emitted by the probe laser is travelling along the x-axis and that it is the z-direction along which the probe laser photons are linearly-polarized, it must therefore be true that for the probe laser light the assumption of eq. (1.3.8) holds. The probe laser is described in section 3.1.1.

Now, from the generalized Heisenberg uncertainty principle seen in eq. (1.2.5) and eqs. (1.3.7.a), (1.3.8) we see that

$$\mathrm{Var}(\hat{S}_y)\mathrm{Var}(\hat{S}_z) \geq \left(\frac{1}{2i}\langle [\hat{S}_y, \hat{S}_z] \rangle\right)^2 = \left(\frac{i}{2i}\langle \hat{S}_x \rangle\right)^2 = \left(\frac{i}{2i} S_x\right)^2 = \frac{1}{4} {S_x}^2 \quad . \tag{1.3.9}$$

Similarly to section 1.2, we can now arrive at the definition for *the coherent states of light*: the states for which the equality

$$\mathrm{Var}(\hat{S}_y) = \mathrm{Var}(\hat{S}_z) \tag{1.3.10}$$

holds are the coherent states of light. According to eqs. (1.3.9) and (1.3.10) the equality

$$\mathrm{Var}(\hat{S}_y)\mathrm{Var}(\hat{S}_z) = \frac{1}{4} {S_x}^2 \tag{1.3.11}$$

holds for the coherent states of light; and in such a case it is said the noise of the operators $\hat{S}_y$ and $\hat{S}_z$ is at the so-called *shot-noise* level.

1.4 The atom-light system Hamiltonian

The Hamiltonian for an atom-light system can in general be written as

$$\hat{H}_{AL} = \hat{H}_{Atomic} + \hat{H}_{Light} + \hat{H}_I \quad , \tag{1.4.1}$$

where $\hat{H}_{Atomic}$ is the atom Hamiltonian, $\hat{H}_{Light}$ is the light Hamiltonian, and $\hat{H}_I$ is the atom-light interaction Hamiltonian.

In this section the atom-light system to be considered will be the one treated in the atom-membrane entanglement protocol described in chapter 2. The atom-membrane entanglement experiment, which is described in chapter 4, and is an attempt at a real life realization of the entanglement protocol described in chapter 2, will serve as the basis for the following derivations.

In the first three subsections of this section, the three Hamiltonians $\hat{H}_{Atomic}$, $\hat{H}_{Light}$ and $\hat{H}_I$ will be treated separately; this will be done in the Heisenberg picture, where the quantum operators are time-dependent and quantum states are time-independent. Having found the effective atom-light interaction Hamiltonian $\hat{H}_I^{eff}$ dealing with off-resonant D_2 line transition $6^2S_{1/2}, f = 4 \rightarrow 6^2P_{3/2}, f` = 5$, the propagation equations for the operators $\hat{J}_i$ and $\hat{S}_i$, where i = x, y, z, introduced in

sections 1.2 and 1.3, respectively, will be presented in the fourth subsection of this section. In the fifth subsection of this section the scaled versions of the operators $\hat{J}_i$ and $\hat{S}_i$ will be presented and the aforementioned propagation equations will be transformed and written in terms of these scaled operators; these transformed propagation equations will in chapter 2 aid us in understanding how the atom-membrane entanglement protocol works.

Note that throughout this thesis, that whenever talking about *ensembles* of Cesium-133 atoms, the ground hyperfine structure energy levels will be labeled by the unprimed capital letter F, and the excited hyperfine structure energy levels will be label by the primed capital letter F`.

Before presenting $\hat{H}_{\text{Atomic}}$, $\hat{H}_{\text{Light}}$ and $\hat{H}_I$ it is important to know that during the atom-membrane entanglement experiment the Cesium-133 atoms can be shined on by three lasers: a probe laser, a pump laser and a repump laser; see figure 4 to see the relevant energy levels of Cesium-133 atoms addressed by these lasers. As described in section 3.1, the role of the probe laser is to probe the Cesium-133 atoms by coupling them off-resonantly to the D_2 line transition $6^2S_{1/2}, F = 4 \rightarrow 6^2P_{3/2}, F` = 5$, and the role of the pump and repump lasers is to put as many of the Cesium-133 atoms into the coherent state $|F = 4, m_F = 4>$ of the energy level $6^2S_{1/2}, F = 4, m_F = 4$, as possible, whereby the Cesium-133 atomic ensemble total angular momentum operator along the quantization-axis can be treated as a macroscopic quantity. In the derivations below I will be neglecting the effect of the pump and repump lasers, thus only considering the effect of the probe laser; and because the Cesium-133 atoms are coupled off-resonantly to the D_2 line transition $6^2S_{1/2}, F = 4 \rightarrow 6^2P_{3/2}, F` = 5$, by the probe laser, I shall assume that the Cesium-133 atoms lie in any Zeeman energy level $m_F$ of the energy level $6^2S_{1/2}, F = 4$ and any Zeeman energy level $m_{F`}$ of the energy levels $6^2P_{3/2}, F` = 2, 3, 4, 5$. Also, since as understood from section 3.2.1, during the atom-membrane entanglement experiment we only care about the Cesium-133 atoms that are contained inside the microchannel of our specially designed microcells. This microchannel has an almost fixed transverse cross-sectional area and length, and the probe laser travelling through the microchannel interacts with all the atoms during the measurement time; and thus I shall assume that the transverse cross-sectional area and the length of Cesium-133 atom medium are constant and are respectively the same as the transverse cross-sectional area of the probe laser light beam and the quantization length along the propagation direction of the probe laser light. Also, since in the atom-membrane entanglement experiment described in chapter 4 we have that the probe laser light is travelling along the x-axis, and that the quantization-axis of $\hat{\mathbf{J}}$ is the z-axis, it will be assumed that these things also hold in the following derivations.

1.4.1 The atom Hamiltonian

From the considerations made in the introductory text of section 1.4, we have that we can write the atom Hamiltonian $\hat{H}_{\text{Atomic}}$ as

$$\hat{H}_{\text{Atomic}} = \sum_{f`=2}^{5} \sum_{m_{f`}} \int_0^L dx\, \hbar(\omega_0 + \Delta_{f`}) \hat{\sigma}_{f`,m_{f`};f`,m_{f`}}(x,t) \rho A \quad , \qquad (1.4.1.1)$$

where the sums are performed over the atomic total angular momentum quantum numbers $f` = 2, 3, 4, 5$ and the atomic total angular momentum projection quantum numbers $m_{f`} = -f`, -f` + 1, \ldots, f`$ for each $f`$, and the integral is performed over x from 0 to L. Here L is the (constant) length of the Cesium-133 atom medium, ρ is the density of the Cesium-133 atom medium, A is the (constant) transverse cross-sectional area of the Cesium-133 atom medium, ω_0 is the carrier angular frequency of the probe laser light, $\Delta_{f`}$ is the negative angular frequency detuning between $\omega_0$ and the angular frequency of the $D_2$ line transition $6^2S_{1/2}, f = 4 \rightarrow 6^2P_{3/2}, f`$, and $\hat{\sigma}_{f`,m_{f`};f`,m_{f`}}(x,t) = |f`, m_{f`}><f`, m_{f`}|(x,t)$ is the density operator, which measures the probability for a Cesium-133 atom in the ensemble at position x and time t of being in the excited spin state $|f`, m_{f`}>$. Note that the energy of the level $6^2P_{3/2}, f`$ is $\hbar(\omega_0 + \Delta_{f`})$, and also note that the energy of the level $6^2S_{1/2}, f = 4$ is taken to be zero, and so, because of that, the term in $\hat{H}_{\text{Atomic}}$ that involves the spin state $|f = 4, m_f>$, where $m_f = -4, -4 + 1, \ldots, 4$, is cancelled.

1.4.2 The light Hamiltonian

Since in the introductory text of section 1.4 it is written that the transverse cross-sectional area and the length of Cesium-133 atom medium are constant and are respectively the same as the transverse cross-sectional area of the probe laser light beam and the quantization length along the propagation direction of the probe laser light, and also that the probe laser light travels in the x-direction, we have that the electric field operator associated with the probe laser light can be written as

$$\hat{\mathbf{E}}(x,t) = \sum_{\lambda} \hat{\mathbf{E}}_{\text{ensemble},\lambda}(x,t) =$$

$$= \sum_{\lambda} \sqrt{\frac{\hbar\omega_\lambda}{2\varepsilon_0 AL}} \left(\left(\hat{a}_{y,\lambda}(t)\mathbf{e}_y + \hat{a}_{z,\lambda}(t)\mathbf{e}_z \right) e^{ik_\lambda x} + \left(\hat{a}^\dagger_{y,\lambda}(t)\mathbf{e}^*_y + \hat{a}^\dagger_{z,\lambda}(t)\mathbf{e}^*_z \right) e^{-ik_\lambda x} \right) \quad , \qquad (1.4.2.1)$$

where

$$\hat{\mathbf{E}}_{\text{ensemble},\lambda}(x,t) = \sqrt{\frac{\hbar\omega_\lambda}{2\varepsilon_0 AL}} \left(\left(\hat{a}_{y,\lambda}(t)\mathbf{e}_y + \hat{a}_{z,\lambda}(t)\mathbf{e}_z \right) e^{ik_\lambda x} + \left(\hat{a}^\dagger_{y,\lambda}(t)\mathbf{e}^*_y + \hat{a}^\dagger_{z,\lambda}(t)\mathbf{e}^*_z \right) e^{-ik_\lambda x} \right) \qquad (1.4.2.2)$$

is the electric field operator associated with the probe laser light photons with the angular frequency ω_λ, k_λ is the angular wave number along the x-axis, which is related to ω_λ as $k_\lambda \equiv \omega_\lambda / c$, $\mathbf{e}_y$ and $\mathbf{e}_z$ are the (complex) Cartesian basis vectors along y- and z-axes, respectively, which describe the direction of polarization, which is perpendicular to k_λ for all λ, $\hat{a}_{j,\lambda}(t)$ and $\hat{a}^\dagger_{j,\lambda}(t)$, where $j = y, z$, are the photonic annihilation and creation operators for j-polarized probe laser light photons with the angular frequency ω_λ, respectively, that are dimensionless and that satisfy the commutation relation

$$\left[\hat{a}_{j,\lambda}(t), \hat{a}^\dagger_{j',\lambda'}(t) \right] = \delta_{j,j'}\delta_{\lambda,\lambda'}. \qquad (1.4.2.3)$$

Note that in eq. (1.4.2.1) $\hat{\mathbf{E}}(x,t)$ is decomposed into two components along the y- and z-axes, similarly to the case of eq. (1.3.1).

Now, the electric field $\hat{\mathbf{E}}$ in eq. (1.4.2.1) assumes a discrete resolution in k-space. We would now like $\hat{\mathrm{E}}$ in eq. (1.4.2.1) to assume a continuous resolution in k-space, i.e. we would like to make the change $\sum \Delta k \rightarrow \int dk$. To do so, let us define the operator

$$\hat{a}_j(k,t) \equiv \frac{\hat{a}_{j,\lambda}(t)}{\sqrt{\Delta k}} \quad , \tag{1.4.2.4}$$

such that $\hat{\mathbf{E}}(x,t)$ in eq. (1.4.2.1) becomes

$$\hat{\mathbf{E}}(x,t) = \int dk \sqrt{\frac{\hbar\omega}{4\pi\varepsilon_0 A}} \left(\left(\hat{a}_y(k,t)\mathbf{e}_y + \hat{a}_z(k,t)\mathbf{e}_z \right) e^{ikx} + \left(\hat{a}_y^\dagger(k,t)\mathbf{e}_y^* + \hat{a}_z^\dagger(k,t)\mathbf{e}_z^* \right) e^{-ikx} \right) \ , \tag{1.4.2.5}$$

where $k \equiv \omega/c$, and $\hat{a}_j(k,t)$ and $\hat{a}_j^\dagger(k,t)$, where $j = y, z$, are the annihilation and creation operators for j-polarized probe laser light photons with the angular frequency ω, respectively, that have units of inverse of square root of length (in k-space) and that satisfy the commutation relation

$$\left[\hat{a}_j(k,t), \hat{a}_{j'}^\dagger(k',t) \right] = \delta_{j,j'}\delta(k-k') \quad . \tag{1.4.2.6}$$

Observe that the LHS and RHS of eq. (1.4.2.6) have the same dimension; this is true, because $\delta(k-k')$ has units of inverse of length (in k-space) as seen from the identity $\int_{-\infty}^{+\infty} dk\, \delta(k) = 1$. With $\hat{\mathbf{E}}$ in eq. (1.4.2.5) the light Hamiltonian $\hat{H}_{\mathrm{Light}}$ we need to consider becomes

$$\hat{H}_{\mathrm{Light}} = \int dk\, \hbar ck \left(\hat{a}^\dagger(k,t)\hat{a}(k,t) + \frac{1}{2} \right) \ , \tag{1.4.2.7}$$

where the operators $\hat{a}(k,t)$ and $\hat{a}^\dagger(k,t)$ respectively take into account the operators $\hat{a}_j(k,t)$ and $\hat{a}_j^\dagger(k,t)$, where j = y, z. Note that $\hat{n}_k(t) \equiv \hat{a}^\dagger(k,t)\hat{a}(k,t)$ is a photon number operator for the probe laser photons with wave numbers in the interval [k, k + dk] at time t.

$\hat{H}_L$ in eq. (1.4.2.7) is in k-space; in order to obtain $\hat{H}_{\mathrm{Light}}$ in x-space one performs the following Fourier transformations of $\hat{a}(k,t)$ and $\hat{a}^\dagger(k,t)$:

$$\hat{a}(x,t) = \frac{1}{\sqrt{2\pi}} \int_{-\infty}^{+\infty} dk\, \hat{a}(k,t) e^{ikx} \quad , \tag{1.4.2.8.a}$$

$$\hat{a}^\dagger(x,t) = \frac{1}{\sqrt{2\pi}} \int_{-\infty}^{+\infty} dk\, \hat{a}^\dagger(k,t) e^{-ikx} \quad ; \tag{1.4.2.8.b}$$

$\hat{a}(x,t)$ and $\hat{a}^\dagger(x,t)$ have units of inverse of square root of length (in x-space) and they satisfy the commutation relation

$$\left[\hat{a}(x,t), \hat{a}^\dagger(x',t) \right] = \delta(x-x') \quad . \tag{1.4.2.9}$$

Note that $\hat{n}_x(t) \equiv \hat{a}^\dagger(x,t)\hat{a}(x,t)$ is a photon number operator for the probe laser photons located in the spatial interval [x, x + dx] at time t.

1.4.3 The atom-light interaction Hamiltonian

The atom-light interaction Hamiltonian presented here will assume the electric dipole approximation. In a case, where $N_C \in \mathbb{N}$ Cesium-133 atoms are considered, such atom-light interaction Hamiltonian will thus describe the electric dipole interaction

$$\hat{H}_I = -\sum_{n=1}^{N_C} \hat{\mathbf{d}}_n \bullet \hat{\mathbf{E}}(x_n, t) \quad , \tag{1.4.3.1}$$

where $\hat{\mathbf{d}}_n \equiv -e\hat{\mathbf{r}}_n$ is the (electric) dipole operator, with e being the elementary charge, for the n'th Cesium-133 atom, x_n is the position of the n'th Cesium-133 atom on the x-axis, and $\hat{\mathbf{E}}(x_n, t)$ is the electric field operator in eq. (1.4.2.5) for the probe laser light defined at x_n and time t.

Note that the electric dipole approximation is justifiable for all experiments described in this thesis, because when observing sections 3.1.1 and 3.2.1, we see that the transverse cross-sectional area of the probe laser light and Cesium-133 interface, A, is much larger than the carrier wavelength of the probe laser light, λ_0, squared, i.e. $A \gg \lambda_0^2$.

Let us for now consider working in the circular basis.

In the circular basis the vector operator $\hat{\mathbf{r}}$ for a single atom is

$$\hat{\mathbf{r}} = \hat{\mathbf{e}}^*{}_{\sigma_+}\hat{r}_+ + \hat{\mathbf{e}}^*{}_0\hat{r}_0 + \hat{\mathbf{e}}^*{}_{\sigma_-}\hat{r}_- \quad , \tag{1.4.3.2}$$

where the circular basis unit vectors are $\mathbf{e}_{\sigma_\pm} \equiv \frac{\mathbf{e}_y \pm i\mathbf{e}_z}{\sqrt{2}}$, $\mathbf{e}_0 \equiv \mathbf{e}_x$, and the circular basis vector components of $\hat{\mathbf{r}}$ are $\hat{r}_\pm \equiv \frac{\hat{y} \pm i\hat{z}}{\sqrt{2}}$, $\hat{r}_0 \equiv \hat{x}$,. Using eq. (1.4.3.2) we thus have that in the circular basis the dipole operator $\hat{\mathbf{d}} \equiv -e\hat{\mathbf{r}}$ for a single atom becomes

$$\hat{\mathbf{d}} = \sum_{f,m_f;f`,m_{f`}} \left(d^-_{f,m_f;f`,m_{f`}} \mathbf{e}^*_{\sigma_+} + d^0_{f,m_f;f`,m_{f`}} \mathbf{e}^*_0 + d^+_{f,m_f;f`,m_{f`}} \mathbf{e}^*_{\sigma_-} \right) \hat{\sigma}_{f,m_f;f`,m_{f`}} + h.c. \quad , \tag{1.4.3.3}$$

where the sums are performed over the atomic total angular momentum quantum numbers f and f`, and the atomic total angular momentum projection quantum numbers $m_f = -f, -f+1, \ldots, f$ for each f, and $m_{f`} = -f`, -f`+1, \ldots, f`$ for each f`. Here $d^+_{f,m_f;f`,m_{f`}} \equiv -e\langle f, m_f|\hat{r}_-|f`, m_{f`}\rangle$, $d^-_{f,m_f;f`,m_{f`}} \equiv -e\langle f, m_f|\hat{r}_+|f`, m_{f`}\rangle$, $d^0_{f,m_f;f`,m_{f`}} \equiv -e\langle f, m_f|\hat{r}_0|f`, m_{f`}\rangle$ are the dipole moments, and $\hat{\sigma}_{f,m_f;f`,m_{f`}} = |f, m_f><f`, m_{f`}|$ is the density operator, which expresses coherence between the excited spin state $|f`, m_{f`}>$ and the ground spin state $|f, m_f>$.

In the circular basis the electric field operator in eq. (1.4.2.5) for the probe laser light becomes

$$\hat{\mathbf{E}}(x,t) = \sqrt{\frac{\hbar\omega_0}{2\epsilon_0 A}} \left(\hat{a}_{\sigma_+}(x,t)\mathbf{e}_{\sigma_+} + \hat{a}^\dagger_{\sigma_+}(x,t)\mathbf{e}^*_{\sigma_+} + \hat{a}_{\sigma_-}(x,t)\mathbf{e}_{\sigma_-} + \hat{a}^\dagger_{\sigma_-}(x,t)\mathbf{e}^*_{\sigma_-} \right) \quad , \tag{1.4.3.4}$$

where the Fourier transformations in eqs. (1.4.2.8.a-b) are used, where it is assumed that the electric field operator in eq. (1.4.2.5) is restricted to a narrow band of frequencies around the carrier angular frequency ω_0, and eq. (1.3.6.a) is used.

Using eqs. (1.4.3.3) and (1.4.3.4) for $\hat{\mathbf{d}}$ and $\hat{\mathbf{E}}(x,t)$, respectively, and defining the coupling constants $g^{\sigma_j}_{f,m_f;f`,m_{f`}} \equiv \sqrt{\frac{\hbar\omega_0}{2\epsilon_0 A}}\, d^j_{f,m_f;f`,m_{f`}}$, where $j = \pm$, and integrating over the length L of the ensemble containing the Cesium-133 atoms, we have that $\hat{H}_I$ in eq. (1.4.3.1) becomes

$$\hat{H}_I = \sum_{f,m_f;f`,m_{f`}} \int_0^L dx\, \rho A \left(\left[g^{\sigma_+}_{f,m_f;f`,m_{f`}} \hat{a}_{\sigma_+}(x,t) + g^{\sigma_-}_{f,m_f;f`,m_{f`}} \hat{a}_{\sigma_-}(x,t) \right] \hat{\sigma}_{f`,m_{f`};f,m_f}(x,t) + \text{h. c.} \right) \quad , \quad (1.4.3.5)$$

when the rotating wave approximation is used, that is, when the fast oscillating terms are set to zero. In $\hat{H}_I$ in eq. (1.4.3.5) we see that the first and the second terms include the annihilation operators $\hat{a}_{\sigma_+}(x,t)$ and $\hat{a}_{\sigma_-}(x,t)$ for respectively right- and left- circularly polarized photons at position x and time t, accompanied by the density operators $\hat{\sigma}_{f`,m_{f`};f,m_f}(x,t) = |f`, m_{f`}><f, m_f|(x,t)$, such that a Cesium-133 atom in the ensemble at position x and time t is taken from the ground spin state $|f, m_f>$ to the excited spin state $|f`, m_{f`}>$ and a photon is absorbed, while the (real) coupling constants $g^{\sigma_+}_{f,m_f;f`,m_{f`}}$ and $g^{\sigma_-}_{f,m_f;f`,m_{f`}}$ govern the strength of the atomic transitions. Note that due to the selection rules given by eqs. (3.1.2.2.b-c) we have that $g^{\sigma_+}_{f,m_f;f`,m_{f`}}$ and $g^{\sigma_-}_{f,m_f;f`,m_{f`}}$ are non-zero only for $m_{f`} = m_f + 1$ and $m_{f`} = m_f - 1$, respectively.

The atom-light interaction Hamiltonian $\hat{H}_I$ in eq. (1.4.3.5) is very general, and now, using this Hamiltonian, we would like to obtain an effective atom-light interaction Hamiltonian, which could reflect the considerations made about the probe laser light in the introductory text of section 1.4. As written in the introductory text of section 1.4, the individual Cesium-133 atoms are coupled off-resonantly to the D_2 line transition $6^2S_{1/2}, f = 4 \rightarrow 6^2P_{3/2}, f` = 5$ by the probe laser light; for that reason the absorption effects become negligible, and so, in $\hat{H}_I$ we can rightfully assume that the excited Zeeman energy level population also becomes negligible such the excited spin states $|f`, m_{f`}>$ can be adiabatically eliminated such that when solving for $\hat{\sigma}_{f,m_f+1;f`,m_f}(x,t)$ and $\hat{\sigma}_{f,m_f-1;f`,m_f}(x,t)$ from the Heisenberg's equation of motion $\frac{\partial}{\partial t}\hat{\sigma}_{f,m_f\pm1;f`,m_f}(x,t) = \frac{1}{i\hbar}\left[\hat{\sigma}_{f,m_f\pm1;f`,m_f}(x,t), \hat{H}_{AL}\right]$ we can set the derivative $\frac{\partial}{\partial t}\hat{\sigma}_{f,m_f\pm1;f`,m_f}(x,t) = 0$, and thus find the solutions to $\hat{\sigma}_{f,m_f+1;f`,m_f}(x,t)$ and $\hat{\sigma}_{f,m_f-1;f`,m_f}(x,t)$ from $\frac{1}{i\hbar}\left[\hat{\sigma}_{f,m_f\pm1;f`,m_f}(x,t), \hat{H}_{AL}\right] = 0$. By plugging the solutions to $\hat{\sigma}_{f,m_f+1;f`,m_f}(x,t)$ and $\hat{\sigma}_{f,m_f-1;f`,m_f}(x,t)$, which are similar to the ones found in [1], into the atom-light interaction Hamiltonian $\hat{H}_I$ in eq. (1.4.3.5) we thus find the effective atom-light interaction Hamiltonian dealing with off-resonant $D_2$ line transition $6^2S_{1/2}, f = 4 \rightarrow 6^2P_{3/2}, f` = 5$ to be

$$\hat{H}_I^{\text{eff}} = -\frac{\hbar c \xi \lambda_{D2}^2}{16\pi A \Delta_5} \int_0^L dx\, \rho A \big(2a_0 \hat{S}_0(x,t) + a_1 \hat{S}_z(x,t)\hat{f}_x(x,t) +$$

$$+ 2a_2 \left[\hat{S}_0(x,t)\hat{f}_x^2(x,t) - \hat{S}_x(x,t)\left\{ f_z^2(x,t) - f_y^2(x,t) \right\} - 2\hat{S}_y(x,t)\hat{f}_z(x,t)\hat{f}_y(x,t) \right] \big) \quad , \quad (1.4.3.6)$$

where $\xi = 2\pi \cdot 5.22$ MHz is the natural FWHM line width of the D_2 line transition in units of radians per time [43], λ_{D2} = 852 nm is the wavelength of the D_2 line transition, Δ_5 is the negative angular frequency detuning between ω_0 and the angular frequency of the D_2 line transition

$6^2S_{1/2}, f = 4 \rightarrow 6^2P_{3/2}, f` = 5$. In eq. (1.4.3.6) we have that $\hat{f}_x(x,t)$, $\hat{f}_y(x,t)$ and $\hat{f}_z(x,t)$ are defined through eqs. (3.2.4.2.a-c) with N = 1 and F → f and are made dimensionless, and that $\hat{S}_i(x,t)$, where i = 0, x, y, z, count the number of photons per unit length, which follows from the definitions of the Stokes operators given by eqs. (1.3.5.a-d), and the fact that $\hat{a}(x,t)$ and $\hat{a}^{\dagger}(x,t)$ have units of inverse of square root of length as seen in section 1.4.2.

The coefficients a_0, a_1 and a_2 are in a case of $6^2S_{1/2}, f = 4$ given by

$$a_0 = \frac{1}{4}\left(\frac{1}{1-\Delta_{3,5}/\Delta_5} + \frac{7}{1-\Delta_{4,5}/\Delta_5} + 8\right) \rightarrow 4 \quad , \tag{1.4.3.7.a}$$

$$a_1 = \frac{1}{120}\left(-\frac{35}{1-\Delta_{3,5}/\Delta_5} - \frac{21}{1-\Delta_{4,5}/\Delta_5} + 176\right) \rightarrow 1 \quad , \tag{1.4.3.7.b}$$

$$a_2 = \frac{1}{240}\left(\frac{5}{1-\Delta_{3,5}/\Delta_5} - \frac{21}{1-\Delta_{4,5}/\Delta_5} + 16\right) \rightarrow 0 \quad , \tag{1.4.3.7.c}$$

where $\Delta_{f`,f``}$ is the negative angular frequency difference between the angular frequency of the D_2 line transition $6^2S_{1/2}, f = 4 \rightarrow 6^2P_{3/2}, f` = 3, 4$ and the angular frequency of the $D_2$ line transition $6^2S_{1/2}, f = 4 \rightarrow 6^2P_{3/2}, f` = 5$. The asymptotic limits seen in eqs. (1.4.3.7.a-c) hold for $\Delta_5 \gg \Delta_{f`,f``}$.

Note that according to section 3.1.1 and figure 4 the asymptotic limits seen in eqs. (1.4.3.7.a-c) are justifiable for all experiments described in this thesis.

Note that the effective atom-light interaction Hamiltonian dealing with off-resonant D_2 line transition $6^2S_{1/2}, f = 3 \rightarrow 6^2P_{3/2}, f` = 5$, is similar to the one in eq. (1.4.3.6) and with the coefficients a_0, a_1 and a_2 being different [1].

In order to interpret $\hat{H}_I^{eff}$ in eq. (1.4.3.6) we have that:

1. the term containing a_0 makes the off-resonant electric field of the light emitted by the probe laser to be responsible for the energy splitting of the hyperfine structure energy levels into the Zeeman energy levels; the amount of splitting will depend on the strength of the electric field. This is known as the *Stark effect* and is analogous to the Zeeman effect described in section 1.1: for the Stark effect it is an off-resonant external electric field that shifts the energies of the Zeeman energy levels, and for the Zeeman effect it is an external static magnetic field that field that shifts the energies of the Zeeman energy levels.

2. the term containing a_1 is responsible for the *Faraday rotation* of the atomic total angular momentum operators $\hat{f}_y(x,t), \hat{f}_z(x,t)$ and the Stokes operators $\hat{S}_x(x,t), \hat{S}_y(x,t)$ around the x-axis; this effect is apparent from the propagation equations (1.4.4.4.a-f) in section 1.4.4.

3. the term containing a_2 is responsible for the higher order coupling between the light of the probe laser and the Cesium-133 atoms; the effect of this term is discussed in detail in [1].

1.4.4 The propagation equations for the atom-light system

In this subsection I will find the propagation equations for the operators $\hat{J}_i(x,t)$ and $\hat{S}_i(x,t)$, where i = x, y, z.

The Heisenberg's equation of motion for the atomic total angular momentum operators $\hat{f}_i(z,t)$ will read as

$$\frac{\partial}{\partial t}\hat{f}_i(x,t) = \frac{1}{i\hbar}\left[\hat{f}_i(x,t), \hat{H}_{AL}\right] \quad => \tag{1.4.4.1.a}$$

$$\frac{\partial}{\partial t}\hat{f}_i(x,t) = \frac{1}{i\hbar}\left[\hat{f}_i(x,t), \hat{H}_I^{eff}\right] \quad ; \tag{1.4.4.2}$$

and the Heisenberg's equation of motion for the Stokes operators $\hat{S}_i$ will become the Maxwell-Bloch equation [1]:

$$\frac{\partial}{\partial t}\hat{S}_i(x,t) = \frac{1}{i}\left[\hat{S}_i(x,t), \hat{H}_{AL}\right] \quad => \tag{1.4.4.1.b}$$

$$\left(\frac{\partial}{\partial t} + c\cdot\frac{\partial}{\partial x}\right)\hat{S}_i(x,t) = \frac{1}{i}\left[\hat{S}_i(x,t), \hat{H}_I^{eff}\right] \quad . \tag{1.4.4.3}$$

Assume now that the retardation effects are not present, i.e. the dynamics on the time scale L/c, where light at speed c travels through the sample of length L, do not contribute; under this assumption we have that $\frac{\partial}{\partial t}\hat{S}_i(x,t) \to 0$ in the Maxwell-Bloch equation (1.4.4.3). By plugging $\hat{H}_I^{eff}$ in eq. (1.4.3.6) with the asymptotic values of a_0, a_1, a_2 in eq. (1.4.3.7), i.e. $a_0 = 4$, $a_1 = 1$, $a_2 = 0$, since we are dealing with the energy level $6^2S_{1/2}, f = 4$ and as mentioned in section 1.4.3 $\Delta_5 \gg \Delta_{f`,f``}$ is justifiable for all experiments described in this thesis, into eqs. (1.4.4.2) and (1.4.4.3), we obtain the following equations of motion for the operators $\hat{f}_i$ and $\hat{S}_i$:

$$\frac{\partial}{\partial t}\hat{f}_x(x,t) = 0 \quad , \tag{1.4.4.4.a}$$

$$\frac{\partial}{\partial t}\hat{f}_y(x,t) = -ca\hat{S}_z(z,t)\hat{f}_z(x,t) \quad , \tag{1.4.4.4.b}$$

$$\frac{\partial}{\partial t}\hat{f}_z(x,t) = +ca\hat{S}_z(z,t)\hat{f}_y(x,t) \quad , \tag{1.4.4.4.c}$$

$$\frac{\partial}{\partial x}\hat{S}_x(x,t) = -a\hat{S}_y(x,t)\hat{f}_x(x,t) \quad , \tag{1.4.4.4.d}$$

$$\frac{\partial}{\partial x}\hat{S}_y(x,t) = +a\hat{S}_x(x,t)\hat{f}_x(x,t) \quad , \tag{1.4.4.4.e}$$

$$\frac{\partial}{\partial x}\hat{S}_z(x,t) = 0 \quad , \tag{1.4.4.4.f}$$

where $a \equiv -\frac{\xi\lambda_{D2}^2}{16\pi A\Delta_5}$, which is dimensionless. From these equations we see the following effects of the dipole interaction between the individual Cesium-133 atoms in the sample and the light emitted by the probe laser as it travels in the x-direction through the atomic sample:

1. the atomic total angular momentum operators $\hat{f}_y(x,t), \hat{f}_z(x,t)$ will Faraday rotate around the x-axis by an amount proportional to the Stokes operator $\hat{S}_z(x,t)$, while the atomic total angular momentum operator $\hat{f}_x(x,t)$ will be unaffected by the interaction.

2. the Stokes operators $\hat{S}_x(x,t), \hat{S}_y(x,t)$ will Faraday rotate around the x-axis by an amount proportional to the atomic total angular momentum operator $\hat{f}_x(x,t)$, while the Stokes operator $\hat{S}_z(x,t)$ will be unaffected by the interaction.

Now, as will be seen in chapter 4, the most essential physical setting for the atom-membrane entanglement experiment is where the Cesium-133 atomic ensemble total angular momentum operator along the quantization-axis, being the z-axis, can be treated as a macroscopic quantity, and the light emitted by the probe laser is travelling in the x-direction through the atomic sample. Since according to section 3.1.1 the probe laser light is linearly-polarized, and assuming that it is the z-direction along which the probe laser light is linearly-polarized, then in the entanglement experiment and other performed experiments that have a similar setting, we have, when observing section 1.2 and eq. (1.3.8), that $\hat{f}_z(x,t) \to \hbar f_z(x,t)$, $\hat{S}_x(x,t) \to S_x(x,t)$, where $f_z(x,t)$ and $S_x(x,t)$ are real numbers, and thus the RHS of eqs. (1.4.4.4.c) and (1.4.4.4.d) is zero; furthermore, in continuous notation the vector operator $\hat{\mathbf{J}}$ becomes

$$\hat{\mathbf{J}}(t) \equiv \int_0^L dz\, \rho A\, \hat{\mathbf{f}}(x,t) \tag{1.4.4.5}$$

(where $\hat{\mathbf{J}}$ in eq. (1.2.1) was defined using discrete notation), and here we let $\hat{J}_z(t) \to \hbar J_z(t) = \hbar J_z$, where J_z is a real number defined in section 1.2, which is of the order of the number of Cesium-133 atoms in the sample. Define also the Stokes operators

$$\hat{S}_i(t) \equiv c\hat{S}_i(x,t) \quad , \tag{1.4.4.6.a}$$
$$\hat{S}_i^{in}(t) \equiv c\hat{S}_i(x=0,t) \quad , \tag{1.4.4.6.b}$$
$$\hat{S}_i^{out}(t) \equiv c\hat{S}_i(x=L,t) \quad , \tag{1.4.4.6.c}$$

where $\hat{S}_i^{in}(t)$ and $\hat{S}_i^{out}(t)$ refer to the Stokes operators at the beginning and at the end of the sample of the length L, respectively. Note that by multiplying by c, we have that $\hat{S}_i(t)$, where i = x, y, z count the number of photons per unit time, because $\hat{S}_i(x,t)$ count the number of photons per unit length, as seen in section 1.4.3. Summarizing the above we thus have that eqs. (1.4.4.4.a-f) yield the following propagation equations relevant for the atom-light system:

$$\hat{S}_z^{out}(t) = \hat{S}_z^{in}(t) \quad , \tag{1.4.4.7.a}$$
$$\hat{S}_y^{out}(t) = \hat{S}_y^{in}(t) + aS_x\hat{J}_x(t) \quad , \tag{1.4.4.7.b}$$
$$\frac{d}{dt}\hat{J}_x(t) = 0 \quad , \tag{1.4.4.7.c}$$
$$\frac{d}{dt}\hat{J}_y(t) = -aJ_z\hat{S}_z^{in}(t) \quad . \tag{1.4.4.7.d}$$

where $S_x = S_x(t)$ has units of inverse of time, and $\hbar = 1$ is assumed.

Note that from now on, whenever S_x will be written in this thesis, it will have units of inverse of time.

Note that the LHS and RHS of eqs. (1.4.4.7.a-d) have the same dimension.

From eq. (1.4.4.7.b) we see that the term $aS_x\hat{J}_x(t)$ allows us to read out the atomic property $\hat{J}_x(t)$ from the light property $\hat{S}_y^{out}(t)$, and from eq. (1.4.4.7.d) we see that another light property $\hat{S}_z^{in}(t)$ is at the same time mapping onto another atomic property $\hat{J}_y(t)$ – we denote such and similar effects as *light back-action*.

The same propagation eq. (1.4.4.7.b) essentially tells us that the Cesium-133 atoms perform *polarization modulation* of the probe laser light, because as understood from section 1.3 and eqs. (1.3.5.b-d), the Stokes vectors can be said to characterize the polarization of light.

Also, from eqs. (1.4.4.7.b) and (1.4.4.7.c) we see that a measurement on $\hat{S}_y^{out}(t)$ will result in a quantum non-demolition (QND) measurement of $\hat{J}_x(t)$, because according to eq. (1.4.4.7.c) $\hat{J}_x(t)$ is not affected by light back-action during the interaction thus ensuring that the state of $\hat{J}_x(t)$ is not demolished.

1.4.5 The scaled atomic ensemble total angular momentum operators, the scaled Stokes operators, and the transformed propagation equations for the atom-light system

In chapter 2, where atom-membrane entanglement protocol is described, we will be using the scaled atomic ensemble total angular momentum operators

$$\hat{x}_a = \hat{x}_a(t) \equiv \frac{\hat{J}_x(t)}{\sqrt{J_z}} \quad , \tag{1.4.5.1.a}$$

$$\hat{p}_a = \hat{p}_a(t) \equiv \frac{\hat{J}_y(t)}{\sqrt{J_z}} \quad , \tag{1.4.5.1.b}$$

where $\hbar = 1$ is assumed such that $\hat{x}_a$ and $\hat{p}_a$ are dimensionless and satisfy the canonic commutation relation $[\hat{x}_a(t), \hat{p}_a(t)] = i$ as seen from eq. (1.2.3.a), and we will also be using the scaled Stokes operators

$$\hat{x}_L(z) = \hat{x}_L(x,t) \equiv \frac{\hat{S}_z(t)}{\sqrt{S_x}} \quad , \tag{1.4.5.1.c}$$

$$\hat{p}_L(z) = \hat{p}_L(x,t) \equiv \frac{\hat{S}_y(t)}{\sqrt{S_x}} \quad , \tag{1.4.5.1.d}$$

which have units of inverse of square root of time, because S_x, $\hat{S}_y(t)$ and $\hat{S}_z(t)$ have units of inverse of time as mentioned in section 1.4.4.

In the present we assume that almost all of the probe laser photons are linearly-polarized along the z-direction, such that the operators $\hat{a}_z(x,t) \to \langle \hat{a}_z(x,t) \rangle = i|\alpha_z(x,t)|$, $\hat{a}_z^\dagger(x,t) \to \langle \hat{a}_z^\dagger(x,t) \rangle =$

$-i|\alpha_z(x,t)|$, where $\alpha_z(x,t)$ is a complex number representing the complex amplitude of the photonic ensemble of the probe laser light pulse at position x and time t, and thus the Stokes operators

$$\hat{S}_x(t) \to S_x(t) \approx -\frac{|\alpha_z(x,t)|^2}{2} \approx -\frac{C_{ph,t}}{2} \quad , \tag{1.4.5.2.a}$$

$$\hat{S}_y(t) \to \frac{|\alpha_z(x,t)|}{i2}(\hat{a}_y(x,t) - \hat{a}_y^\dagger(x,t)) \quad , \tag{1.4.5.2.b}$$

$$\hat{S}_z(t) \to \frac{|\alpha_z(x,t)|}{2}(\hat{a}_y(x,t) + \hat{a}_y^\dagger(x,t)) \quad . \tag{1.4.5.2.c}$$

Note that eq. (1.4.5.2.a) holds, since here we have $\hat{S}_x(t) \to \langle \hat{S}_x(t) \rangle = S_x \equiv \langle \frac{1}{2}\left(\hat{n}_y(x,t) - \hat{n}_z(x,t)\right) \rangle \approx -\frac{1}{2}\langle \hat{n}_z(x,t) \rangle = -\frac{|\alpha_z(t)|^2}{2} \approx -\frac{C_{ph,t}}{2}$, when using eq. (1.3.5.b).

From eqs. (1.4.2.9), (1.4.5.1.c-d) and (1.4.5.2.a-c) it follows that $\hat{x}_L(x)$ and $\hat{p}_L(x)$ satisfy the canonic commutation relation $[\hat{x}_L(x,t), \hat{p}_L(x,t')] = i\delta(t-t')$.

In eqs. (1.4.5.1.a-d) we have $J_z = J_z(t) \equiv 4C_{a,t}$, which follows from the definition $J_z \equiv 4C_a$ in section 1.2, and $S_x = S_x(t) \approx -\frac{C_{ph,t}}{2}$, which is seen in eq. (1.4.5.2.a). Here, in the present case, $C_{a,t} \in \mathbb{N}$ denotes a *large* number of Cesium-133 atoms in the coherent spin state $|F = 4, m_F = 4>$ at time t, and $C_{ph,t} \in \mathbb{N}$ denotes a *large* number of linearly-polarized probe laser photons per unit time at position x.

By making use of the scaled operators given by eqs. (1.4.5.1.a-d), when eqs. (1.4.5.2.a-c) hold, we have that the propagation equations (1.4.4.7.a-d) transform to

$$\hat{x}_L^{out} = -\hat{x}_L^{in} \quad , \tag{1.4.5.3.a}$$

$$\hat{p}_L^{out} = -\hat{p}_L^{in} - \kappa\sqrt{\frac{2}{\tau}}\hat{x}_a \quad , \tag{1.4.5.3.b}$$

$$\frac{d}{dt}\hat{x}_a = 0 \quad , \tag{1.4.5.3.c}$$

$$\frac{d}{dt}\hat{p}_a = \kappa\sqrt{\frac{2}{\tau}}\hat{x}_L^{in} \quad , \tag{1.4.5.3.d}$$

where $\hat{x}_L^{in} \equiv \hat{x}_L(x=0)$, $\hat{x}_L^{out} \equiv \hat{x}_L(x=L)$, $\hat{p}_L^{in} \equiv \hat{p}_L(x=0)$, $\hat{p}_L^{out} \equiv \hat{p}_L(x=L)$, and $\kappa \equiv a\sqrt{\frac{S_x J_z}{2}\tau} = -a\sqrt{C_{ph,t}C_{a,t}\tau}$ will be referred to as the atom-light coupling strength, where τ is the time period of the probe laser pulse. κ is here seen to be dimensionless; this follows from the fact that $a \equiv -\frac{\xi\lambda_{D2}^2}{16\pi A\Delta_5}$ is dimensionless, $C_{a,t}$ is dimensionless and $C_{ph,t}$ has units of inverse of time.

Note that the LHS and RHS of eqs. (1.4.5.3.a-d) have the same dimension.

The propagation equations (1.4.5.3.a-d) will in chapter 2 aid us in understanding the atom-membrane entanglement protocol.

Note that in appendix C, where balanced homodyne detection is briefly described, we can see how one can experimentally measure $\hat{x}_L^{out} \propto \hat{S}_z^{out}(t)$ and $\hat{p}_L^{out} \propto \hat{S}_y^{out}(t)$.

1.5 The effect of an externally applied static magnetic field on the transformed propagation equations for the atom-light system

In order to understand the main effects of an externally applied static magnetic field **B** on the Cesium-133 atoms in all of the experiments described in this thesis it is sufficient to consider the Hamiltonian

$$\hat{H}_{B_{static}} = \frac{\mu_B g}{\hbar}\hat{\mathbf{J}}(t) \bullet \mathbf{B} \quad , \tag{1.5.1}$$

where μ_B is the Bohr magneton and g is the Landé g-factor. Now, when the static magnetic field **B** is pointing along the z-axis in our experiments, we have that $\hat{H}_{B_{static}}$ in eq. (1.5.1) will read as

$$\hat{H}_{B_{static}} = \frac{\mu_B g}{\hbar}\hat{J}_z(t)B_z = \frac{\mu_B g}{\hbar}\hat{J}_z(t)B_{static} = \Omega_L\hat{J}_z(t) \quad , \tag{1.5.2}$$

where $B_z = B_{static}$, and $\Omega_L \equiv \frac{\mu_B g}{\hbar}B_{static}$ is the Larmor frequency of the Cesium-133 atoms in our experiments. Ω_L defines the angular frequency at which $\hat{J}_x(t)$ and $\hat{J}_y(t)$ will precess around the direction of **B**, namely the z-axis. Note that $\hat{H}_{B_{static}}$ makes all the Zeeman energy levels m_F of the Cesium-133 atoms in the performed experiments non-degenerate as understood from appendix A, and that it forces us to use the direction of **B**, which in the present case is the z-axis, as the quantization axis. If we now include the effect of $\hat{H}_{B_{static}}$ into eqs. (1.4.4.2) and (1.4.4.3) for the operators $\hat{f}_i(z,t)$ and $\hat{S}_i(z,t)$, respectively, where i = x, y, z, we have that, when using the commutation relations (1.2.3.b), eqs. (1.4.5.3.a-d) turn into

$$\hat{x}_L^{out} = -\hat{x}_L^{in} \quad , \tag{1.5.3.a}$$

$$\hat{p}_L^{out} = -\hat{p}_L^{in} - \kappa\sqrt{\frac{2}{\tau}}\hat{x}_a \quad , \tag{1.5.3.b}$$

$$\frac{d}{dt}\hat{x}_a = -\Omega_L\hat{p}_a \quad , \tag{1.5.3.c}$$

$$\frac{d}{dt}\hat{p}_a = +\Omega_L\hat{x}_a + \kappa\sqrt{\frac{2}{\tau}}\hat{x}_L^{in} \quad . \tag{1.5.3.d}$$

It is important to note that the similar equations as the ones above can be shown hold for Cesium-133 atoms inside a low-finesse [2] Fabry-Perot-type cavity [12].

Now, as $\hat{x}_a \propto \hat{J}_x(t)$ and $\hat{p}_a \propto \hat{J}_y(t)$ will precess around the x-axis at the Larmor frequency Ω_L, we for convenience switch to the rotating frame, where we use new operators $\hat{x}_a^*$ and $\hat{p}_a^*$ that are related to $\hat{x}_a$ and $\hat{p}_a$ through a 2×2 rotation matrix:

[2] A dimensionless parameter called the optical finesse F gives the average number of roundtrips before a photon leaves a cavity.

$$\begin{pmatrix} \hat{x}_a^* \\ \hat{p}_a^* \end{pmatrix} = \begin{pmatrix} \cos(\Omega_L t) & \sin(\Omega_L t) \\ -\sin(\Omega_L t) & \cos(\Omega_L t) \end{pmatrix} \begin{pmatrix} \hat{x}_a \\ \hat{p}_a \end{pmatrix} \quad . \tag{1.5.4}$$

Observing eq. (1.5.4) it is clear that once we'll know $\hat{x}_a^*$ and $\hat{p}_a^*$, then we'll know $\hat{x}_a$ and $\hat{p}_a$, and vice versa.

The propagation equations (1.5.3.a-d) are in the rotating frame therefore written as follows:

$$\hat{x}_L^{out} = -\hat{x}_L^{in} \quad , \tag{1.5.5.a}$$

$$\hat{p}_L^{out} = -\hat{p}_L^{in} - \kappa\sqrt{\frac{2}{\tau}}(-\hat{p}_a^* \sin(\Omega_L t) + \hat{x}_a^* \cos(\Omega_L t)) \quad , \tag{1.5.5.b}$$

$$\frac{d}{dt}\hat{x}_a^* = \kappa\sqrt{\frac{2}{\tau}}\,\hat{x}_L^{in}\sin(\Omega_L t) \quad , \tag{1.5.5.c}$$

$$\frac{d}{dt}\hat{p}_a^* = \kappa\sqrt{\frac{2}{\tau}}\,\hat{x}_L^{in}\cos(\Omega_L t) \quad , \tag{1.5.5.d}$$

where eq. (1.5.5.b) is obtained by plugging the expression for $\hat{x}_a$ in eq. (1.5.4) into eq. (1.5.3.b), and eqs. (1.5.5.c) and (1.5.5.d) are obtained by differentiating $\hat{x}_a^*$ and $\hat{p}_a^*$ in eq. (1.5.4) with respect to time t, then the product rule for derivatives is used and then eqs. (1.5.3.c) and (1.5.3.d) are used.

The result of eq. (1.5.5.b) tells us that when an externally applied static magnetic field subjects the Cesium-133 atoms and it is homogeneously pointing along the same direction, being the z-direction, and $\hat{p}_L^{out}$ is measured, we will simultaneously access information about $\hat{x}_a^*$ and $\hat{p}_a^*$. However, we see from eqs. (1.5.5.c) and (1.5.5.d) that $\hat{x}_L^{in}$ is during the interaction piling light back-action onto $\hat{x}_a^*$ and $\hat{p}_a^*$ such that the states of $\hat{x}_a^*$ and $\hat{p}_a^*$ are demolished during the interaction. This contrasts the propagation eqs. (1.4.4.7.a-d) (and eqs. (1.4.5.3.a-d)), because in the present case we see that we no longer can perform QND measurements of any kind.

By solving for $\hat{x}_a^*$ and $\hat{p}_a^*$ in eqs. (1.5.5.c) and (1.5.5.d) we obtain

$$\hat{x}_a^* = \hat{x}_a^*(t) = \hat{x}_a^*(0) + \kappa\sqrt{\frac{2}{\tau}}\int_0^t dt'\,\hat{x}_L^{in}(t')\sin(\Omega_L t') \quad , \tag{1.5.6.a}$$

$$\hat{p}_a^* = \hat{p}_a^*(t) = \hat{p}_a^*(0) + \kappa\sqrt{\frac{2}{\tau}}\int_0^t dt'\,\hat{x}_L^{in}(t')\cos(\Omega_L t') \quad . \tag{1.5.6.b}$$

By plugging the above expressions for $\hat{x}_a^*$ and $\hat{p}_a^*$ into eq. (1.5.5.b) we observe that as $\hat{x}_L^{in}(t)$ is during the interaction piling light back-action onto $\hat{x}_a^*$ and $\hat{p}_a^*$, then $\hat{x}_L^{in}(t')$ is being transferred onto $\hat{p}_L^{out}(t)$, for all times $t' < t$. This kind of feedback is referred to as *light back-action noise*.

1.6 The cavity optomechanical system Hamiltonian

In this section I will consider treating a cavity optomechanical system depicted in figure 2. It consists of an optical Fabry-Perot cavity, where one of the mirrors is stationary and allows light field to be transmitted into the cavity, and the second mirror is dynamic, exhibiting pendulum-like motion. The dynamic mirror acts as a mechanical resonator.

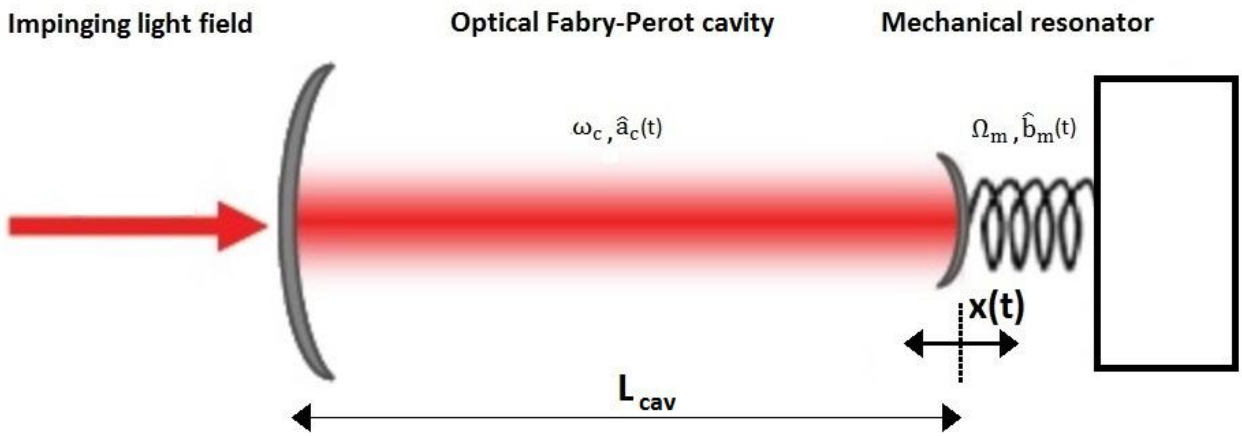

Figure 2. A schematic for a generic geometry of a cavity optomechanical system. It consists of an optical Fabry-Perot cavity, where the left mirror is assumed to be stationary and allows light field to be transmitted into the cavity, and the right mirror is dynamic, exhibiting pendulum-like motion, where x(t) denotes its position from the equilibrium position, which is where the two mirrors are separated by the distance L_{cav}. The dynamic mirror acts as a mechanical resonator. In the text we focus on a single optical mode of the optical Fabry-Perot cavity and a single mechanical mode of the mechanical resonator. Note that the various parameters seen in this figure are also seen in the text.

The Hamiltonian for a cavity optomechanical system can in general be written as

$$\hat{H}_{om} = \hat{H}_c + \hat{H}_m + \hat{H}_{I,om} + \text{Extra} \quad , \tag{1.6.1}$$

where $\hat{H}_c$ is the optical cavity (a.k.a. optical resonator) Hamiltonian, $\hat{H}_m$ is the mechanical resonator Hamiltonian, $\hat{H}_{I,om}$ is the optomechanical interaction Hamiltonian, and the term "Extra" is associated with cavity photon decay, mechanical friction of the mechanical resonator, influx of thermal phonons and driving by an external laser and/or a fluctuating vacuum field.

In the following three subsections of this section, the three Hamiltonians $\hat{H}_c$, $\hat{H}_m$ and $\hat{H}_{I,om}$ will be put forward; this will be done in the Heisenberg picture, where the quantum operators are time-dependent and quantum states are time-independent. Having found the *linearized* optomechanical interaction Hamiltonian $\hat{H}_{int,om}^{lin}$, the input-output relations for operators that describe light that is transmitted by the optomechanical system will be presented in the fourth subsection of this section. These input-output relations will in chapter 2 aid us in understanding how the atom-membrane entanglement works.

Note that this section also serves to explain the basic principles of the optomechanical system described in section 3.4 that is part of our atom-membrane interfacing experimental setup.

1.6.1 The optical cavity Hamiltonian

An optical Fabry-Perot cavity that consists of two highly reflective mirrors that are separated by a fixed distance L_{cav} has the resonance angular frequencies given by

$$\omega_{cav,n} = n\pi \frac{c}{L_{cav}} \quad , \tag{1.6.1.1}$$

where n is the integer number of the optical (Fabry-Perot) cavity mode. In the following we will focus on a single optical cavity mode, whose angular frequency will be denoted as ω_c.

The Hamiltonian describing the optical cavity is thus that of a single-mode harmonic oscillator and is given by

$$\hat{H}_c = \hbar\omega_c\left(\hat{a}_c^\dagger(t)\hat{a}_c(t) + \frac{1}{2}\right) \quad , \tag{1.6.1.2}$$

where $\hat{a}_c(t)$ and $\hat{a}_c^\dagger(t)$ are the photonic annihilation and creation operators of the optical cavity mode, respectively, that are dimensionless and that satisfy the commutation relation $\left[\hat{a}_c(t)\,,\hat{a}_c^\dagger(t)\right] = 1$.

1.6.2 The mechanical resonator Hamiltonian

To understand the vibrational behavior of a mechanical resonator one can solve the equations of linear theory of elasticity under appropriate boundary conditions that are determined by the geometry of the mechanical resonator. Solving the problem yields a set of equations that can be used to visualize the vibrational shape for the different mechanical modes and the corresponding eigenangularfrequencies $\Omega_{mech,n}$, where n is the integer number of the mechanical mode. In the following we will focus on a single mechanical mode, whose angular frequency will be denoted as Ω_m.

The Hamiltonian describing the mechanical resonator is thus that of a single-mode harmonic oscillator and is given by

$$\begin{aligned}\hat{H}_m &= \hbar\Omega_m\left(\hat{b}_m^\dagger(t)\hat{b}_m(t) + \frac{1}{2}\right) = \\ &= \frac{1}{2}\hat{p}_m^2(t) + \frac{1}{2}\Omega_m^2\hat{x}_m^2(t) \quad ,\end{aligned} \tag{1.6.2.1}$$

where

$$\hat{x}_m = \hat{x}_m(t) \equiv \sqrt{\frac{\hbar}{2m_{eff}\Omega_m}}\left(\hat{b}_m(t) + \hat{b}_m^\dagger(t)\right) \quad , \tag{1.6.2.2.a}$$

$$\hat{p}_m = \hat{p}_m(t) \equiv \sqrt{\hbar m_{eff}\Omega_m}\,\frac{\left(\hat{b}_m(t) - \hat{b}_m^\dagger(t)\right)}{i\sqrt{2}} \tag{1.6.2.2.b}$$

are the position and the momentum operators of the mechanical resonator that respectively have dimensions of square root of time multiplied by dimensions of $\sqrt{\frac{\hbar}{m_{eff}}}$ and the inverse of square root time multiplied by dimensions of $\sqrt{\hbar m_{eff}}$, and that satisfy the canonical commutation relation $[\hat{x}_m(t), \hat{p}_m(t)] = i\hbar$, with $\hat{b}_m(t)$ and $\hat{b}_m^\dagger(t)$ being the phononic annihilation and creation operators of the mechanical mode, respectively, that are dimensionless and that satisfy the commutation relation $\left[\hat{b}_m(t)\,,\hat{b}_m^\dagger(t)\right] = 1$.

1.6.3 The optomechanical interaction Hamiltonian

When the dynamic mirror of the optical Fabry-Perot cavity seen in figure 2 exhibits pendulum-like motion, then the coupling of optical and mechanical modes is parametric, i.e. the resonance angular frequency of the optical Fabry-Perot cavity, $\omega_c(x)$, is modulated by the displacement $x = x(t)$ of the mechanical resonator, and so we can describe $\omega_c(x)$ by the Taylor series

$$\omega_c(x) = \omega_c + x\frac{d\omega_c}{dx} + \cdots = \omega_c + xG + \cdots \ , \tag{1.6.3.1}$$

where $\omega_c = \omega_c(0)$, and $G \equiv \frac{d\omega_c}{dx}$ is the optical angular frequency shift per displacement and is referred to as the frequency-pull parameter.

Expanding now the Hamiltonian $\hat{H}_c$ in eq. (1.6.1.2) (with the vacuum noise term neglected) to leading-order in the displacement x we obtain $\hbar\omega_c(x)\hat{a}_c^\dagger(t)\hat{a}_c(t) \approx \hbar(\omega_c + xG)\hat{a}_c^\dagger(t)\hat{a}_c(t) \rightarrow \hbar(\omega_c + \hat{x}_m G)\hat{a}_c^\dagger(t)\hat{a}_c(t)$, where $x \rightarrow \hat{x}_m \equiv \sqrt{\frac{\hbar}{2m_{eff}\Omega_m}}\left(\hat{b}_m(t) + \hat{b}_m^\dagger(t)\right)$, as defined in equation (1.6.2.2.a); and so the optomechanical interaction Hamiltonian becomes

$$\hat{H}_{I,om} = \hbar G\hat{x}_m\hat{a}_c^\dagger(t)\hat{a}_c(t) \ . \tag{1.6.3.2}$$

The fundamental mechanism that couples the radiation field of the cavity to the motion of the mechanical resonator is the momentum transfer of the cavity photons onto the mechanical resonator, i.e. radiation-pressure force. A single photon transfers the momentum $|\Delta p| = 2\hbar k_c$, where $k_c = \frac{\omega_c}{c}$ is the angular wave number of the cavity photon, in a roundtrip inside the cavity, and as a consequence the radiation-pressure force (operator) is given by

$$\hat{F}_{rad} = \frac{d\hat{H}_{I,om}}{d\hat{x}_m} = \hbar G\hat{a}_c^\dagger(t)\hat{a}_c(t) \ , \tag{1.6.3.3}$$

where $\hat{n}_c(t) \equiv \hat{a}_c^\dagger(t)\hat{a}_c(t)$ is a photon number operator for the cavity photons, and the RHS of the equation equals $\frac{|\Delta p|}{\tau_c}\hat{a}_c^\dagger\hat{a}_c = \hbar\frac{\omega_c}{L_{cav}}\hat{a}_c^\dagger\hat{a}_c$, where $\tau_c = \frac{2L_{cav}}{c}$ is the cavity roundtrip time, where L_{cav} is the length of the cavity, if $G = \frac{d\omega_c}{dx} \approx \frac{\omega_c}{L_{cav}}$. Note that as the motion of the mechanical resonator induces a shift to the resonance angular frequency of the optical cavity mode, a change in the circulating light intensity will happen and so a change in the radiation-pressure force will also happen. This kind of feedback-loop is referred to as *optomechanical back-action*.

Since the mechanical resonator Hamiltonian $\hat{H}_m$ in eq. (1.6.2.1) describes the mechanical resonator exhibiting *mechanical oscillatory motion*, it follows that the radiation-pressure force $\hat{F}_{rad}$ in eq. (1.6.3.3) is a force of varying amplitude, such that $\hat{F}_{rad}$ can be said to deal with light that is *amplitude modulated*.

Note that in chapter 2 the so-called *linearized* approximate description of the optomechanical system will be used. Here we first need to split $\hat{a}_c(t)$ into an average complex amplitude $\overline{\alpha}_c(t) \equiv \langle \hat{a}_c(t) \rangle$ and a fluctuating term $\delta\hat{a}_c(t)$, i.e. $\hat{a}_c(t) = \overline{\alpha}_c(t) + \delta\hat{a}_c(t)$, and plug it in the optomechanical interaction Hamiltonian $\widehat{H}_{I,om}$ in eq. (1.6.3.2), such that $\widehat{H}_{I,om}$ reads as

$$\widehat{H}_{I,om} = \hbar G \hat{x}_m (\overline{\alpha}_c(t) + \delta\hat{a}_c(t))^\dagger (\overline{\alpha}_c(t) + \delta\hat{a}_c(t)) \quad . \tag{1.6.3.4}$$

$\widehat{H}_{I,om}$ in eq. (1.6.3.4) may now be expanded in powers of $\overline{\alpha}_c(t)$. The part of the expanded $\widehat{H}_{I,om}$ that will result in linear (coupled) equations of motion is referred to as the *linearized* optomechanical interaction Hamiltonian $\widehat{H}^{lin}_{int,om}$, and is

$$\widehat{H}^{lin}_{I,om} = \hbar g \hat{x}_m \left(\delta\hat{a}_c(t) + \delta\hat{a}_c^\dagger(t) \right) = g_{m,c} \hat{x}_{m,z} \hat{x}_c \quad , \tag{1.6.3.5}$$

where $g \equiv G\overline{\alpha}_c$, and $g_{m,c} \equiv \hbar \sqrt{\frac{1}{m_{eff}\Omega_m}}\, g = \hbar \sqrt{\frac{1}{m_{eff}\Omega_m}}\, G\overline{\alpha}_c$ with $\overline{\alpha}_c$ assumed to be real, is referred to as the optomechanical coupling strength, $\hat{x}_{m,z} \equiv \left(\hat{b}_m(t) + \hat{b}_m^\dagger(t) \right)$ is $\hat{x}_m$ divided by $\sqrt{\frac{\hbar}{2m_{eff}\Omega_m}}$, such that $\hat{x}_{m,z}$ is dimensionless, and

$$\hat{x}_c = \hat{x}_c(t) \equiv \sqrt{\frac{\hbar}{2}} \left(\delta\hat{a}_c + \delta\hat{a}_c^\dagger \right) \quad , \tag{1.6.3.6.a}$$

$$\hat{p}_c = \hat{p}_c(t) \equiv \sqrt{\hbar}\, \frac{\left(\delta\hat{a}_c - \delta\hat{a}_c^\dagger \right)}{i\sqrt{2}} \tag{1.6.3.6.b}$$

denote the quantum fluctuations of the optical cavity mode. Note that $\hat{x}_c$ and $\hat{p}_c$ have dimensions of $\sqrt{\hbar}$ and satisfy the canonical commutation relation $[\, \hat{x}_c(t), \hat{p}_c(t)] = i\hbar$. Note that $g_{m,c}$ has dimensions of inverse of time multiplied by dimensions of $\sqrt{\hbar}$.

1.6.4 The propagation equations for the cavity optomechanical system

In this subsection I consider finding input-output relations for operators that describe light that is transmitted by the optomechanical system.

From the cavity optomechanical system Hamiltonian $\widehat{H}_{om}$ in eq. (1.6.1) we observe that the cavity optomechanical system is a quantum system that interacts with the environment, which by definition implies that it is an open quantum system, and thus the equations of motion for an operator $\widehat{A}$ of the system will be given by the Lindblad-Heisenberg equation of motion

$$\frac{\partial}{\partial t}\widehat{A} = \frac{1}{i\hbar}\left[\widehat{A}, \widehat{H}_{om,E}\right] + \frac{1}{2\hbar}\sum_{k=1}^{\infty} \left(\hat{L}_k^\dagger \left[\widehat{A}, \hat{L}_k\right] + \left[\hat{L}_k^\dagger, \widehat{A}\right] \hat{L}_k \right) \quad , \tag{1.6.4.1}$$

where $\widehat{H}_{om,E}$ is the optomechanical system Hamiltonian $\widehat{H}_{om}$ in eq. (1.6.1) without the term "Extra", and $\hat{L}_k$ are known as Lindlblad operators, which are operators that model the effects of the environment. Note that $\widehat{H}_{om,E}$ excludes the term "Extra", because as understood from the text below

eq. (1.6.1) this is an environmental term. For the operators $\hat{x}_c$ and $\hat{p}_c$, which are defined in equations (1.6.3.6.a) and (1.6.3.6.b), respectively, that denote the quantum fluctuations of the optical cavity mode, we have that the Lindblad-Heisenberg equations of motion will read as [12]

$$\frac{\partial}{\partial t}\hat{x}_c = \frac{1}{i\hbar}\left[\hat{x}_c, \hat{H}_{om,E}\right] - \eta_c\hat{x}_c - \sqrt{2\eta_c}\hat{x}'^{in}_L \quad , \tag{1.6.4.2.a}$$

$$\frac{\partial}{\partial t}\hat{p}_c = \frac{1}{i\hbar}\left[\hat{p}_c, \hat{H}_{om,E}\right] - \eta_c\hat{p}_c - \sqrt{2\eta_c}\hat{p}'^{in}_L \quad , \tag{1.6.4.2.b}$$

where the operators $\hat{x}'_L(x) = \hat{x}'_L(x,t)$ and $\hat{p}'_L(x) = \hat{p}'_L(x,t)$ represent the fluctuating vacuum field plus the laser field outside of the cavity, such that the operators $\hat{x}'^{in}_L = \hat{x}'^{in}_L(t)$ and $\hat{p}'^{in}_L = \hat{p}'^{in}_L(t)$ represent the fluctuating vacuum field plus the driving laser field entering the cavity from the left mirror in figure 2, and η_c is the total cavity photon decay rate. Note that as understood from the text below eq. (1.6.1) $\hat{x}'_L(x)$ and $\hat{p}'_L(x)$ may also represent *just* the fluctuating vacuum field outside of the cavity, such that $\hat{x}'^{in}_L$ and $\hat{p}'^{in}_L$ represent the fluctuating vacuum field entering the cavity from the left mirror in figure 2. Note as well that $\hat{x}'_L(x)$ and $\hat{p}'_L(x)$ have units of inverse of square root of time multiplied by $\sqrt{\hbar}$ and satisfy the canonical commutation relation $[\hat{x}'_L(x,t), \hat{p}'_L(x,t')] = i\hbar\delta(t-t')$, which, as we observe, is also the case for the scaled Stokes operators $\hat{x}_L(x)$ and $\hat{p}_L(x)$ defined in eqs. (1.4.5.1.c) and (1.4.5.1.d), respectively, but without $\sqrt{\hbar}$. Note therefore that the LHS and RHS of eqs. (1.6.4.2.a-b) have the same dimension.

Using $\hat{H}_{om,E}$ with $\hat{H}^{lin}_{I,om}$ in eq. (1.6.3.5) and the fact that $[\hat{x}_c, \hat{p}_c] = i\hbar$ we have that eqs. (1.6.4.2) now read

$$\frac{\partial}{\partial t}\hat{x}_c = -\eta_c\hat{x}_c - \sqrt{2\eta_c}\hat{x}'^{in}_L \quad , \tag{1.6.4.3.a}$$

$$\frac{\partial}{\partial t}\hat{p}_c = -\eta_c\hat{p}_c - \sqrt{2\eta_c}\hat{p}'^{in}_L - g_{m,c}\hat{x}_{m,z} \quad . \tag{1.6.4.3.b}$$

Note that the LHS and RHS of eqs. (1.6.4.3.a-b) have the same dimension.

Define now the operators $\hat{x}'^{out}_L$ and $\hat{p}'^{out}_L$ as the operators that describe light that is transmitted by the cavity optomechanical system, i.e. light that is transmitted through the dynamic mirror seen in figure 2, or, equivalently, light that is transmitted back through the stationary mirror in figure 2. The boundary conditions for $\hat{x}'^{out}_L$ and $\hat{p}'^{out}_L$ are given by

$$\hat{x}'^{out}_L = \hat{x}'^{in}_L + \sqrt{2\eta_c}\hat{x}_c \quad , \tag{1.6.4.4.a}$$

$$\hat{p}'^{out}_L = \hat{p}'^{in}_L + \sqrt{2\eta_c}\hat{p}_c \quad . \tag{1.6.4.4.b}$$

Now, assume that $\eta_c \gg \Omega_m$ such that one can adiabatically eliminate the optical cavity mode, so $\frac{\partial}{\partial t}\hat{x}_c = 0$ such that from eq. (1.6.4.3.a) one obtains $\frac{\partial}{\partial t}\hat{x}_c = -\eta_c\hat{x}_c - \sqrt{2\eta_c}\hat{x}'^{in}_L = 0$ => $\hat{x}_c = -\sqrt{\frac{2}{\eta_c}}\hat{x}'^{in}_L$, and $\frac{\partial}{\partial t}\hat{p}_c = 0$ such that from eq. (1.6.4.3.b) one obtains $\frac{\partial}{\partial t}\hat{p}_c = -\eta_c\hat{p}_c - \sqrt{2\eta_c}\hat{p}'^{in}_L -$

$g_{m,c}\hat{x}_{m,z} = 0$ => $\hat{p}_c = -\sqrt{\frac{2}{\eta_c}}\hat{p}'^{in}_L - \frac{g_{m,c}}{\eta_c}\hat{x}_m$. Plugging these results for $\hat{x}_c$ and $\hat{p}_c$ into eqs. (1.6.4.4.a-b) one obtains input-output relations for the light operators $\hat{x}'^{out}_L$ and $\hat{p}'^{out}_L$:

$$\hat{x}'^{out}_L = -\hat{x}'^{in}_L \quad , \tag{1.6.4.5.a}$$

$$\hat{p}'^{out}_L = -\hat{p}'^{in}_L - g_{m,c}\sqrt{\frac{2}{\eta_c}}\hat{x}_m \quad . \tag{1.6.4.5.b}$$

These input-output relations will in chapter 2 aid us in understanding how the atom-membrane entanglement works.

Note that in appendix C, where balanced homodyne detection is briefly described, we can see how one can experimentally measure $\hat{x}'^{out}_L$ and $\hat{p}'^{out}_L$.

Chapter 2: Protocol for entanglement generation between Cesium-133 atomic ensemble and nanomechanical membrane resonator

In this chapter I present a protocol for entanglement generation between Cesium-133 atomic ensemble and nanomechanical membrane resonator with the help of the theory from chapter 1. The protocol presented here was first proposed by K. Hammerer et al. [12].

Note that in this chapter it is assumed that $\hbar = 1$.

2.1 Conditions for generating atom-membrane entanglement

Consider two systems respectively described by a pair of canonical operators $\hat{x}_1$, $\hat{p}_1$ and $\hat{x}_2$, $\hat{p}_2$, which obey the canonical commutation relations

$$[\hat{x}_1, \hat{p}_1] = [\hat{x}_2, \hat{p}_2] = i \quad , \tag{2.1.1}$$

and otherwise commute with one another. The two systems are said to be entangled if the following Einstein-Podolsky-Rosen (EPR) variance criterion is fulfilled [2, 3]

$$\sum_{EPR} \equiv \mathrm{Var}\left(\frac{\hat{x}_2+\hat{x}_1}{\sqrt{2}}\right) + \mathrm{Var}\left(\frac{\hat{p}_2-\hat{p}_1}{\sqrt{2}}\right) < 1 \quad , \tag{2.1.2}$$

where $\sum_{EPR}$ is referred to as the EPR variance.

Let now the two systems considered above respectively refer to Cesium-133 atomic ensemble and nanomechanical membrane resonator that is part of an optomechanical system. Let the canonical variables $\hat{x}_1$ and $\hat{p}_1$ respectively refer to the scaled atomic ensemble total angular momentum operators $\hat{x}_a = \hat{x}_a(t)$ and $\hat{p}_a = \hat{p}_a(t)$, which respectively are defined in eqs. (1.4.5.1.a) and (1.4.5.2.b), and let the canonical variables $\hat{x}_2$ and $\hat{p}_2$ respectively refer to the position and the momentum operators of the nanomechanical membrane resonator, $\hat{x}_m = \hat{x}_m(t)$ and $\hat{p}_m = \hat{p}_m(t)$, which respectively are defined in eqs. (1.6.2.2.a) and (1.6.2.2.b). Note that the pairs of operators $\hat{x}_a$, $\hat{p}_a$ and $\hat{x}_m$, $\hat{p}_m$ satisfy the canonical commutation relations $[\hat{x}_a(t), \hat{p}_a(t)] = i$, $[\hat{x}_m(t), \hat{p}_m(t)] = i$ as seen previously in chapter 1; and so, from eq. (2.1.2) we have that the Cesium-133 atomic ensemble and the nanomechanical membrane resonator are entangled if the inequality

$$\sum_{EPR} \equiv \mathrm{Var}\left(\frac{\hat{x}_m+\hat{x}_a}{\sqrt{2}}\right) + \mathrm{Var}\left(\frac{\hat{p}_m-\hat{p}_a}{\sqrt{2}}\right) < 1 \tag{2.1.3}$$

holds.

Let us now consider describing a protocol, which deals with entanglement generation between Cesium-133 atomic ensemble and nanomechanical membrane resonator.

In figure 3 we can see a schematic of the setup that allows us to entangle the Cesium-133 atomic ensemble with the nanomechanical membrane resonator. Here the (Cesium-133) atomic ensemble is seen to be interfaced together with the (nanomechanical) membrane resonator via light bus. Entanglement can be generated by measuring the light that has interfaced the atomic ensemble and the membrane resonator. In figure 3 we will refer to the part of the setup that is to the left of the filter as the atomic part of the setup, and the part of the setup that is to the right of the filter as the optomechanical part of the setup. The light in the atomic part of the setup is described by the scaled Stokes operators $\hat{x}_L(x) = \hat{x}_L(x,t)$ and $\hat{p}_L(x) = \hat{p}_L(x,t)$, which respectively are defined in equations (1.4.5.1.c) and (1.4.5.1.d); and the light in the optomechanical part of the setup is described by the operators $\hat{x}'_L(x) = \hat{x}'_L(x,t)$ and $\hat{p}'_L(x) = \hat{p}'_L(x,t)$, which are defined in section 1.6.4, and the operators $\hat{x}_c = \hat{x}_c(t)$ and $\hat{p}_c = \hat{p}_c(t)$, which respectively are defined in equations (1.6.3.6.a) and (1.6.3.6.b). Note that the pairs of operators $\hat{x}_L(x)$, $\hat{p}_L(x)$ and $\hat{x}'_L(x)$, $\hat{p}'_L(x)$, and $\hat{x}_c, \hat{p}_c$ satisfy the canonical commutation relations $[\hat{x}_L(x,t), \hat{p}_L(x,t)] = i\delta(t-t')$, $[\hat{x}'_L(x,t), \hat{p}'_L(x,t)] = i\delta(t-t')$, $[\hat{x}_c(t), \hat{p}_c(t)] = i$ as seen in chapter 1. Note as well that according to chapter 1 we have $\hat{x}_L^{in} \equiv \hat{x}_L(x)$, $\hat{p}_L^{in} \equiv \hat{p}_L(x)$, where the position x is before the atomic ensemble, $\hat{x}_L^{out} \equiv \hat{x}_L(x)$, $\hat{p}_L^{out} \equiv \hat{p}_L(x)$, where the position x is after the atomic ensemble and before the filter, $\hat{x}'^{in}_L \equiv \hat{x}'_L(x)$, $\hat{p}'^{in}_L \equiv \hat{p}'_L(x)$, where the position x is after the filter and before the cavity, $\hat{x}'^{out}_L \equiv \hat{x}'_L(x)$, $\hat{p}'^{out}_L \equiv \hat{p}'_L(x)$, where the position x is after the cavity and before the detection.

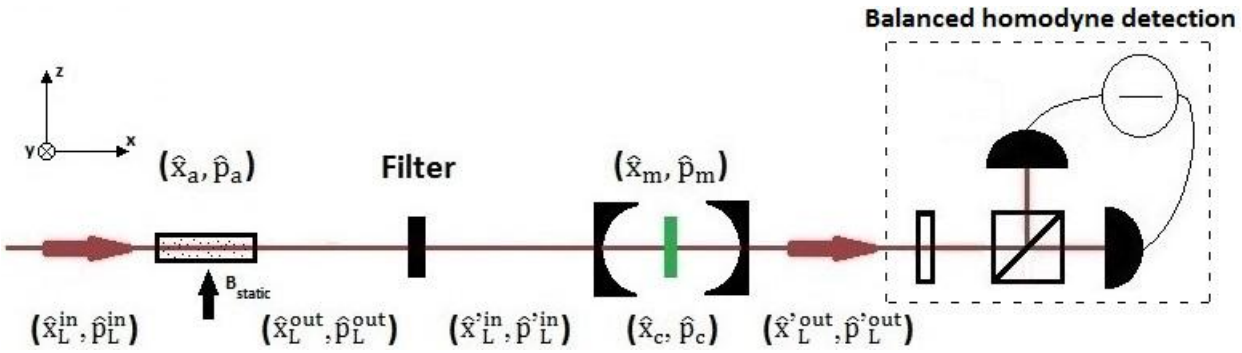

Figure 3. A schematic of the setup used for entanglement generation between Cesium-133 atomic ensemble and nanomechanical membrane resonator. A pulse of light described by the operators $\hat{x}_L^{in}$ and $\hat{p}_L^{in}$ interacts first with the atomic ensemble described by the operators $\hat{x}_a$ and $\hat{p}_a$ that are precessing at the Larmor frequency around the z-axis due to a static magnectic field $\mathbf{B}_{static}$ pointing along the z-axis. After the light has interacted with the atoms, it is described by the operators $\hat{x}_L^{out}$ and $\hat{p}_L^{out}$. As understood from the propagation equations (1.4.5.3.a-b) and as noted in the text of section 1.4.4 we have that as the light interacts with the atoms, it becomes polarization modulated. Now, since as understood from section 1.6.3 the fundamental mechanism that couples the radiation field of the cavity to the motion of the membrane resonator is the radiation-pressure force described by the operator $\hat{F}_{rad}$ in eq. (1.6.3.3), and $\hat{F}_{rad}$ deals with light that is amplitude modulated, and since it is the light after the atoms that one needs the membrane resonator to respond to, one builds a filter that can convert the polarization modulated light into amplitude modulated light. After the filter, the light is described by the operators $\hat{x}'^{in}_L$ and $\hat{p}'^{in}_L$ and it interacts with the membrane resonator described by the operators $\hat{x}_m$ and $\hat{p}_m$, because according to Lindblad-Heisenberg equation of motion (1.6.4.2) we have that the operators $\hat{x}'^{in}_L$ and $\hat{p}'^{in}_L$ affect the time evolution of the operators $\hat{x}_c$ and $\hat{p}_c$ that are used to describe the optical cavity mode. Light leaving the cavity is described by the operators $\hat{x}'^{out}_L$ and $\hat{p}'^{out}_L$, and it is subject to balanced homodyne detection, whose basic principals are described in appendix C.

Let us now understand why the light that is subject to detection carries information about the commuting *EPR observables* $\hat{x}_m + \hat{x}_a$ and $\hat{p}_m - \hat{p}_a$.

To start, it is proposed that the Hamiltonians that respectively describe the atomic ensemble and the membrane resonator are structurally similar.

In order to obtain structural similarity between these two Hamiltonians, one chooses to model the atomic ensemble as a negative-mass (single-mode) harmonic oscillator, and the membrane resonator as a positive-mass (single-mode) harmonic oscillator, such that the respective Hamiltonians of these two systems become

$$\widehat{H}_{\text{atoms}} = \frac{1}{2}\hat{p}_a^2 + \frac{1}{2}\Omega_{L,n}^2\hat{x}_a^2 = \frac{\Omega_{L,n}}{2}\left(\widehat{P}_a^2 + \widehat{X}_a^2\right) \quad , \tag{2.1.4.a}$$

$$\widehat{H}_{\text{membrane}} = \frac{1}{2}\hat{p}_m^2 + \frac{1}{2}\Omega_m^2\hat{x}_m^2 = \frac{\Omega_m}{2}\left(\widehat{P}_m^2 + \widehat{X}_m^2\right) \quad , \tag{2.1.4.b}$$

where both oscillators are assumed to be of unit mass, $\widehat{P}_a \equiv \frac{\hat{p}_a}{\sqrt{\Omega_{L,n}}}$, $\widehat{P}_m \equiv \frac{\hat{p}_m}{\sqrt{\Omega_m}}$, $\widehat{X}_a \equiv \sqrt{\Omega_{L,n}}\hat{x}_a$, $\widehat{X}_m \equiv \sqrt{\Omega_m}\hat{x}_m$, and $\Omega_{L,n} < 0$ is the *negative* angular frequency of the splitting between the Zeeman energy levels $m_F = 3$ and $m_F = 4$ of the energy level $6^2S_{1/2}$, F = 4 of the atoms, and $\Omega_m > 0$ is the *positive* angular frequency of the mechanical mode of the membrane resonator. $\Omega_{L,n}$ is non-zero, because the atoms are subject to a static magnetic field $\mathbf{B}_{\text{static}}$ as seen in figure 3, and so the $m_F -$ levels are made non-degenerate as understood from appendix A; and Ω_m is non-zero, because the membrane resonator exhibits mechanical oscillatory motion. Also, the reason why $\Omega_{L,n}$ is negative, is because the atomic ensemble is modeled as a negative-mass harmonic oscillator, and the reason why Ω_m is positive, is because the membrane resonator is modeled as a positive-mass harmonic oscillator.

The main difference between negative- and positive-mass oscillators is as follows: in order for a negative-mass oscillator to create a quantum excitation, a quantum of energy must be extracted, instead of being supplied, which is the case for a positive-mass oscillator; ergo $\Omega_{L,n}$ must be negative, because the energy of $6^2S_{1/2}$, F = 4, $m_F = 3$ is smaller than that of $6^2S_{1/2}$, F = 4, $m_F = 4$ as seen in figure A1 in appendix A.

In order for the atomic ensemble to be modeled as a negative-mass harmonic oscillator we assume that all the atoms reside either in the coherent spin state $|F = 4, m_F = 4>$ or the spin state $|F = 4, m_F = 3>$, and say that when all the atoms are in $|4,4>$, then the atomic ensemble is in the ground state $|0\rangle \equiv |+\rangle^{\otimes C_{a,t}}$ of the negative-mass harmonic oscillator, and when all the atoms are in $|4,3>$, then the atomic ensemble is in the state $|-\rangle^{\otimes C_{a,t}}$ of the negative-mass harmonic oscillator, where "$\otimes C_{a,t}$" refers to the $C_{a,t}$'th tensor power. Recall from section 1.4.5 that the number $C_{a,t}$ appears in the definition of $J_z = J_z(t)$, i.e. there $J_z \equiv 4C_{a,t}$, where $C_{a,t}$ denotes a large number of Cesium-133 atoms in the coherent spin state $|F = 4, m_F = 4>$ at time t. The excited states of the oscillator are given by $|1\rangle \equiv \hat{a}_a^\dagger|0\rangle$, $|2\rangle \equiv \hat{a}_a^\dagger|1\rangle$, etc., where $\hat{a}_a^\dagger \equiv \frac{1}{\sqrt{C_{a,t}}}\hat{J}_{a,+}$, where $\hat{J}_{a,+} \equiv \sum_i^{C_{a,t}} |-\rangle_i\langle+|_i$ is the raising operator of the oscillator, such that $\hat{a}_a^\dagger|-\rangle^{\otimes C_{a,t}} = 0$; and $\hat{a}_a \equiv \frac{1}{\sqrt{C_{a,t}}}\hat{J}_{a,-}$, where $\hat{J}_{a,-} \equiv \sum_i^{C_{a,t}} |+\rangle_i\langle-|_i$ is the lowering operator of the oscillator, such that $\hat{a}_a|+\rangle^{\otimes C_{a,t}} = 0$. We

observe that when one of the atoms in the atomic ensemble is in $|4,3>$, then the atomic ensemble is in the first excited state $|1\rangle$ of the negative-mass harmonic oscillator, etc.

By observing section 1.6.2, and eq. (1.6.2.1) we see that one can model the membrane resonator as a positive-mass harmonic oscillator. Note that $\widehat{H}_{membrane}$ in eq. (2.1.4.b) is $\widehat{H}_m$ in eq. (1.6.2.1) with $m_{eff} = 1$.

As understood from eq. (1.5.2) $\Omega_{L,n} \equiv -\Omega_L$, where Ω_L is the Larmor frequency, i.e. the angular frequency at which $\widehat{X}_a$ and $\widehat{P}_a$ will precess around the direction of the static magnetic field $\mathbf{B}_{static}$ seen in figure 3, namely the z-axis.

Note that the pairs of operators $\widehat{X}_a$, $\widehat{P}_a$ and $\widehat{X}_m$, $\widehat{P}_m$ satisfy the canonical commutation relations, because the pairs of operators $\hat{x}_a$, $\hat{p}_a$ and $\hat{x}_m$, $\hat{p}_m$ satisfy the canonical commutation relations.

Now, observing eq. (2.1.4.a) and section 1.5, we have that the input-output relations for the light operators $\hat{x}_L(x)$ and $\hat{p}_L(x)$ in the atomic part of the setup in figure 3 are the ones given by the input-output relations (1.5.3.a) and (1.5.3.b), respectively, with the substitution $\hat{x}_a \to \widehat{X}_a$, and also observing eq. (2.1.4.b) and section 1.6.4, we have that the input-output relations of the light operators $\hat{x}'_L(x)$ and $\hat{p}'_L(x)$ in the optomechanical part of the setup in figure 3 are to the ones given by the input-output relations (1.6.4.5.a) and (1.6.4.5.b), respectively, with the substitution $\hat{x}_m \to \widehat{X}_m$:

$$\hat{x}_L^{out} = -\hat{x}_L^{in} \quad , \tag{2.1.5.a}$$

$$\hat{p}_L^{out} = -\hat{p}_L^{in} - \kappa\sqrt{\frac{2}{\tau}}\widehat{X}_a \quad , \tag{2.1.5.b}$$

$$\hat{x}'^{out}_L = -\hat{x}'^{in}_L \quad , \tag{2.1.6.a}$$

$$\hat{p}'^{out}_L = -\hat{p}'^{in}_L - g_{m,c}\sqrt{\frac{2}{\eta_c}}\widehat{X}_m \quad , \tag{2.1.6.b}$$

where $\kappa \equiv -a\sqrt{C_{ph,t}C_{a,t}\tau}$ is the atom-light coupling strength as defined in section 1.4.5, $g_{m,c} \equiv \hbar\sqrt{\frac{1}{m_{eff}\Omega_m}}G\overline{\alpha}_c$ is the optomechanical coupling strength as defined in section 1.6.4. Recall from section 1.4.4 that that κ is dimensionless, and from section 1.6.4 that $g_{m,c}$ has units of inverse of time multiplied by dimensions of $\sqrt{\hbar}$, and since in the present case we have $\hbar = 1$, then $g_{m,c}$ has units of inverse of time. Note that the assumptions that were made in order to arrive at the input-output relations (1.5.3.a), (1.5.3.b), (1.6.4.5.a) and (1.6.4.5.b) are assumed also to hold in the present case.

Let us now consider finding the equations of motion for respectively $\widehat{X}_a$, $\widehat{P}_a$, and $\widehat{X}_m$, $\widehat{P}_m$.

Observing section 1.4.4 we have that the equations of motion for respectively the operators $\widehat{X}_a$ and $\widehat{P}_a$ are found using the Heisenberg equation of motion with the corresponding Hamiltonian $\widehat{H}_{ap} = \widehat{H}_{atoms} + \widehat{H}_I^{eff}$, where $\widehat{H}_I^{eff}$ is given by eq. (1.4.3.6), where the appropriate substitutions involving the different operators are made use of:

$$\frac{d}{dt}\hat{X}_a = \frac{1}{i}\left[\hat{X}_a, \hat{H}_{ap}\right] = +\Omega_{L,n}\hat{P}_a \quad , \tag{2.1.5.c}$$

$$\frac{d}{dt}\hat{P}_a = \frac{1}{i}\left[\hat{P}_a, \hat{H}_{ap}\right] = -\Omega_{L,n}\hat{X}_a + \kappa\sqrt{\frac{2}{\tau}}\hat{x}_L^{in} \quad . \tag{2.1.5.d}$$

Note that eqs. (2.1.5.c) and (2.1.5.d) can also be obtained from eqs. (1.5.3.c) and (1.5.3.d), respectively, with the appropriate substitutions $\hat{x}_a \to \hat{X}_a$ and $\hat{p}_a \to \hat{P}_a$, and using $\Omega_{L,n} \equiv -\Omega_L$.

Observing section 1.6.4 we have that the equations of motion for respectively the operators $\hat{X}_m$ and $\hat{P}_m$ are found using the Lindblad-Heisenberg equation of motion with the corresponding Hamiltonian $\hat{H}_{mc} = \hat{H}_{membrane} + \hat{H}_{l,om}^{lin}$, where $\hat{H}_{l,om}^{lin}$ is given by eq. (1.6.3.5), where the appropriate substitutions involving the different operators are made used of. This is because the membrane resonator is subject to environmental effects as it can decay due thermalization, and it is driven by the quantum fluctuations of the optical cavity mode, i.e. $\hat{x}_c$ and $\hat{p}_c$, which, as seen from section 1.6, depend on environmental effects.

Assume now that the thermalization decay of the membrane resonator can be neglected; this holds true if the whole protocol is performed in the time period $t_1 \approx \tau$ such that $\tau \ll 1/\eta_m\bar{n}_{th}$, where η_m is the membrane resonator mechanical damping rate, and $\bar{n}_{th} \equiv k_B T/\Omega_m$ is the mean occupation of the membrane resonator in thermal equilibrium at temperature T (with $\hbar = 1$). With this assumption the equations of motion for respectively the operators $\hat{X}_m$, $\hat{P}_m$ are thus found using the Heisenberg equation with the Hamiltonian $\hat{H}_{mc}$:

$$\frac{d}{dt}\hat{X}_m = \frac{1}{i}\left[\hat{X}_m, \hat{H}_{mc}\right] = +\Omega_m\hat{P}_m \quad , \tag{2.1.6.c}$$

$$\frac{d}{dt}\hat{P}_m = \frac{1}{i}\left[\hat{P}_m, \hat{H}_{mc}\right] = -\Omega_m\hat{X}_m - g_{m,c}\hat{x}_c = -\Omega_m\hat{X}_m + g_{m,c}\sqrt{\frac{2}{\eta_c}}\hat{x}_L'^{in} \quad . \tag{2.1.6.d}$$

In eqs. (2.1.6.c) and (2.1.6.d) one uses the canonical commutation relation $\left[\hat{X}_m, \hat{P}_m\right] = i$. In the last equality of eq. (2.1.6.d) one uses $\hat{x}_c = -\sqrt{\frac{2}{\eta_c}}\hat{x}_L'^{in}$, which follows as explained below eqs. (1.6.4.4.a-b).

As was done in section 1.5, we now write eqs. (2.1.5.a-d) and (2.1.6.a-d) in the rotating frame, where we use new operators $\hat{X}_j^*$ and $\hat{P}_j^*$ that are related to $\hat{X}_j$ and $\hat{P}_j$ through a 2×2 rotation matrix:

$$\begin{pmatrix}\hat{X}_j^* \\ \hat{P}_j^*\end{pmatrix} = \begin{pmatrix}\cos(\Omega_j t) & \sin(\Omega_j t) \\ -\sin(\Omega_j t) & \cos(\Omega_j t)\end{pmatrix}\begin{pmatrix}\hat{X}_j \\ \hat{P}_j\end{pmatrix} \quad , \tag{2.1.7}$$

where $j = a, m$ and $\Omega_a \equiv \Omega_{L,n}$. Observe in eq. (2.1.7) how in the case of j = a we are looking at counter-clockwise rotations, and in the case of j = m we are looking at clockwise rotations; this is true because $\Omega_{L,n}$ is negative and Ω_m is positive.

Observing eqs. (1.5.5.a-d) and (2.1.7) we have that the propagations eqs. (2.1.5.a-d) and (2.1.6.a-d) are in the rotating frame therefore respectively written as

$$\hat{x}_L^{out} = -\hat{x}_L^{in} \quad , \tag{2.1.8.a}$$

$$\hat{p}_L^{out} = -\hat{p}_L^{in} - \kappa\sqrt{\frac{2}{\tau}}\left(-\hat{P}_a^* \sin\left(\Omega_{L,n}t\right) + \hat{X}_a^* \cos\left(\Omega_{L,n}t\right)\right) \quad , \tag{2.1.8.b}$$

$$\frac{d}{dt}\hat{X}_a^* = \kappa\sqrt{\frac{2}{\tau}}\,\hat{x}_L^{in}\sin(\Omega_{L,n}t) \quad , \tag{2.1.8.c}$$

$$\frac{d}{dt}\hat{P}_a^* = \kappa\sqrt{\frac{2}{\tau}}\,\hat{x}_L^{in}\cos(\Omega_{L,n}t) \quad ; \tag{2.1.8.d}$$

and

$$\hat{x}'^{out}_L = -\hat{x}'^{in}_L \quad , \tag{2.1.9.a}$$

$$\hat{p}'^{out}_L = -\hat{p}'^{in}_L - g_{m,c}\sqrt{\frac{2}{\eta_c}}\left(-\hat{P}_m^* \sin(\Omega_m t) + \hat{X}_m^* \cos(\Omega_m t)\right) \quad , \tag{2.1.9.b}$$

$$\frac{d}{dt}\hat{X}_m^* = g_{m,c}\sqrt{\frac{2}{\eta_c}}\,\hat{x}'^{in}_L\sin(\Omega_m t) \quad , \tag{2.1.9.c}$$

$$\frac{d}{dt}\hat{P}_m^* = g_{m,c}\sqrt{\frac{2}{\eta_c}}\,\hat{x}'^{in}_L\cos(\Omega_m t) \quad . \tag{2.1.9.d}$$

Assume now that the light after the atomic ensemble provides the input light to the cavity such that

$$\hat{x}'^{in}_L = -\hat{x}_L^{out} \quad , \tag{2.1.10.a}$$

$$\hat{p}'^{in}_L = -\hat{p}_L^{out} \quad . \tag{2.1.10.b}$$

In order to achieve the equalities given by eqs. (2.1.10.a-b), light interfaces the atomic ensemble and the membrane resonator through a filter seen in figure 3. In the text of figure 3 it is explained what the filter does. Note that in chapter 4, where the atom-membrane entanglement experiment, which is an attempt at a real life realization of the entanglement protocol presented in this chapter, is described, it is explained how we experimentally realize the filter.

Assume now further that the atomic and the membrane resonator parameters are matched by requiring

$$\kappa\sqrt{\frac{2}{\tau}} = g_{m,c}\sqrt{\frac{2}{\eta_c}} \quad , \tag{2.1.11.a}$$

and that the angular frequencies Ω_m and $\Omega_{L,n}$ satisfy

$$\Omega_m = -\Omega_{L,n} \quad . \tag{2.1.11.b}$$

Using the assumptions given by eqs. (2.1.10.a-b) and (2.1.11.a-b) we have that the propagations eqs. (2.1.8.a-d) and (2.1.9.a-d) tell us that

$$\hat{x}'^{out}_L = -\hat{x}_L^{in} \quad , \tag{2.1.12.a}$$

$$\hat{p}'^{out}_L = -\hat{p}_L^{in} - \kappa\sqrt{\frac{2}{\tau}}\left(\left(\hat{P}_m^* - \hat{P}_a^*\right)\sin\left(\Omega_{L,n}t\right) + \left(\hat{X}_m^* + \hat{X}_a^*\right)\cos\left(\Omega_{L,n}t\right)\right) \quad , \tag{2.1.12.b}$$

$$\frac{d}{dt}\left(\hat{X}_a^* + \hat{X}_m^*\right) = 0 \quad , \tag{2.1.12.c}$$

$$\frac{d}{dt}\left(\hat{P}_a^* - \hat{P}_m^*\right) = 0 \quad , \tag{2.1.12.d}$$

where in eq. (2.1.12.b) one has that $\sin(\Omega_m t) = \sin\left(-\Omega_{L,n} t\right) = -\sin\left(\Omega_{L,n} t\right)$ and $\cos(\Omega_m t) = \cos\left(-\Omega_{L,n} t\right) = \cos\left(\Omega_{L,n} t\right)$; in eqs. (2.1.12.c-d) one has that $\hat{x}_L^{in} = \hat{x}'^{in}_L$, which follows from eq. (2.1.10.a) in combination with eq. (2.1.8.a), and that $\sin(\Omega_m t) = -\sin\left(\Omega_{L,n} t\right)$ and $\cos(\Omega_m t) = \cos\left(\Omega_{L,n} t\right)$.

Note that from eq. (2.1.7) it is clear that once we'll know $\hat{X}_m^* + \hat{X}_a^*$ and $\hat{P}_m^* - \hat{P}_a^*$, then we'll know $\hat{X}_m + \hat{X}_a$ and $\hat{P}_m - \hat{P}_a$, and vice versa. Observe that according to eq. (2.1.7) we have, when using eq. (2.1.11.b) and the properties $\sin\left(-\Omega_{L,n} t\right) = -\sin\left(\Omega_{L,n} t\right)$ and $\cos\left(-\Omega_{L,n} t\right) = \cos\left(\Omega_{L,n} t\right)$, that $\hat{X}_m^* + \hat{X}_a^*$ and $\hat{P}_m^* - \hat{P}_a^*$ and related to $\hat{X}_m + \hat{X}_a$ and $\hat{P}_m - \hat{P}_a$ through a a 2×2 rotation matrix:

$$\begin{pmatrix} \hat{X}_m^* + \hat{X}_a^* \\ \hat{P}_m^* - \hat{P}_a^* \end{pmatrix} = \begin{pmatrix} \cos\left(\Omega_{L,n} t\right) & \sin\left(\Omega_{L,n} t\right) \\ -\sin\left(\Omega_{L,n} t\right) & \cos\left(\Omega_{L,n} t\right) \end{pmatrix} \begin{pmatrix} \hat{X}_m + \hat{X}_a \\ \hat{P}_m - \hat{P}_a \end{pmatrix} \quad . \tag{2.1.13}$$

Now, the result of eq. (2.1.12.b) tells us that when an externally applied static magnetic field subjects the atoms and it is homogeneously pointing along the same direction, being the z-direction, and $\hat{p}'^{out}_L$ is measured, we will simultaneously access information about the commuting EPR observables $\hat{X}_m^* + \hat{X}_a^*$ and $\hat{P}_m^* - \hat{P}_a^*$. According to eqs. (2.1.12.c) and (2.1.12.d) such measurement of $\hat{p}'^{out}_L$ will result in a QND measurement of $\hat{X}_m^* + \hat{X}_a^*$ and $\hat{P}_m^* - \hat{P}_a^*$, because $\hat{X}_m^* + \hat{X}_a^*$ and $\hat{P}_m^* - \hat{P}_a^*$ are not affected by light back-action during the interaction thus ensuring that the states of $\hat{X}_m^* + \hat{X}_a^*$ and $\hat{P}_m^* - \hat{P}_a^*$ are not demolished. Note that this is exactly the opposite of the case of eqs. (1.5.5.a-d) (and also eqs. (2.1.8.a-d) and (2.1.9.a-d)).

$\hat{X}_m^* + \hat{X}_a^*$ and $\hat{P}_m^* - \hat{P}_a^*$ can from eq. (2.1.12.b) be *gained access to* by multiplying $\hat{p}'^{out}_L$ by respectively $\sin\left(\Omega_{L,n} t\right)$ and $\cos\left(\Omega_{L,n} t\right)$ and integrating in time from 0 to τ. We consider now therefore the two operators

$$\hat{p}'^{out}_{L,cos} \equiv -\sqrt{\frac{2}{\tau}} \int_0^\tau dt \cos\left(\Omega_{L,n} t\right) \, \hat{p}'^{out}_L \quad , \tag{2.1.14.a}$$

$$\hat{p}'^{out}_{L,sin} \equiv -\sqrt{\frac{2}{\tau}} \int_0^\tau dt \sin\left(\Omega_{L,n} t\right) \, \hat{p}'^{out}_L \quad . \tag{2.1.14.b}$$

Performing the Fourier transform of $\hat{p}'^{out}_L$ in eq. (2.1.12.b) and observing eqs. (2.1.12.c-d) therefore yields

$$\hat{p}'^{out}_{L,cos} = \hat{p}^{in}_{L,cos} + \kappa\left(\hat{X}_m^* + \hat{X}_a^*\right) \quad , \tag{2.1.15.a}$$

$$\hat{p}'^{out}_{L,sin} = \hat{p}^{in}_{L,sin} + \kappa\left(\hat{P}_m^* - \hat{P}_a^*\right) \quad , \tag{2.1.15.b}$$

where

$$\hat{p}^{in}_{L,cos} \equiv -\sqrt{\frac{2}{\tau}}\int_0^\tau dt\, cos\left(\Omega_{L,n}t\right)\ \hat{p}^{in}_{L} \quad , \tag{2.1.16.a}$$

$$\hat{p}^{in}_{L,sin} \equiv -\sqrt{\frac{2}{\tau}}\int_0^\tau dt\, sin\left(\Omega_{L,n}t\right)\ \hat{p}^{in}_{L} \quad . \tag{2.1.16.b}$$

Note that in order to arrive at eqs. (2.1.15.a-b) it was assumed that $\int_0^\tau dt\, cos^2\left(\Omega_{L,n}t\right) \approx \int_0^\tau dt\, sin^2\left(\Omega_{L,n}t\right) \approx \tau/2$, and that $\int_0^\tau dt\, sin\left(\Omega_{L,n}t\right) cos\left(\Omega_{L,n}t\right) \approx 0$, which is justified if the time period of the protocol, $t_1 \approx \tau$, is much longer than $1/\Omega_L$, i.e. $\tau \gg 1/\Omega_L$.

Using eqs. (1.3.10), (1.3.11), (2.1.3) and (2.1.13), and the definitions of $\hat{P}_a$, $\hat{P}_m$, $\hat{X}_a$, $\hat{X}_m$ below eqs. (2.1.4.a-b) we now calculate the sum of the variances of $\hat{p}'^{out}_{L,cos}$ and $\hat{p}'^{out}_{L,sin}$:

$$\begin{aligned} Var\left(\hat{p}'^{out}_{L,cos}\right) + Var\left(\hat{p}'^{out}_{L,sin}\right) &= Var\left(\hat{p}^{in}_{L,cos}\right) + Var\left(\hat{p}^{in}_{L,cos}\right) + Var\left(\kappa\left(\hat{X}^*_m + \hat{X}^*_a\right)\right) + Var\left(\kappa\left(\hat{P}^*_m - \hat{P}^*_a\right)\right) \\ &= 1 + \kappa^2 \sum_{EPR} \quad , \end{aligned} \tag{2.1.17}$$

where the property $Var\left(b_1\hat{C}\right) = b_1^2 Var\left(\hat{C}\right)$ is used, where b_1 is a constant and $\hat{C}$ is an operator.

The first term on the RHS of eq. (2.1.17) is attributed to the shot-noise of the light; this term arises, because in the present case it is assumed that we are dealing with the light operator $\hat{p}^{in}_L$ that is in the coherent state of light such that eqs. (1.3.10) and (1.3.11) hold. Note that according to section 1.4 and eqs. (1.3.10), (1.3.11) and (1.4.5.2.a), the magnitude of the shot-noise is $\left|Var\left(\hat{S}_y(t)\right)\right| = \left|Var\left(\hat{S}_z(t)\right)\right| = \left|\frac{S_x(t)}{2}\right| \approx \frac{C_{ph,t}}{4}$, where it is seen to scale with the number of linearly-polarized photons.

The second term on the RHS of eq. (2.1.17) is the atom-light coupling strength $\kappa \equiv -a\sqrt{C_{ph,t}C_{a,t}\tau}$, as defined in section 1.4.5, squared and multiplied by the EPR variance $\sum_{EPR} \equiv Var\left(\frac{\hat{x}_m+\hat{x}_a}{\sqrt{2}}\right) + Var\left(\frac{\hat{p}_m-\hat{p}_a}{\sqrt{2}}\right)$, as defined in eq. (2.1.3).

We see now from eq. (2.1.17) that by measuring $\hat{p}'^{out}_{L,cos}$ and $\hat{p}'^{out}_{L,sin}$, we can, with the knowledge of the atom-light coupling strength κ, extract the EPR variance $\sum_{EPR}$, and thereby find out whether EPR variance criterion (2.1.3) is fulfilled.

Using the property $Var\left(b_1\hat{C} \pm b_2\hat{Z}\right) = b_1^2 Var\left(\hat{C}\right) + b_2^2 Var\left(\hat{Z}\right) \pm 2b_1b_2 Cov\left(\hat{C},\hat{Z}\right)$, where b_1 and b_2 are constants, $\hat{C}$ and $\hat{Z}$ are operators, and $Cov\left(\hat{C},Z\right)$ is the covariance between $\hat{C}$ and $\hat{Z}$, we have that $\sum_{EPR}$ in eq. (2.1.3) in general reads as

$$\sum_{EPR} \equiv \frac{1}{2}\left(Var(\hat{x}_m) + Var(\hat{x}_a) + Var(\hat{p}_m) + Var(\hat{p}_a)\right) + Cov(\hat{x}_m,\hat{x}_a) - Cov(\hat{p}_m,\hat{p}_a) \ . \tag{2.1.18}$$

Assuming that initially, at $t = t_0$, i.e. before the light interfaces the atomic ensemble and the membrane resonator, the two systems are in their ground states, we have that the covariances in eq. (2.1.18) disappear, i.e. $Cov\left(\hat{x}_m(t_0),\hat{x}_a(t_0)\right) = 0$ and $Cov\left(\hat{p}_m(t_0),\hat{p}_a(t_0)\right) = 0$, and $\sum_{EPR} = 1$,

which according to eq. (2.1.3) tells us that the atoms and the membrane resonator are not entangled, but nevertheless is the best we can do for the two quantum-uncorrelated systems. Note that as the two systems are in their ground states at t_0, we have, according to eqs. (1.2.12) and (1.4.5.1.a-b), and section 1.2, that the terms $\mathrm{Var}(\hat{x}_a) = \frac{1}{2}$ and $\mathrm{Var}(\hat{p}_a) = \frac{1}{2}$, and that they are attributed to the projection-noise of the atoms, and, according to eq. (1.6.2.1), that the terms $\mathrm{Var}(\hat{x}_m) = \frac{1}{2}$ and $\mathrm{Var}(\hat{p}_m) = \frac{1}{2}$, and that they are attributed to the vacuum noise of the membrane resonator. Now, after these two systems become interfaced by the light *and* we have performed the measurement of $\hat{p}'^{out}_{L,cos}$ and $\hat{p}'^{out}_{L,sin}$, the covariances in eq. (2.1.18) no longer disappear, i.e. $\mathrm{Cov}\big(\hat{x}_m(t_1), \hat{x}_a(t_1)\big) \neq 0$ and $\mathrm{Cov}\big(\hat{p}_m(t_1), \hat{p}_a(t_1)\big) \neq 0$, where $t_1 \approx \tau$ is the time period of the protocol, i.e. the time elapsed from t_0 till the measurement is performed, and, as shown in [12] $\sum_{EPR}$ becomes *reduced*, i.e.

$$\sum_{EPR} = \frac{1}{\frac{2}{1+\bar{n}_{th,i}} + 4\kappa^2} < 1 \quad , \tag{2.1.19}$$

which according to eq. (2.1.3) tells us that the atomic ensemble and the membrane resonator become entangled. Here $\bar{n}_{th,i}$ is the initial thermal occupation of the membrane resonator.

Note how due to the factor $\frac{2}{1+\bar{n}_{th,i}}$ in the denominator in eq. (2.1.19), the present protocol allows entanglement to be observable even if the membrane resonator initially is well above its ground state; this is true, because $\frac{2}{1+\bar{n}_{th,i}} \in [2; 0)$.

Note as well how eq. (2.1.19) tells us that the more atoms there are in the coherent spin state $|F = 4, m_F = 4>$ and the more linearly-polarized photons there are to interact with these atoms, the lower $\sum_{EPR}$ goes below one; this is true, because $\kappa^2 = a^2 C_{ph,t} C_{a,t} \tau$. In [12] it is noted that moderate values of κ^2 are $\kappa^2 \lesssim 0.25$. In chapter 3, where the main experimental components of our group's atom-membrane interfacing experimental setup are described, an expression for κ^2 will be put forward that will prove to be convenient from the point of view of our atom-membrane experiment. By making use of experimental data and parameters that characterize our experiment it will then be estimated what values for κ^2 we can expect to obtain in the case of our atom-membrane interfacing experimental setup.

2.2 The dominant impairing effects in atom-membrane entanglement generation

In this section I will discuss the dominant impairing effects that alter the expression for the reduced EPR variance $\sum_{EPR}$ given by eq. (2.1.19). By examining the dominant impairing effects the entanglement protocol will reveal practical considerations common to experimental systems that in principle can be used for satisfying the entanglement protocol.

The first dominant impairing effect is due to the mismatch between the atomic and the membrane resonator parameters, i.e. when $\kappa\sqrt{\frac{2}{\tau}} \neq g_{m,c}\sqrt{\frac{2}{\eta_c}}$. Observing eqs. (2.1.8.c-d) and (2.1.9.c-d) for

respectively $\frac{d}{dt}\hat{X}_a^*$, $\frac{d}{dt}\hat{P}_a^*$ and $\frac{d}{dt}\hat{X}_m^*$, $\frac{d}{dt}\hat{P}_m^*$, and also section 1.5, we see that if the atomic and the membrane resonator parameters are mismatched, then light back-action noise will enter the expression for $\hat{p}'^{out}_L$, and thus the expressions for $\hat{p}'^{out}_{L,cos}$ and $\hat{p}'^{out}_{L,sin}$. This will then alter the expression for $\mathrm{Var}(\hat{p}'^{out}_{L,cos}) + \mathrm{Var}(\hat{p}'^{out}_{L,sin})$, and the term describing the light back-action noise will be absorbed by the expression for the EPR variance $\sum_{EPR}$. Note that all impairing effects essentially are absorbed by $\sum_{EPR.}$ According to [12], the EPR variance $\sum_{EPR}$ given by eq. (2.1.19) will due to the atomic and the membrane resonator parameter mismatch become $\sum_{EPR} \rightarrow \sum_{EPR} + \left[\epsilon\kappa\left(\bar{n}_{th,i} + 2\right)\right]^2$, where $\epsilon \equiv \frac{(\kappa - \delta\sqrt{\eta_c\tau})}{(\kappa + \delta\sqrt{\eta_c\tau})}$ denotes the practical mismatch between the atomic and the membrane resonator parameters, where δ is used to describe the degree of this mismatch. Note that $\left[\epsilon\kappa\left(\bar{n}_{th,i} + 2\right)\right]^2$ is the leading-order term. Due to this modification of the reduced EPR variance $\sum_{EPR}$, there is a practical limit set to the initial thermal occupation of the membrane resonator. In [12] it is noted that for $\kappa^2 \gtrsim 1$ a mismatch of $\epsilon \sim \frac{1}{10\bar{n}_{th,i}}$ becomes tolerable. Note that in eqs. (4.2.1.a-b) one can see the versions of $\hat{p}'^{out}_{L,cos}$ and $\hat{p}'^{out}_{L,sin}$, when the atomic and the membrane resonator parameters are mismatched.

The second dominant impairing effect is due to the thermalization decay of the membrane resonator. Recall that this effect is neglected in the derivation of eqs. (2.1.6.c) and (2.1.6.d) for respectively $\frac{d}{dt}\hat{X}_m$ and $\frac{d}{dt}\hat{P}_m$. If this effect is not neglected, then there will be additional terms entering eqs. (2.1.6.c-d) that will be proportional to the membrane resonator mechanical damping rate η_m, and these decay terms will also be accompanied by Langevin operators such that the correct quantum statistics could be preserved. According to [12], the EPR variance $\sum_{EPR}$ given by eq. (2.1.19) will due to the thermalization decay become $\sum_{EPR} \rightarrow \sum_{EPR} + \eta_m\tau(\bar{n}_{th} + 1)$. Due to this modification of the reduced EPR variance $\sum_{EPR}$, there is a practical limit to how long the time period $t_1 \approx \tau$ of the protocol can be. We see that the practical requirement for $t_1 \approx \tau$ becomes $\tau \ll 1/\eta_m\bar{n}_{th}$. The size of η_m is set by the quality factor [3] Q_m of the membrane resonator, since $Q_m \equiv \Omega_m/\eta_m$ [17], where Ω_m is the angular frequency of the mechanical mode of the membrane resonator as seen in eq. (2.1.4.b).

The third dominant impairing effect is due to the loss of light via detection inefficiency and spontaneous emission in the atom-light interaction. Note that the spontaneous emission can indeed be treated as a light loss mechanism, because spontaneously emitted photons travel in a random direction [24]. According to [12], the EPR variance $\sum_{EPR}$ given by eq. (2.1.19) will due to the loss of light become $\sum_{EPR} \rightarrow (1 - \varepsilon)\sum_{EPR} + \varepsilon$, where ε denotes the fraction of the photons lost. Due to this modification of the reduced EPR variance $\sum_{EPR}$, the entanglement created by this protocol is reduced but not removed.

[3] A quality factor, or Q-factor for short, is a dimensionless parameter that describes how underdamped a resonator is.

Chapter 3: Experimental system

In this chapter I first describe the main experimental components of the atom-membrane entanglement interfacing experimental setup described in chapter 4. These experimental components include: a laser system, a microcell that contains the Cesium-133 atoms, a magnetic shield for shielding the atoms against stray magnetic fields, a system that can generate useful magnetic fields that subject the atoms, and a cavity optomechanical system that contains the nanomechanical membrane resonator.

The material presented in this chapter is used to then put forward an expression for κ^2 that will prove to be convenient from the point of view of our atom-membrane entanglement experiment. By making use of experimental data and parameters that characterize our experiment it will then be estimated what values for κ^2 we can expect to obtain in the case of our atom-membrane interfacing experimental setup.

Note that in this chapter we will be making use of the *regular* atomic ensemble total angular momentum operators and the *regular* Stokes operators, i.e. the operators $\hat{J}_x(t) \propto \hat{x}_a$, $\hat{J}_y(t) \propto \hat{p}_a$, $\hat{J}_z(t)$, $\hat{S}_x(t)$, $\hat{S}_y(t) \propto \hat{p}_L(z)$, $\hat{S}_z(t) \propto \hat{x}_L(z)$, where $\hat{x}_a$ and $\hat{p}_a$, and $\hat{x}_L(z)$ and $\hat{p}_L(z)$ are respectively the *scaled* atomic ensemble total angular momentum operators and the *scaled* Stokes operators. All these operators are introduced in section 1.4.

3.1 The laser system

The laser system used in the experiments is composed of three lasers: the probe laser, the pump laser and the repump laser, where the latter two constitute an optical pumping system. See figure 4 to see the relevant energy levels of Cesium-133 atoms that are addressed by these lasers. In the following I will explain the experimental roles of the lasers and what we do in order to lock the frequency of the respective lasers.

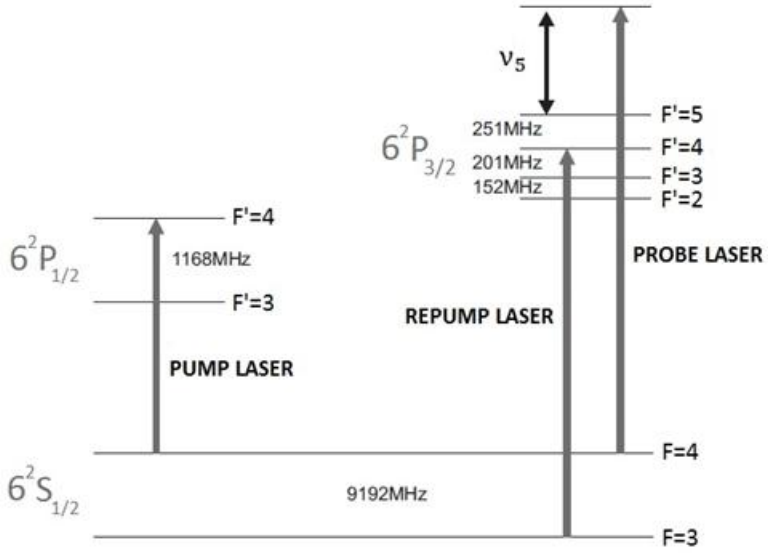

Figure 4. The relevant energy levels of Cesium-133 atoms addressed by the laser system used in the experiments. The laser system is composed of three lasers: the probe laser, the pump laser and the repump laser. The probe laser is tuned off-resonantly to the D_2 line transition $6^2S_{1/2}, F = 4 \rightarrow 6^2P_{3/2}, F` = 5$ with negative frequency detuning $\nu_5$; the pump laser is tuned to the $D_1$ line transition $6^2S_{1/2}, F = 4 \rightarrow 6^2P_{1/2}, F` = 4$; and the repump laser is tuned to the D_2 line transition $6^2S_{1/2}, F = 3 \rightarrow 6^2P_{3/2}, F` = 4$. The figure is adapted from [1].

3.1.1 The probe laser

The probe laser is used to probe the Cesium-133 atoms. As indicated by figure 4 the probe laser is tuned off-resonantly to the D_2 line transition $6^2S_{1/2}, F = 4 \rightarrow 6^2P_{3/2}, F` = 5$ with negative frequency detuning $\nu_5 \equiv \frac{\Delta_5}{2\pi}$; and the light emitted by the probe laser is linearly-polarized. Using this information we are able to summarize the probe laser's interaction with the Cesium-133 atoms by the propagation eqs. (1.4.4.7.a-d), given that no external magnetic fields are present, and by propagation eqs. (1.5.3.a-d), given that an external static magnetic field is present.

In the experiments a Toptica DLpro diode laser is used as the probe laser; it is tuned off-resonantly to the D_2 line transition $6^2S_{1/2}, F = 4 \rightarrow 6^2P_{3/2}, F` = 5$ with negative frequency detuning $\nu_5 = -1600$ MHz . According to the online source [41] that sells Toptica DLpro diode lasers, the Toptica DLpro diode laser produces linearly-polarized light to a high degree (linear > 100:1). Before subjecting the atoms to the light we *clean* the linear-polarization even further by making use polarizing beam splitters, thus making sure that we probe the atoms with linearly-polarized light.

3.1.2 The pump and repump lasers

The pump and repump lasers constitute an optical pumping system, whose role is to put as many of the Cesium-133 atoms into the coherent spin state $|F = 4, m_F = 4>$ of the energy level $6^2S_{1/2}, F = 4, m_F = 4$, as possible. As indicated by figure 4 the pump laser is tuned to the D_1 line transition $6^2S_{1/2}, F = 4 \rightarrow 6^2P_{1/2}, F` = 4$, and the repump laser is tuned to the D_2 line transition $6^2S_{1/2}, F =$

$3 \rightarrow 6^2P_{3/2}, F` = 4$. In the experiments, the light emitted by the pump and the repump lasers is right-circulary (σ_+) polarized and travelling along the direction of a static magnetic field that we produce as explained in section 3.3.

In order to see how our optical pumping system works we may use Fermi's golden rule with the Hamiltonian for the dipole interaction and derive the following selection rules for the dipole interaction driven transitions [25]:

$$\Delta L = \pm 1 \quad (3.1.2.1.a)$$
$$\Delta S = 0 \quad (3.1.2.1.b)$$
$$\Delta J = 0, \pm 1 \quad (3.1.2.1.c)$$
$$\Delta F = 0, \pm 1 \quad (3.1.2.1.d)$$

$$\Delta m_F = 0 \quad (\pi \text{ transitions}) \quad (3.1.2.2.a)$$
$$\Delta m_F = +1 \quad (\sigma_+ \text{ transitions}) \quad (3.1.2.2.b)$$
$$\Delta m_F = -1 \quad (\sigma_- \text{ transitions}) \quad (3.1.2.2.c)$$

where the quantum numbers L, S, J, F are the quantum numbers defined in section 1.1, but now the capital letters are used, because we are dealing with ensembles of Cesium-133 atoms. Note that the Cesium-133 atoms can also decay by spontaneous emission with the selection rule

$$\Delta m_F = 0, +1 \text{ (spontaneous emission)} \quad (3.1.2.3)$$

Observing the selection rules for the dipole interaction driven transitions, given by eqs. (3.1.2.1.a-d) and (3.1.2.2.a-c) and the selection rule for spontaneous emission decay, given by eq. (3.1.2.3), we have that the pump laser light can bring the atoms from the energy levels $6^2S_{1/2}, F = 4, m_F = -4, \dots, 3$ to the energy level $6^2S_{1/2}, F = 4, m_F = 4$ with the help of spontaneous emission decay, and if there are atoms in the energy level $6^2S_{1/2}, F = 3, m_F = -3, \dots, 3$, then they will be put to the energy level $6^2S_{1/2}, F = 4, m_F = 4$ by the repump laser light with the help of spontaneous emission decay. By increasing the pump and repump laser output power and by making sure that both the pump and the repump laser light is right-circularly-polarized, the value of m_F can be made to increase on average during the optical pumping process such that all of the Cesium-133 atoms are put into their coherent spin state $|4,4>$ of the energy level $6^2S_{1/2}, F = 4, m_F = 4$. In figure 5 we can see an illustration showing an example how the optical pumping system will put a Cesium-133 atom into the energy level $6^2S_{1/2}, f = 4, m_f = 4$, if it starts in the energy level $6^2S_{1/2}, f = 4, m_f = 2$.

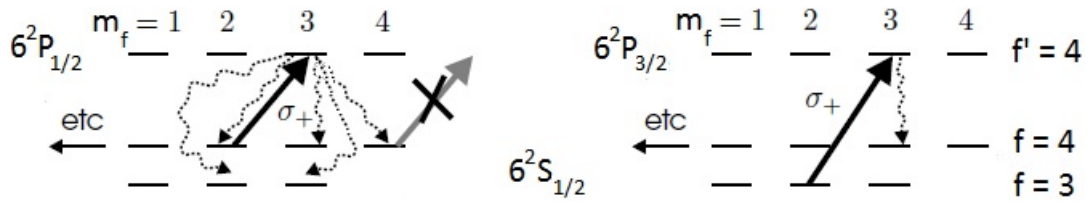

Figure 5. An illustration showing how the optical pumping system will put a Cesium-133 atom into the energy level $6^2S_{1/2}, f = 4, m_f = 4$ with the help of spontaneous emission decay, if the atom starts in the energy level $6^2S_{1/2}, f = 4, m_f = 2$. The pump laser

action is shown on the left of the figure and the repump laser action is shown on the right of the figure; both lasers are assumed to produce right-circulary (σ_+) polarized light. Starting with the left figure, a Cesium-133 atom starts in the energy level $6^2S_{1/2}, f = 4, m_f = 2$, from which it is lifted to the energy level $6^2P_{1/2}, f = 4, m_f = 3$ by the pump laser light; from $6^2P_{1/2}, f = 4, m_F = 3$ the atom can spontaneously decay into the energy level $6^2S_{1/2}, f = 3$ with $m_f = 2, 3$ or $6^2S_{1/2}, f = 4$ with $m_f = 2, 3, 4$. If the atom will only spontaneously decay into the energy level $6^2S_{1/2}, f = 4$, it will eventually end up in the coherent spin state $|4,4>$ of the energy level $6^2S_{1/2}, f = 4, m_f = 4$, which is a dark state from which the atom will not move further; if, however, the atom does spontaneously decay into the energy level $6^2S_{1/2}, f = 3$, this will be counteracted by the repump laser light shown on the right of the figure. This pumping scheme will work due to fact that the light emitted by the pump and the repump lasers travels along the direction of a static magnetic field, and due to the selection rules given by eqs. (3.1.2.1.a-d), (3.1.2.2.a-c) and (3.1.2.3). The figure is adapted from [1].

In the experiments two separate Toptica DL100 diode lasers are used as the pump and repump lasers. According to the online source [42] that sells Toptica DL100 diode lasers, the Toptica DL100 diode laser produces linearly-polarized light to a high degree (linear > 100:1). Before subjecting the atoms to the light we *clean* the linear-polarization even further by making use polarizing beam splitters, similarly to the case of the probe laser light. In order to turn the linearly-polarized light into right-circulary polarized light in the experiments, we put, in succession, a quarter-wave plate (QWP), and a half-wave plate (HWP) in the path of the respective light beams. For e.g. linear horizontally-polarized light entering the QWP, we have according to the Jones matrix calculus introduced in appendix D, that the QWP must be $\frac{\pi}{4}$-rotated, and the HWP after the QWP must be $\frac{\pi}{8}$-rotated, such that the linear horizontally-polarized light can be turned to right-circularly-polarized light.

3.1.3 Locking the frequencies of the lasers

In this subsection I will explain what we do in order to lock the frequencies of our lasers.

Atomic motion causes Doppler broadening of hyperfine atomic transitions. Because atomic velocities are distributed according to the Maxwell-Boltzmann distribution [26], this broadening has a Gaussian profile. The full-width-at-half-maximum (FWHM) of this Gaussian profile is given by

$$\delta\nu_{D,FWHM,atom} = \sqrt{\frac{8k_B T \ln(2)}{m_{atom}c^2}}\nu_{rest} \quad , \tag{3.1.3.1}$$

where k_B is the Boltzmann constant, T is the temperature, and ν_{rest} is the frequency of the hyperfine transition, when an atom of mass m_{atom} is at rest with respect to the lab frame, hence referred to as the *rest* frequency of the hyperfine transition.

In a case of the repump laser, we have in eq. (3.1.3.1) that $\nu_{rest} = \nu_{D2}$, where ν_{D2} is the frequency of the D_2 line transition, and also $m_{atom} = m_{Cs}$, where m_{Cs} is the mass of a Cesium atom, and $T \sim 293$ K is the room temperature, such that

$$\delta\nu_{D,FWHM,Cs;D2} \approx 274 \text{ MHz} \quad . \tag{3.1.3.2.a}$$

Note that there are also other line width broadening effects involved such as, e.g., the power broadening effect. However, the Doppler broadening effect is here the most significant one, such that for simplicity we will be neglecting other line width broadening effects.

For comparison, recall below eq. (1.4.3.6) that the natural FWHM line width of the D_2 line transition is (in units of inverse of time)

$$\delta\nu_{n,FWHM,Cs;D2} = 5.22\ \text{MHz} \quad . \tag{3.1.3.2.b}$$

Observing figure 4 and eqs. (3.1.3.2.a) and (3.1.3.2.b) we see that the repump laser will take the Cesium-133 atoms from the hyperfine structure level $6^2S_{1/2}$, F = 3 to any of the other three hyperfine structure levels $6^2P_{3/2}$, F' = 2, 3, 5 with a significantly increased probability due to the Doppler broadening effect.

In order to lock the frequencies of our lasers at the desired points we make use of an experimental technique known as frequency modulated (FM) saturated absorption spectroscopy. We employ this technique for each of our lasers by building setups, whose diagrammatic representations can be seen in figure 6.

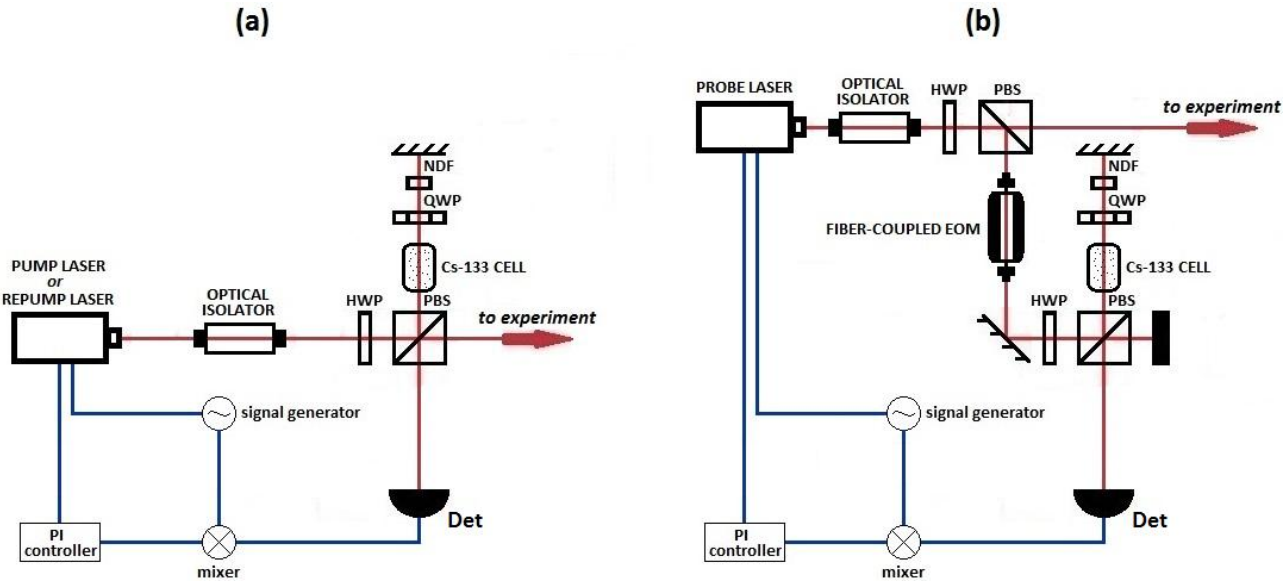

Figure 6. (a) and (b) Diagrammatic representations of setups that employ frequency modulated (FM) saturated absorption spectroscopy, which is an experimental technique that allows us to lock the frequencies of our lasers at the desired points. (a) depicts the cases of the pump and the repump lasers; and (b) depicts the case of the probe laser. In the figures we have that the solid red lines are optical paths, the solid blue lines are electrical-signal paths, PBS stands for polarizing beam splitter, HWP stands for half-wave plate, QWP stands for quarter-wave plate, NDF stands for neutral-density filter, Cs-133 cell is a Cesium-133 vapor cell, Det is a photodetector, and PI controller is a proportional-integral controller.

In figure 6 we see that the light originating from a given laser travels through an optical isolator and then a part of this light is reflected by a polarizing beam splitter (PBS), where it used for FM saturated absorption spectroscopy. Note that the function of the optical isolator is to prevent potential back-reflections from entering the laser.

Figure 6 (a) depicts the cases of the pump and the repump lasers. Here we see that the reflected light travels in succession through the Cesium-133 vapor cell, the quarter-wave plate (QWP), and the neutral-density filter (NDF), then becomes reflected back on a mirror, and then travels in succession through the NDF, the QWP, and the cell again, and, finally, gets transmitted by the PBS and picked up by the photodetector Det. The function of the QWP is to make sure that when the light passes the cell for the second time, all of this light becomes transmitted by the PBS and nothing gets reflected; in order to see why this is true, one can make use of Jones calculus introduced in appendix D. Also, the function of the NDF is to attenuate the light beam.

Figure 6 (b) depicts the case of the probe laser. Here we see that the reflected light first travels through a fiber-coupled electro-optic modulator (EOM) before it propagates the same way as in the case of the pump and the repump lasers seen in figure 6 (a). The function of the fiber-coupled EOM is to create frequency sidebands that allow us to lock the frequency of the probe laser at the large negative frequency detuning $\nu_5 = -1600$ MHz mentioned in subsection 3.1.1.

Now, from the absorption signal originating from the photodetector, we will see small but distinct peaks revealing the rest frequencies of the hyperfine transitions, and these peaks will have FWHM line widths close to the natural FWHM line widths of the corresponding hyperfine transitions. These peaks result from the motionless atoms and the atoms moving perpendicular to the beam path, both of which resonate with the counter-propagating light beams, i.e. the strong light beam and the attenuated light beam. These peaks are produced because the strong light beam will saturate the transition such that the attenuated beam will induce stimulated emission, and so, a small peak in the Doppler broadened profile will appear, thus revealing the rest frequency of the hyperfine transition.

Note that between the peaks that reveal the rest frequency of the given hyperfine transition, there will be *cross-over* peaks. These cross-over peaks result from the moving atoms that resonate with the counter-propagating light beams.

We wish the frequency of the given laser to be locked at the center of a designated peak. Locking the frequency will require a feedback-mechanism to the laser electronics, because the frequency of the laser might naturally drift. The absorption signal is, however, not used for the locking. Instead, the derivative of the absorption signal, known as *the error signal*, is used for the locking.

In order to obtain the error signal, a sine modulation signal $\sin(\omega_{\mathrm{mod}}t + \varphi_{\mathrm{mod},1})$ of angular frequency ω_{mod} and phase $\varphi_{\mathrm{mod},1}$ is created by a signal generator and fed to the laser electronics. With this modulation signal, the laser will generate $\pm\omega_{\mathrm{mod}}$-sidebands. If we were to detect this frequency modulated light after its interaction with the Cesium-133 vapor cell with a photodetector, the photocurrent resulting from that photodetector would contain a component oscillating as $\sin(\omega_{\mathrm{mod}}t)$ and another component oscillating as $\cos(\omega_{\mathrm{mod}}t)$. The component oscillating as $\sin(\omega_{\mathrm{mod}}t)$ is proportional to the difference in absorption of the two sidebands; and the component oscillating as $\cos(\omega_{\mathrm{mod}}t)$ is proportional to the difference between the phase shift of the carrier and the (average) phase shift between the two sidebands. In our situation $\omega_{\mathrm{mod}} \approx 4$ MHz, which is small compared to the hyperfine structure energy splitting, and so, the component oscillating as

$\sin(\omega_{mod}t)$ is the derivative of the absorption signal, i.e. it is the error signal. Now, in order to pick out the error signal, the photocurrent resulting from the photodetector Det in figure 6 is via a mixer combined with the sine demodulation signal $\sin(\omega_{mod}t + \varphi_{mod,2})$ of angular frequency ω_{mod} and phase $\varphi_{mod,2}$ created by a signal generator. By adjusting the phase difference $\varphi_{mod,1} - \varphi_{mod,2}$, one is able to pick out the error signal. This error signal is then fed to a proportional-integral (PI) controller. The signal generated by the PI controller then travels to the laser electronics, and this completes the frequency locking feedback-mechanism.

In figure 7 we can see the absorption signal and the error signal for the probe laser light, when the fiber-coupled EOM is turned off such that sidebands are not produced.

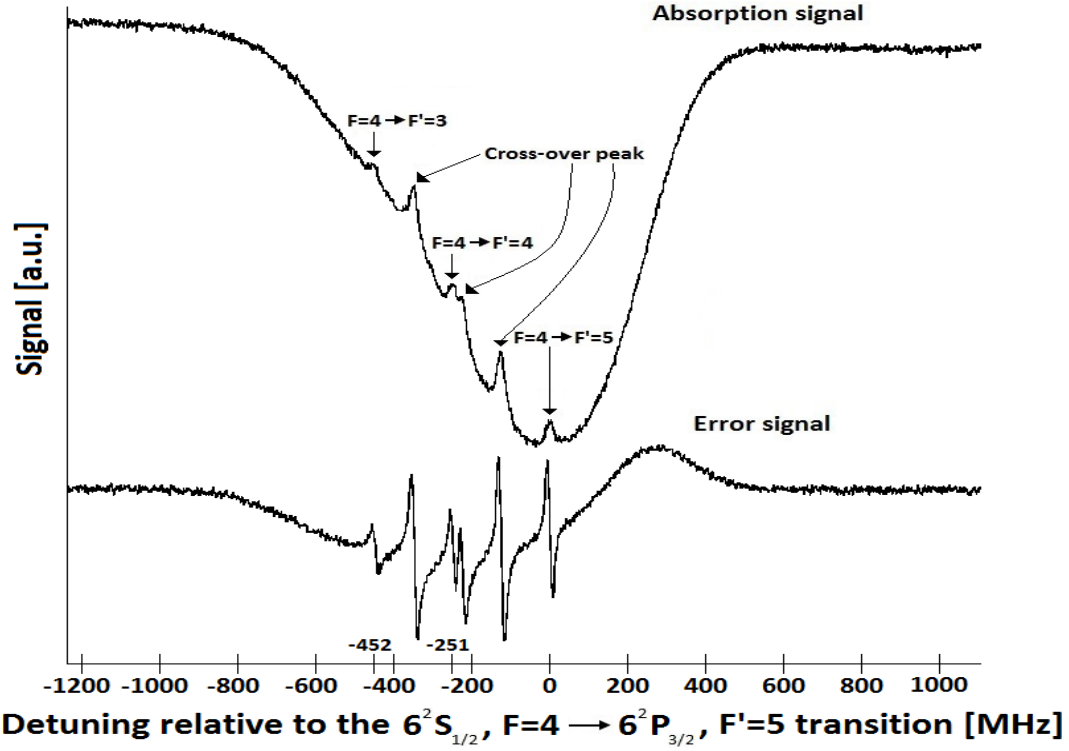

Figure 7. Absorption and error signals for the probe laser light, when the fiber-coupled EOM seen in figure 6 is turned off such that sidebands are not produced. The horizontal axis is the detuning relative to the D_2 line transition $6^2S_{1/2}, F = 4 \rightarrow 6^2P_{3/2}, F` = 5$. In the absorption signal we can see the peaks that reveal the rest frequency of the hyperfine transitions $6^2S_{1/2}, F = 4 \rightarrow 6^2P_{3/2}, F` = 3, 4, 5$; and we can also see the cross-over peaks. Using the information provided by [35], it is possible to know which peaks correspond to which peaks. The peaks corresponding to the transitions $6^2S_{1/2}, F = 4 \rightarrow 6^2P_{3/2}, F` = 3$ and 4 are respectively -452 MHz and -251 MHz away from the $6^2S_{1/2}, F = 4 \rightarrow 6^2P_{3/2}, F` = 5$ transition according to figure 4, and this information is used in this figure.

3.2 The microcells

The Cesium-133 atoms used in our experiments are in a gaseous form and are contained in glass microcells. The reason why the atoms are in a gaseous form is because the microcells are held near room temperature.

In the following I first present the general characteristics of the microcells used in the experiments described in this thesis. Next, I present the experiment that determines the atomic density of Cesium-133 vapor inside the microchannel of a microcell, and then the experiment that determines the Faraday angle for the linearly-polarized probe laser light as it passes through the microchannel of a microcell. From the Faraday angle measurements we will see how the spin-depolarization time T_1 of the Cesium-133 atoms can be extracted. Next, I explain how to investigate the spin states $|F = 4, m_F >$, where m_F = -4, ... 4, using the magneto-optical resonance method [11], and show experimentally how to obtain the magneto-optical resonance signal (MORS). By using the magneto-optical resonance method we will see how the transverse spin-coherence time T_2 of the Cesium-133 atoms can be extracted from the MORS.

Note that this section will make it clear why the particular experimental measurements mentioned in the above paragraph are important for the atom-membrane entanglement experiment described in chapter 4.

3.2.1 General characteristics of the microcells

In figure 8 (c) one can see how typical microcells used in the experiments look like. The microcells consist of a chip, seen in figure 8 (a), enclosed by a cylindrical body on which a stem is attached. The microcells are completely made out of borosilicate glass; the reason for that being that borosilicate glass has a very low coefficient of thermal expansion [27], making the dimensions of the microcell almost fixed if it is being heated, or cooled, for the reasons described below. As seen in figure 8 (a), there is a microchannel in the middle of the chip with dimensions 300 μm × 300 μm × 10 mm; the light originating from the probe laser passes through this microchannel. As seen in figures 8 (a) and (b), a microhole of a conical shape is drilled at the top of the chip to create a 20 μm entrance into the microchannel. The microhole allows Cesium-133 atom vapor to enter the microchannel. In the stem of the microcell there is a reservoir of Cesium-133 atoms in a solid form, and by heating, or cooling, the microcell one can control the amount of Cesium-133 atom vapor inside the microchannel that will enter through the microhole. At the both ends of the microchannel of the bare chip seen in figure 8 (a) one attaches 500 μm thick windows with vacuum tightness; these windows have an anti-reflection coating on the outside such that beam losses are reduced.

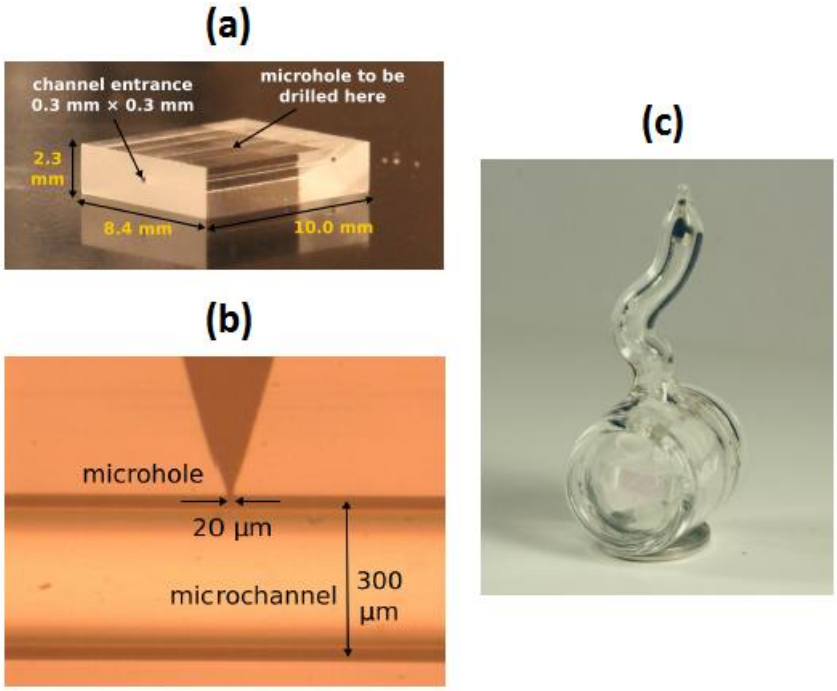

Figure 8. Photos of a typical microcell used in the experiments with Cesium-133 atoms. (a) bare chip, (b) close-up of the microchannel in the chip and the laser-drilled microhole, (c) finished microcell with windows that have anti-reflection coating. Photo credit: Kasper Jensen.

During the manufacturing process of the microcells, an alkene-based anti-relaxation coating is deposited through the microhole into the microchannel, where it then sticks to the walls of the microchannel; the particular compound used is alkene 1-nonadecene. As the Cesium-133 atoms collide with the walls of the microchannel, they can decohere from their quantum spin state; and with the coating in place it will take longer time for the Cesium-133 atoms to decohere than if there was no coating in place. As will be understood from section 3.2.3 by means of optical pumping the coating deposited on the walls of the microchannel can effectively allow us to conduct our atom-membrane experiment on timescales of milliseconds. However, if there was no coating in place, the timescale could be reduced to microseconds. The latter can be seen as the Cesium-133 atoms inside the microchannel follow a Maxwell-Boltzmann distribution for thermal motion, and so their mean thermal speed at room temperature of 20℃ (293 K) is

$$v_{mean} = \sqrt{\frac{8k_B T}{\pi m_{Cs}}} \approx 216 \text{ m/s} \quad , \tag{3.2.1.1}$$

where T = 293 K is the temperature. From eq. (3.2.1.1) we see that a Cesium-133 atom should collide with the wall of the microchannel every $\frac{L_{transverse}}{v_{mean}} \approx 0.5$ µs, where $L_{transverse} = 300$ µm is the transverse dimension of the microchannel as seen from figure 8 (b). The real reason why the anti-relaxation coating works the way it does is not fully understood in the literature; however, from the documented experimental work of Bouchiat and Brossel on relaxation of alkali atoms on paraffin surfaces [28], we can learn that alkali atoms (such as Cesium atoms) do not simply scatter

elastically off the coated surface, but rather stick fast to the coating for some finite time thereby increasing the time period in which the atoms spend inside the body of the microchannel.

Note that we can neglect the decoherence effects due to intra-atom collisions inside the microcells. This is justified as in alkali atom vapor, the interaction between the atoms is dominated by spin-exchange collisions [28]. The rate of the spin-exchange is given by [20]

$$\Gamma_{ex} = \rho \sigma_{ex} v_{mean} \quad , \tag{3.2.1.2}$$

where ρ is the atomic density, and σ_{ex} is the spin-exchange cross-section. Now, ρ is on the order of 10^{16} m^{-3} from the atomic density measurements in section 3.2.2 (at $\sim$20℃, according to the lab thermometer), $\sigma_{ex} \approx 2 \cdot 10^{-18} m^2$ for Cesium atoms [36], and $v_{mean} \approx 216$ m/s from eq. (3.2.1.1); plugging all this into eq. (3.2.1.2) we thus find that $T_{ex} \equiv \frac{1}{\Gamma_{ex}}$ is on the order of 1 second, which is significantly longer than the effective timescales of milliseconds of our atom-membrane experiment. It is reasonable to assume that $T_{ex} \gg 1$ ms for temperatures close to 20℃, and so, in the end, we can indeed neglect the decoherence effects due to intra-atom collisions inside the microcells.

We have many microcells in our lab and so we name them. Generic names such as e.g. "D4", "A2", "F3" are chosen. The capital letter refers to the generation of the mircocell, where "A" refers to the 1st generation, "B" refers to the 2nd generation, etc.; and the numbers 1, 2, 3 etc. refer to the number of the cell in the particular generation. The characterization measurements seen in the following subsections were performed using the microcell G2, which is not the same microcell that is used in the in the atom-membrane entanglement experiment described in chapter 4.

Note that in the experiments the probe laser light beam has a diameter of $\sim$110 μm measured at the middle of the microchannel; in this way the beam fills the microchannel with minimal power clipping. During the measurement time, the probe laser light will interact with all the Cesium-133 atoms inside the microchannel as they move around.

3.2.2 Atomic density measurements

In this subsection I present the experiment that determines the atomic density of Cesium-133 vapor inside the microchannel of a microcell.

In this experiment the light beam originating from the probe laser is aligned through the microchannel of a microcell and the transmitted light is picked up using a photodetector. The probe laser is scanned in frequency over both hyperfine manifolds of the D_2 line transition, and as the probe laser is scanned, the photodetector provides the signal seen in figure 9.

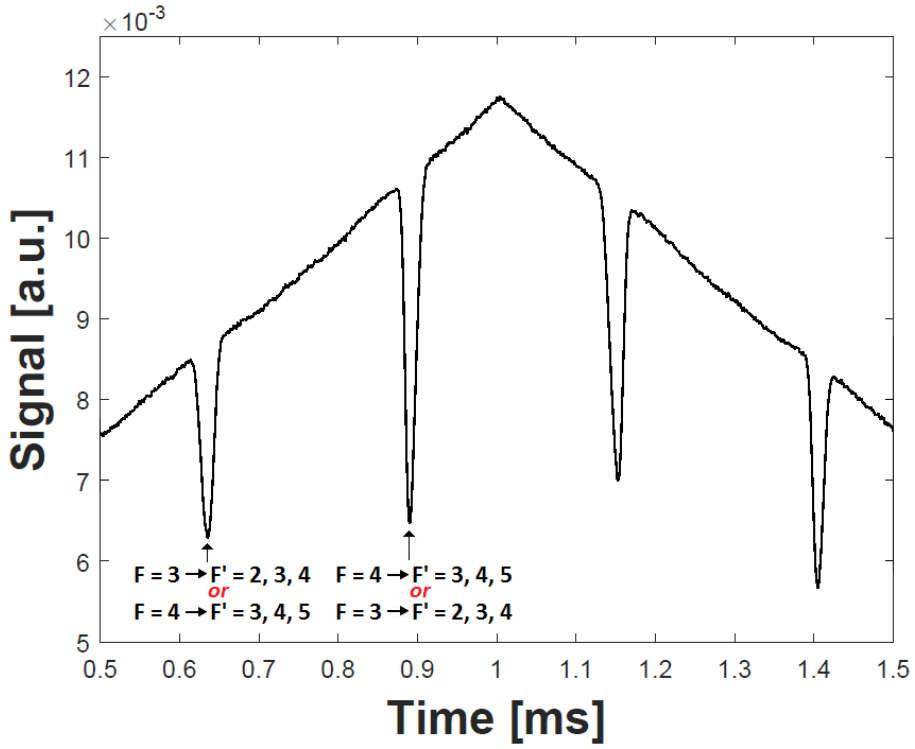

Figure 9. A signal obtained by sending probe laser light through the microchannel of the microcell G2 and then picking up the transmitted light using a photodetector. The photodector offset has been subtracted. The probe laser is scanned in frequency over both hyperfine manifolds of the D_2 line transition, and the pump and repump lasers are turned off. The two dips that are seen during either the rising or the falling scan correspond respectively to the Cesium-133 atoms in the energy levels $6^2S_{1/2}$, F = 3 and $6^2S_{1/2}$, F = 4 that undergo the transitions $6^2S_{1/2}, F = 3 \rightarrow 6^2P_{3/2}, F` = 2, 3, 4$ and $6^2S_{1/2}, F = 4 \rightarrow 6^2P_{3/2}, F` = 3, 4, 5$, as these atoms absorb the photons originating from the probe laser. These transitions follow from observing figure 4 and eqs. (3.1.2.1.a-d).

Here we see two dips appearing in both the *rising* and the *falling* scan of the probe laser. The two dips that are seen during either the rising or the falling scan correspond respectively to the Cesium-133 atoms in the energy levels $6^2S_{1/2}$, F = 3 and $6^2S_{1/2}$, F = 4 that absorb the photons originating from the probe laser. The light from the probe laser must be of sufficiently low power (on order of 100 nW) in order to minimize the depumping effects as much as possible. As the scanning changes from rising to falling, the same energy level is being passed twice. We observe in the figure that the dip after the rising edge is smaller than the preceding dip. This is caused by the depumping of the atoms from e.g. $6^2S_{1/2}$, F = 4, such that when the same laser frequency is reached for the second time there are fewer atoms in the same energy level to absorb the photons. Note that in order to understand which dip corresponds to which energy level one can shine on the atoms with the repump laser light. Since from section 3.1.2 we have that the repump laser light will put the atoms from $6^2S_{1/2}$, F = 3 to $6^2S_{1/2}$, F = 4 with the help of spontaneous emission decay, we should see that as the repump laser light is applied, then the dip corresponding to $6^2S_{1/2}$, F = 3 should disappear and the dip corresponding to $6^2S_{1/2}$, F = 4 should increase. When the check with the repump laser is performed, we can also perform a check on the pump laser, where we apply both pump and repump laser light and see how the pump laser light puts some of the atoms $6^2S_{1/2}$, F = 4 back to $6^2S_{1/2}$, F = 3; this would make sense since from section 3.1.2 we have that the pump laser light will put the atoms from $6^2S_{1/2}$, F = 4 to $6^2S_{1/2}$, F = 3 with the help of spontaneous emission decay.

Now, from the obtained signal we can calculate the atomic density of Cesium-133 vapor inside the microchannel by the use of the Lambert-Beer law [26], which tells us that the intensity of light of frequency ν that has propagated a distance z through an attenuating medium can be written as

$$I_\nu(z) = I_\nu(0)e^{-\rho z\sigma(\nu)} \quad , \tag{3.2.2.1}$$

where $I_\nu(0)$ is the incident intensity, ρ is the atomic density, and $\sigma(\nu)$ is the absorption cross-section. From the Lambert-Beert law given by eq. (3.2.2.1), we find for the atomic density ρ:

$$\rho = \frac{\int d\nu\{-\ln[I_\nu(z)/I_\nu(0)]\}}{z\int d\nu\sigma(\nu)} \quad , \tag{3.2.2.2}$$

where we now set z = L = 0,01 m, because it is the length of the microchannel as seen from figure 8 (a).

In order to determine the numerator in eq. (3.2.2.2), we first need to take the signal in figure 9 (where the photodetector offset is subtracted as mentioned in the figure text) from either the falling or the rising scan and convert this signal from the time domain (as it is on the figure) to the frequency domain. In order to do so, we observe figure A1 in appendix A and make use of the fact that the hyperfine splitting frequency between the energy levels $6^2S_{1/2}$ F = 3 and $6^2S_{1/2}$ F = 4 is $\nu_{HFS} = 9192$ MHz, such that the spacing between the dips can serve as a reference in order to convert from the time domain to the frequency domain. Next, we fit a line to the frequency-domain-signal with the dips omitted, and then divide each point on this signal with the corresponding point on the line we just fitted; and so the ratio $I_\nu(L)/I_\nu(0)$ can now be found for the different frequencies, and thus the numerator in eq. (3.2.2.2), where z = L, can be determined.

In order to determine the denominator in eq. (3.2.2.2) we can write the integral $\int d\nu\,\sigma(\nu)$ in terms of absorption oscillator strength of a transition between two states respectively characterized by the electron total angular momentum quantum numbers j and j′; it may be written as

$$f_{j,j'} \equiv \frac{\epsilon_0 m_{el} c^3}{2\pi e^2 \nu_0{}^2}\frac{2j'+1}{2j+1}\Gamma_{spon} \quad , \tag{3.2.2.3}$$

where m_{el} is the mass of an electron, ν_0 is the transition frequency, and Γ_{spon} is the spontaneous emission decay rate. For the Cesium-133 D_2 line transition, where j = 1/2 and j' = 3/2, we have, according to [43], that $f_{j,j'} = 0.7164$. In terms of $f_{j,j'}$ we have that that the integral

$$\int d\nu\,\sigma(\nu) = \pi c r_{el} f_{j,j'} = 1.9021 \cdot 10^{-6}\,\frac{m^2}{s} \quad , \tag{3.2.2.4}$$

where $r_{el} = 2.8179 \cdot 10^{-15}$ m is the (classical) radius of an electron. Using eq. (3.2.2.4) we are finally able to determine the atomic density of Cesium-133 vapor inside the microchannel of a microcell.

The signal seen in figure 9 thus shows that the atomic density of Cesium-133 vapor inside the microchannel of the microcell G2 is $\rho = 2.40 \cdot 10^{16}\ m^{-3}$. ρ here is obtained by averaging the result from both the falling and the rising scan.

Since the volume of the microchannel is $V_{channel}$ = $(0.3 \times 0.3 \times 10)$ mm^3 as seen from figure 8 (a), we find from the density $\rho = 2.40 \cdot 10^{16}\ m^{-3}$ the number of Cesium-133 atoms inside the microchannel to be $N_{Cs-133} = \rho V_{channel} = 2.16 \cdot 10^7$.

With a high number of Cesium-133 atoms inside the microchannel it becomes possible to put more atoms to the coherent spin state $|F = 4, m_F = 4>$ such that κ^2 can be increased.

3.2.3 Faraday angle and T_1 measurements

In this subsection I present the experiment that determines the Faraday angle of the linearly polarized probe light as it passes through the microchannel of a microcell. From the Faraday angle measurements we will see how the spin-depolarization time T_1 of the Cesium-133 atoms can be extracted.

The *Faraday angle* is an angle by which linearly-polarized light is rotated as it propagates through a given medium.

In our case, we have the linearly-polarized probe laser light propagating through the Cesium-133 vapor medium inside a microchannel of a microcell in the z-direction, and here the Faraday angle is defined as

$$\theta_F(t) \equiv \frac{a}{2}\langle \hat{J}_z(t)\rangle \quad , \tag{3.2.3.1}$$

where $\langle \hat{J}_z(t)\rangle$ refers to the mean value of the longitudinal Cesium-133 atomic ensemble total angular momentum operator $\hat{J}_z(t)$, and $a \equiv -\frac{\xi\lambda_{D2}^2}{16\pi A\Delta_5}$ as defined below eqs. (1.4.4.4.a-f).

A diagrammatic representation of the setup used for the Faraday angle $\theta_F(t)$ measurement is seen in figure 10. Here we place a ring magnet next to the microcell in order to subject the atoms to a static magnetic field pointing along the z-axis. The static magnetic field forces us to use the z-axis as the quantization axis as understood from section 1.5; and so, by sending a pulse of combined pump and repump light in the same direction as the magnetic field direction, being the z-direction, we are according to section 3.1.2 optically pumping the Cesium-133 atoms to the coherent spin state $|4,4>$. Right after the combined pump plus repump laser pulse we send a pulse of linearly-polarized probe light in the z-direction through the microchannel. The pulse sequence is produced using acousto-optic modulators (AOMs) with both the pump plus repump pulse and the probing pulse being of 50 ms duration each.

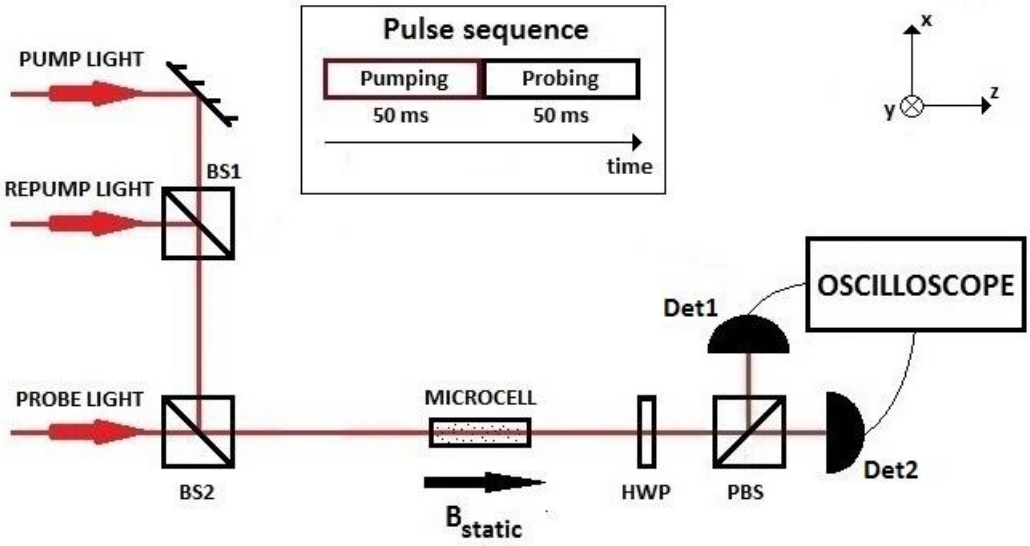

Figure 10. A diagrammatic representation of the experimental setup used for the Faraday angle $\theta_F(t)$ measurement, where $\theta_F(t)$ is defined in eq. (3.2.3.1). Photocurrents from photodetectors Det1 and Det2 travel to an oscilloscope which is used to read out $\theta_F(t)$. In the figure we have that BS stands for 50/50 beam splitter, PBS stands for polarizing beam splitter, HWP stands for half-wave plate, and $\mathbf{B}_{\text{static}}$ is the static magnetic field pointing along the z-axis that the Cesium-133 atoms in the microcell are subject to.

Let us now use Jones matrix calculus introduced in appendix D, and find the intensities picked up by respectively the photodetector Det1 and Det2. From these intensities we will be able to determine the Faraday angle $\theta_F(t)$ in eq. (3.2.3.1). By making use of Jones matrix calculus, we will need to treat the probe laser light classically.

From eq. (D.1) we have that the Jones vector for the probe light before the microcell in figure 10 is

$$\mathbf{V}_{\text{in},\theta_F} \equiv \begin{bmatrix} E_H \\ E_V \end{bmatrix} = \begin{bmatrix} E_{0H} e^{i(\varphi_H - \omega_0 t)} \\ E_{0V} e^{i(\varphi_V - \omega_0 t)} \end{bmatrix} = \begin{bmatrix} E_{0H} e^{i(\varphi_H - \omega_0 t)} \\ E_{0H} e^{i(\varphi_H - \omega_0 t)} \end{bmatrix} , \qquad (3.2.3.2)$$

where E_H and E_V are the (complex) horizontal and vertical polarization components, respectively, of the electric field $\mathbf{E}(z,t) = \mathbf{V}_{\text{in},\theta_F} e^{ikz}$ of a monochromatic plane wave of light, which in the present case describes the probe laser light, which travels along the z-axis, where k is the angular wave number and ω_0 is the angular frequency of the probe laser light with $k = \omega_0/c$, and E_{0H} and E_{0V} are the amplitudes of respectively E_H and E_V with φ_H and φ_V being the respective phases. In the last equality we assume that $E_{0H} = E_{0V}$ and $\varphi_H = \varphi_V$.

The Jones matrices that we will use in the present case are: $\bar{\bar{\mathbf{M}}}_R(\theta)$, $\bar{\bar{\mathbf{M}}}_{RWP}(\varphi,\theta)$ and $\bar{\bar{\mathbf{M}}}_{LPOL}(p_H, p_V)$, which respectively are the Jones matrix for a rotator defined in eq. (D.3.a), the Jones matrix for a rotated wave plate defined in eq. (D.3.b) and the Jones matrix for a perfect linear polarizer defined in eq. (D.3.c). Here θ is the angle of the fast axis of a wave plate with respect to the horizontal axis, $\varphi \equiv \varphi_H - \varphi_V$, and $p_H, p_V = 0$ or 1.

Observing figure 10 we now find

1. the Jones vector for the light incident on the Det1:

$$\mathbf{V}_{1,\theta_F} = \bar{\bar{\mathbf{M}}}_{PBS,r}\bar{\bar{\mathbf{M}}}_{HWP}\bar{\bar{\mathbf{M}}}_{MICROCELL}\mathbf{V}_{in,\theta_F} = \begin{bmatrix} 0 \\ E_{0H}\left(\sin\left(\theta_F(t)\right) - \cos\left(\theta_F(t)\right)\right)e^{i(\varphi_H - \omega_0 t)} \end{bmatrix} \quad . \quad (3.2.3.3.a)$$

2. the Jones vector for the light incident on the Det2:

$$\mathbf{V}_{2,\theta_F} = \bar{\bar{\mathbf{M}}}_{PBS,tr}\bar{\bar{\mathbf{M}}}_{HWP}\bar{\bar{\mathbf{M}}}_{MICROCELL}\mathbf{V}_{in,\theta_F} = \begin{bmatrix} E_{0H}\left(\sin\left(\theta_F(t)\right) + \cos\left(\theta_F(t)\right)\right)e^{i(\varphi_H - \omega_0 t)} \\ 0 \end{bmatrix} \quad . \quad (3.2.3.3.b)$$

In eqs. (3.2.3.3.a-b) we assume that the Cesium-133 atoms inside the microchannel of a microcell act to rotate the linear polarization of the probe laser light by the Faraday angle $\theta_F(t)$, and so the Jones matrix for the microcell is $\bar{\bar{\mathbf{M}}}_{MICROCELL} \equiv \bar{\bar{\mathbf{M}}}_R\left(\theta_F(t)\right)$; the HWP is assumed to behave as a non-rotated half-wave plate which introduces the phase shift $\varphi = \pi$ between the horizontal and vertical components of the light such that the light intensities that are picked up by the Det1 and Det2 are the same, when the microcell is not present, and so the Jones matrix for the HWP is $\bar{\bar{\mathbf{M}}}_{HWP} = \bar{\bar{\mathbf{M}}}_{RWP}(\pi, 0)$; the polarizing beam splitters used in our experiments transmit the horizontally-polarized component of the light and reflect the vertically-polarized component of the light, and so the Jones matrix for the PBS reflecting the light is $\bar{\bar{\mathbf{M}}}_{PBS,r} \equiv \bar{\bar{\mathbf{M}}}_{LPOL}(0,1)$ and the Jones matrix for the PBS transmitting the light is $\bar{\bar{\mathbf{M}}}_{PBS,tr} \equiv \bar{\bar{\mathbf{M}}}_{LPOL}(1,0)$.

From eqs. (3.2.3.3.a-b) and (D.2) we now find

1. the differences in the intensities picked up by respectively the Det1 and Det2 to be

$$I_{1,\theta_F} - I_{2,\theta_F} \propto \mathbf{V}^*_{1,\theta_F} \bullet \mathbf{V}_{1,\theta_F} - \mathbf{V}^*_{2,\theta_F} \bullet \mathbf{V}_{2,\theta_F} = 4E^2_{0H}\sin\left(\theta_F(t)\right)\cos\left(\theta_F(t)\right) \approx 4E^2_{0H}\theta_F(t) \quad , \quad (3.2.3.4.a)$$

where the approximations $\sin\left(\theta_F(t)\right) \approx \theta_F(t)$ and $\cos\left(\theta_F(t)\right) \approx 1$ are used.

2. the sum of the intensities picked up by respectively the Det1 and Det2 to be

$$I_{1,\theta_F} + I_{2,\theta_F} \propto \mathbf{V}^*_{1,\theta_F} \bullet \mathbf{V}_{1,\theta_F} + \mathbf{V}^*_{2,\theta_F} \bullet \mathbf{V}_{2,\theta_F} = 2E^2_{0H} \quad , \quad (3.2.3.4.b)$$

Eqs. (3.2.3.4.a-b) tell us that

$$I_{1,\theta_F} - I_{2,\theta_F} = 2\left(I_{1,\theta_F} + I_{2,\theta_F}\right)\theta_F(t) \quad \Rightarrow$$

$$\theta_F(t) = \frac{I_{1,\theta_F} - I_{2,\theta_F}}{2\left(I_{1,\theta_F} + I_{2,\theta_F}\right)} \quad . \quad (3.2.3.5)$$

The Faraday angle $\theta_F(t)$ measurement results for different probe light powers using the microcell G2 are seen in figure 11. We observe that $\theta_F(t)$ decays in time. $\theta_F(t)$'s decay in time follows from the definition of $\theta_F(t)$ in eq. (3.2.3.1), where it is seen that $\theta_F(t) \propto \langle \hat{J}_z(t) \rangle$. Assuming that $\langle \hat{J}_z(t) \rangle = \langle \hat{J}_z(0) \rangle e^{-t/T_1}$, where T_1 is called the spin-depolarization time, and is a concept, whose origin is explained in appendix B, we see that under this assumption T_1 defines the time at which $\langle \hat{J}_z(t) \rangle$ has

decayed by the factor of $\frac{1}{e}$ from its initial value. Since $\theta_F(t) \propto \langle \hat{J}_z(t) \rangle$, it must thus under the assumption that $\langle \hat{J}_z(t) \rangle$ decays exponentially in time follow that $\theta_F(t)$ also decays exponentially in time and that T_1 now defines the time at which both $\langle \hat{J}_z(t) \rangle$ and $\theta_F(t)$ have decayed by the factor of $\frac{1}{e}$ from their initial value. The assumption regarding the exponential decay is made use of when extracting the Faraday angle $\theta_F(0)$, which is the Faraday angle at the beginning of probing, i.e. at $t = 0$, and the spin-depolarization time T_1, from the $\theta_F(t)$ measurements. In figure 12 (a) we can see that $\theta_F(0) \sim 1.38\,°$ for the microcell G2. $\theta_F(0)$ should stay constant with respect to probe light power P_{probe}, because $t = 0$ signifies the beginning of the probing, where the depumping of the Cesium-133 atoms from $|4,4>$ due to probing cannot yet happen, and there is also nothing in the definition of the Faraday angle $\theta_F(t)$, i.e. eq. (3.2.3.1), that would indicate that $\theta_F(0)$ shouldn't stay constant. One of the reasons why $\theta_F(0)$ is seen not to be constant might be because the microcell was exposed to stray magnetic fields. In such a case the optical pumping becomes compromised such that a different amount of Cesium-133 atoms reside in the coherent spin state $|4,4>$ at $t = 0$ for the different measurements, and thus $\langle \hat{J}_z(0) \rangle \propto \theta_F(0)$ is different for the different measurements. Note that neither the raw data nor the fitting can provide us with a constant $\theta_F(0)$. See section 3.3, where we discuss how in the remaining experiments we shield the microcell from stray magnetic fields. In figure 12 (b) we can see how the inverse of T_1 depends on the probe light power. We see that using a higher probe light power will decrease T_1; this is because for higher probe light power there is a higher chance of the depumping of the Cesium-133 atoms from $|4,4>$, because of the power broadening. Assuming that we may fit a linear curve to the data points seen in figure 12 (b), we can extract T_1 for the microcell G2, when there is no probe light; in such a case we obtain $T_1 \sim 2.75$ ms.

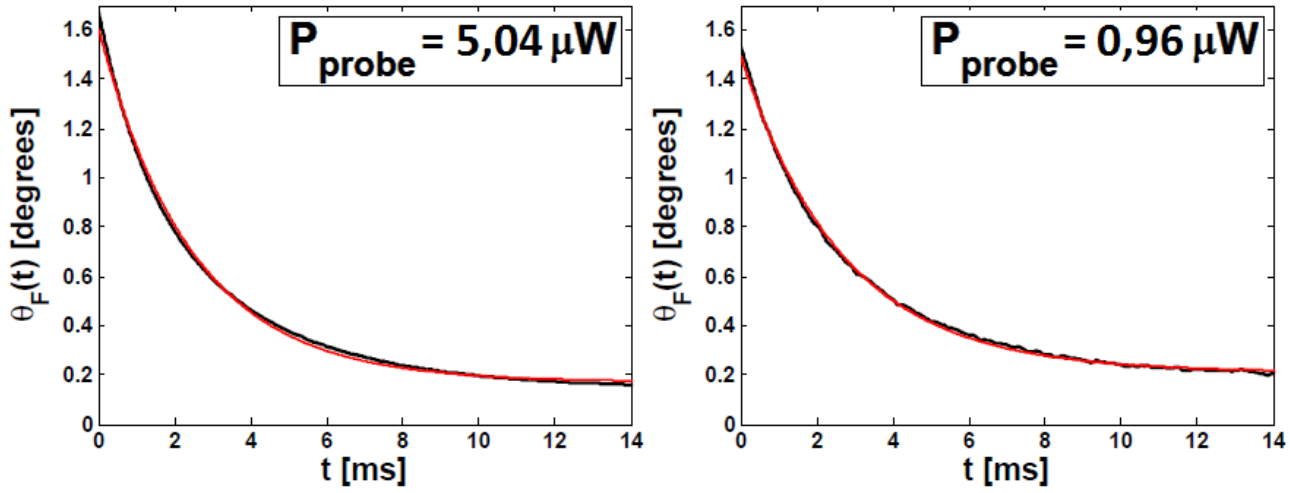

Figure 11. Experimentally obtained graphs, seen as black lines, showing how the Faraday angle θ_F behaves in time t for different probe light powers P_{probe} (seen in the legends) using the microcell G2. The red lines are fits to the experimentally obtained graphs. In order to make reasonably good fitting in the region from 0 to 14 ms, exponential curves with added constant offsets are fitted. If we assume that the decay of $\theta_F(t)$ in the region from 0 to 14 ms follows an exponential decay without an added constant offset, it must thus follow that there is a constant offset produced by the experimental procedure. In order to extract the Faraday angle $\theta_F(0)$, which is the Faraday angle at the beginning of probing, i.e. at $t = 0$, and the spin-depolarization time T_1, we must thus subtract the constant offsets. Note that if the experimental procedure does not, however, produce the constant offsets, it must thus follow that $\theta_F(t)$ does not follow a simple exponential decay.

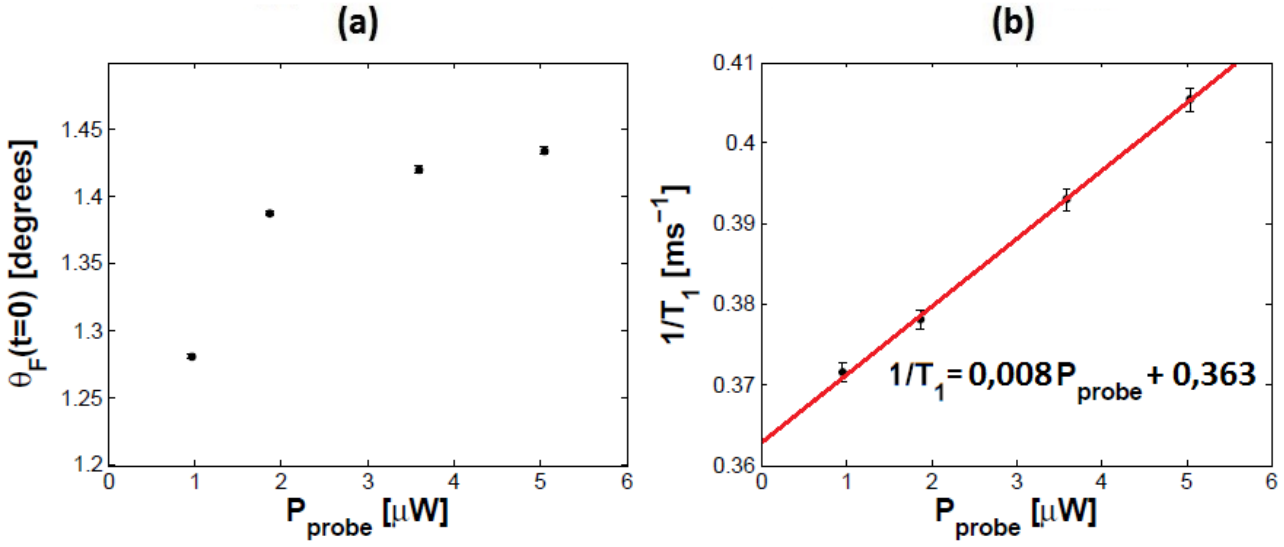

Figure 12. (a) Experimentally obtained data points, seen as black dots, showing how the Faraday angle $\theta_F(0)$, which is the Faraday angle at the beginning of probing, i.e. at time $t = 0$, varies for different probe light powers P_{probe} using the microcell G2. As explained in the text, $\theta_F(0)$ should stay constant with respect to P_{probe}. Taking the average of $\theta_F(0)$ at the different P_{probe}, we nevertheless conclude that $\theta_F(0) \sim 1.38$ ° for the microcell G2. (b) Experimentally obtained data points, seen as black dots, showing how the inverse of the spin-depolarization time T_1 varies for different probe light powers P_{probe} using the microcell G2. Assuming that we may fit a linear curve to the data points, seen as a red line, with the fit being $1/T_1 = 0.008P_{probe} + 0.363$, we can extract the T_1 for the microcell G2, when there is no probe light; in such a case we obtain $T_1 \sim 2.75$ ms.

The measurements here show that by means of optical pumping the coating deposited on the walls of the microchannel can effectively allow us to conduct our atom-membrane experiment on timescales of milliseconds.

3.2.4 MORS and T_2 measurements

In this subsection I explain how to investigate the spin states $|F = 4, m_F>$, where m_F = -4, ... 4, using the magneto-optical resonance method and show experimentally how to obtain the magneto-optical resonance signal (MORS). By using the magneto-optical resonance method we will see how the transverse spin-coherence time T_2 of the Cesium-133 atoms can be extracted from the MORS.

A diagrammatic representation of the setup used for this experiment is seen in figure 13. Here we place the microcell containing Cesium-133 atoms inside a magnetic shield, which can subject the atoms to a static magnetic field pointing along the z-axis and a radio frequency (RF) magnetic field oscillating on the x-axis; the magnetic shield used in this experiment is described in section 3.3. According to appendix A the static magnetic field will make the energy of each Zeeman energy levels m_F change as shown in figure A1; here we see that the frequency difference between the two closest sets of two nearby $m_f -$ lines in figure A1 is the quadratic Zeeman splitting frequency $\nu_{QZ} = \frac{2\nu_L{}^2}{\nu_{HFS}}$ given by eq. (A.5), where $\Omega_L \equiv 2\pi\nu_L$ is the Larmor frequency and ν_{HFS} is the hyperfine spilling frequency. To understand the role the RF magnetic field we write down the Hamiltonian describing the interaction of the static and RF magnetic fields with the atoms as

$$\hat{H}_{B_{static},B_{RF}} = \hat{H}_{B_{static}} + \hat{H}_{B_{RF}} = \frac{\mu_B g}{\hbar}\hat{\mathbf{J}}(t) \bullet \mathbf{B} + O(B^2) \quad , \tag{3.2.4.1}$$

where the static magnetic field along the z-axis contributes by $\hat{H}_{B_{static}} = \frac{\mu_B g}{\hbar}\hat{J}_z(t)B_{static} + O(B_{static}^2)$ to the Hamiltonian, where the second order contribution $O(B_{static}^2)$ incorporates the quadratic Zeeman splitting frequency $\nu_{QZ} = \frac{2{\nu_L}^2}{\nu_{HFS}}$ (which was derived to second order in appendix A), and the RF magnetic field oscillating on the x-axis contributes by $\hat{H}_{B_{RF}} = \frac{\mu_B g}{\hbar}\hat{J}_x(t)|B_{RF}|\cos(\omega_{RF}t + \varphi_{RF})$ to the Hamiltonian, where $|B_{RF}|$ is the amplitude of the RF magnetic field $\mathbf{B}_{RF}$ of angular frequency ω_{RF} and phase φ_{RF}. Note that for simplicity the second order contribution $O(B_{RF}^2)$ is neglected.

With the z-axis as the quantization-axis let us now write the total angular momentum operators $\hat{J}_x(t), \hat{J}_y(t), \hat{J}_z(t)$ of N Cesium-133 atoms in the hyperfine structure energy level F as

$$\hat{J}_x = N\sum_{m_F=-F}^{F-1}\frac{C(F,m_F)}{2}\left\{\hat{\sigma}_{m_F+1,m_F} + \hat{\sigma}_{m_F,m_F+1}\right\} \quad , \tag{3.2.4.2.a}$$

$$\hat{J}_y = N\sum_{m_F=-F}^{F-1}\frac{C(F,m_F)}{2i}\left\{\hat{\sigma}_{m_F+1,m_F} - \hat{\sigma}_{m_F,m_F+1}\right\} \quad , \tag{3.2.4.2.b}$$

$$\hat{J}_z = N\sum_{m_F=-F}^{F} m_F\hat{\sigma}_{m_F,m_F} \quad , \tag{3.2.4.2.c}$$

where $\hbar = 1$ is used, the time t dependence is suppressed, $C(F, m_F) \equiv \sqrt{F(F+1) - m_F(m_F+1)}$, and

$$\hat{\sigma}_{i,j} = \frac{1}{N}\sum_{k=1}^{N}\hat{\sigma}_{i,j}^{(k)} = \frac{1}{N}\sum_{k=1}^{N}|i\rangle_k\langle j|_k \tag{3.2.4.3}$$

is the density operator for the $m_F -$ levels of the $F -$ level, where i, j = m_F = -F, -F + 1, ... , F and the sum is done over N atoms, where $\hat{\sigma}_{i,j}^{(k)}$ is density operator for a single Cesium-133 atom, used in chapter 1.

For simplicity we now set N = 1; and so, using the density operator $\hat{\sigma}_{i,j}$ in eq. (3.2.4.3) we can rewrite the Hamiltonian $\hat{H}_{B_{static},B_{RF}}$ as

$$\hat{H}_{B_{static},B_{RF}} = \sum_{m_F=-F}^{F}\hbar\omega_{m_F}\hat{\sigma}_{m_F,m_F} + \frac{\mu_B g}{4\hbar}\sum_{m_F=-F}^{F-1}C(F,m_F)\left\{\hat{\sigma}_{m_F+1,m_F}B_{RF}e^{i\omega_{RF}t} + h.c.\right\} \quad , \tag{3.2.4.4}$$

where $\hbar\omega_{m_F}$ is the energy of the $m_F -$ level, and $B_{RF} = |B_{RF}|e^{-i\varphi_{RF}}$ is the complex amplitude of $\mathbf{B}_{RF}$. The first term is the static magnetic field contribution, and because of the density operators $\hat{\sigma}_{m_F,m_F}$, which measure the probability for Cesium-133 atoms of being in the ground spin state $|F, m_F>$, we have that it is responsible for the $m_F -$ level energy splitting. The second term is the RF magnetic field contribution in the rotating-wave approximation, where we neglect the fast-oscillating terms, and because of the density operators $\hat{\sigma}_{m_F+1,m_F}$ and $\hat{\sigma}_{m_F,m_F+1}$, which express coherence between the ground spin states $|F, m_F>$ and $|F, m_{F+1}>$, we have that it is responsible for driving the transitions between the $m_F -$ levels.

Now, to understand how the Cesium-133 atoms are transferred between different spin states $|F, m_F>$, where m_F = -F, -F + 1, ... , F, we must know how the off-diagonal density operators $\hat{\sigma}_{i,j}$, $i \neq j$, evolve in time; and to do so, we use the Lindblad-Heisenberg equation of motion

$$\frac{\partial}{\partial t}\hat{\sigma}_{i,j} = \frac{1}{i\hbar}\left[\hat{\sigma}_{i,j}, \hat{H}_{B_{static},B_{RF}}\right] - \frac{\Gamma_{i,j}}{2}\hat{\sigma}_{i,j} \quad (i \neq j) \quad , \tag{3.2.4.5}$$

where the second term is the decay term that is due to the interaction with the environment, with $\Gamma_{i,j}$ being the decay rate of the transverse total angular momentum operators $\hat{J}_x(t)$ and $\hat{J}_y(t)$ for $m_F -$ level transition $i \rightarrow j$. We have that $\Gamma_{i,j} \equiv \left(\pi T_{2,i\rightarrow j}\right)^{-1}$, where $T_{2,i\rightarrow j}$ is the transverse spin-coherence time for $m_F -$ level transition $i \rightarrow j$. Transverse spin-coherence time is a concept, whose origin is explained in appendix B.

In order to understand the method for solving eq. (3.2.4.5), we can pick out a single example. By inserting the Hamiltonian $\hat{H}_{B_{static},B_{RF}}$ in eq. (3.2.4.5) for e.g. $\hat{\sigma}_{1,2}$ we obtain

$$\frac{\partial}{\partial t}\hat{\sigma}_{1,2} = \frac{1}{i\hbar}\left[\hat{\sigma}_{1,2}, \hat{H}_{B_{static},B_{RF}}\right] - \frac{\Gamma_{1,2}}{2}\hat{\sigma}_{1,2} = \left(\frac{\omega_{2,1}}{i} - \frac{\Gamma_{1,2}}{2}\right)\hat{\sigma}_{1,2} -$$

$$-\frac{\mu_B g}{4i\hbar^2}\left\{C(F,1)\left[\hat{\sigma}_{2,2} - \hat{\sigma}_{1,1}\right]B_{RF}e^{-i\omega_{RF}t} + \left[C(F,0)\hat{\sigma}_{0,2} - C(F,2)\hat{\sigma}_{1,3}\right]B_{RF}^{*}e^{i\omega_{RF}t}\right\} \quad , \tag{3.2.4.6}$$

where $\omega_{b_1,b_2} \equiv \omega_{b_1} - \omega_{b_2}$ is the transition angular frequency between the energy levels with $m_F = b_1$ and $m_F = b_2$, where $b_1 \neq b_2$. Now, in this experiment we can assume that the angle by which the mean of total angular momentum operator $\hat{\mathbf{J}}(t)$ deviates from being oriented from z-axis is much less than unity, and so it is justified that $\hat{\sigma}_{0,2}, \hat{\sigma}_{1,3} \rightarrow 0$ in eq. (3.2.4.6). Also, since ω_{RF} is close to the transition angular frequency $\omega_{a,b}$ in this experiment, we can define the slowly varying operators

$$\tilde{\sigma}_{i,j} \equiv \hat{\sigma}_{i,j}e^{i\omega_{RF}t} \quad , \tag{3.2.4.7}$$

such that eq. (3.2.4.6) now is turned to

$$\frac{\partial}{\partial t}\tilde{\sigma}_{1,2} = \left(i(\omega_{RF} - \omega_{2,1}) - \frac{\Gamma_{1,2}}{2}\right)\tilde{\sigma}_{1,2} - \frac{\mu_B g}{4i\hbar^2}C(F,1)\left[\hat{\sigma}_{2,2} - \hat{\sigma}_{1,1}\right]B_{RF} \quad . \tag{3.2.4.8}$$

Assuming that in this experiment the spin-depolarization time T_1 is longer than the transverse spin-coherence time $T_{2,i\rightarrow j}$, i.e. $T_1 > T_{2,i\rightarrow j}$, we have that $\tilde{\sigma}_{1,2}$ will follow $\left(\hat{\sigma}_{2,2} - \hat{\sigma}_{1,1}\right)$ adiabatically, such that we can assume that $\tilde{\sigma}_{1,2}$ stays constant in time, i.e. $\frac{\partial}{\partial t}\tilde{\sigma}_{1,2} = 0$. Using this assumption in eq. (3.2.4.8) we get

$$\hat{\sigma}_{1,2} = \frac{\mu_B g B_{RF} C(F,1)e^{-i\omega_{RF}t}}{4i\hbar^2\left(i\left(\omega_{RF} - \omega_{2,1}\right) - \frac{\Gamma_{1,2}}{2}\right)}\left[\hat{\sigma}_{2,2} - \hat{\sigma}_{1,1}\right] \quad . \tag{3.2.4.9}$$

We can use the above method for finding all $\hat{\sigma}_{i,j}$, $i \neq j$; and substituting these into eqs. (3.2.4.2.b) and (3.2.4.2.c) for respectively $\hat{J}_x(t)$ and $\hat{J}_y(t)$, we obtain [1]

$$\hat{J}_x(t) = \mathrm{Re}\left\{\frac{i\mu_B g B_{RF} N}{4\hbar^2}\sum_{m_F=-F}^{F-1}\frac{[F(F+1)-m_F(m_F+1)]e^{i\omega_{RF}t}}{i(\omega_{m_F+1,m_F}-\omega_{RF})-\frac{\Gamma_{m_F+1,m_F}}{2}}\left[\hat{\sigma}_{m_F+1,m_F+1}-\hat{\sigma}_{m_F,m_F}\right]\right\} \quad , \quad (3.2.4.10.a)$$

$$\hat{J}_y(t) = \mathrm{Im}\left\{\frac{i\mu_B g B_{RF} N}{4\hbar^2}\sum_{m_F=-F}^{F-1}\frac{[F(F+1)-m_F(m_F+1)]e^{i\omega_{RF}t}}{i(\omega_{m_F+1,m_F}-\omega_{RF})-\frac{\Gamma_{m_F+1,m_F}}{2}}\left[\hat{\sigma}_{m_F+1,m_F+1}-\hat{\sigma}_{m_F,m_F}\right]\right\} \quad . \quad (3.2.4.10.b)$$

Note that $\mathrm{Re}\{u\} = \frac{1}{2}(u + \bar{u})$ and $\mathrm{Im}\{u\} = \frac{1}{2i}(u - \bar{u})$, where u is a complex number.

Observing eqs. (3.2.4.10.a-b) for $\hat{J}_x(t)$ and $\hat{J}_y(t)$ we see that they can be interpreted as describing a total amount of 2F two-level systems that all respond to an RF magnetic field of angular frequency ω_{RF}. Two adjacent energy levels $m_F + 1$ and m_F will correspond to one of the 2F two-level systems with resonance frequency ω_{m_F+1,m_F} and FWHM line width Γ_{m_F+1,m_F}. We have that two adjacent two-levels systems with the resonance frequencies ω_{m_F+1,m_F} and ω_{m_F+2,m_F+1}, respectively, are split by the quadratic Zeeman splitting angular frequency $\omega_{QZ} = 2\pi\nu_{QZ} = \frac{4\pi{\nu_L}^2}{\nu_{HFS}}$. From [1] we have that the line width

$$\Gamma_{m_F+1,m_F} = \Gamma_{com} + \Gamma_{pump}\frac{19-2m_F-m_F^2}{4} \quad . \quad (3.2.4.11)$$

Γ_{com} is the decay rate common to all transitions independent of m_F; the cause for this type of decay include different loss mechanisms common to all atoms and the fact that the different atoms in the microchannel may be subject to a different magnetic field, as the magnetic field that subjects the atoms might be of different strength at different points in space and it might not be homogeneously pointing along the same direction. Γ_{pump} is the decay rate caused by the optical pumping process and it varies for a given transition between the $m_F -$ levels. Note that Γ_{pump} is defined such that for the $m_F = 4 \rightarrow m_F = 3$ transition for F = 4 we have $\Gamma_{4,3} = \Gamma_{com} + \Gamma_{pump}$.

We observe that $\hat{J}_x(t)$ and $\hat{J}_y(t)$ in eqs. (3.2.4.10.a-b) can tell us how well we can pump the Cesium-133 atoms in the microchannel of a microcell to the coherent spin state $|4,4>$, and thus how well in our experiments we can polarize the Cesium-133 atomic ensemble total angular momentum vector operator $\hat{\mathbf{J}}(t)$ along the quantization-axis; for this reason we define a polarization parameter p, which quantifies how well $\hat{\mathbf{J}}(t)$ is polarized along the quantization-axis:

$$p \equiv \frac{1}{4}\sum_{m_F=-4}^{4} m_F\langle\hat{\sigma}_{m_F,m_F}\rangle = \frac{\langle\hat{J}_z(t)\rangle}{4N} = \frac{J_{z,C_a}}{4N} = \frac{C_{a,t}}{N} \quad , \quad (3.2.4.12)$$

where $\langle . \rangle$ refers to the mean value, and in the third equality we set $\langle\hat{J}_z(t)\rangle = \langle 4,4|\hat{J}_z(t)|4,4\rangle = \hbar J_{z,C_a}(t) = \hbar J_{z,C_a} \equiv \hbar 4 C_{a,t}$, where $C_{a,t} \in \mathbb{N}$ in the present case denotes the number of Cesium-133 atoms in the coherent spin state $|F = 4, m_F = 4>$ at time t, and $N \geq C_{a,t}$; such that if p = 1, then all N Cesium-133 atoms lie in the coherent spin state $|4,4>$, and if p = 0, then there are no Cesium-133 atoms in the coherent spin state $|4,4>$. Note that in eq. (3.2.4.12) $\hbar = 1$ is assumed.

Note that from the Cesium-133 atom Hamiltonian $\widehat{H}_{atoms}$ in eq. (2.1.4.a) in chapter 2, where the atom-membrane protocol is described, we see that we care most for the decay rate $\Gamma_{4,3} = \left(\pi T_{2,4\to3}\right)^{-1}$. In a case, where $\hat{\mathbf{J}}(t)$ is well-polarized along the quantization-axis, we define $T_2 \equiv T_{2,4\to3}$ as *the* transverse spin-coherence time.

Now, from section 1.4 and eq. (1.4.4.7.a) we know that the probe laser light in this experiment will carry information about the modulated $\hat{J}_x(t)$, when it will pass the atoms, because $\hat{S}_y^{out}(t) \propto \hat{J}_x(t)$. In order to measure $\hat{S}_y^{out}(t)$ we make use of the balanced homodyne detection scheme seen in figure C1 (b) (i) in appendix C. In the language of appendix C, we have that the light that is subject to the balanced homodyne detection is composed of two light fields: the signal field described by the quadrature operators of the signal field and the local oscillator (LO) that is treated as a classical light field. The quadrature operators of the signal field in the present case are the Stokes operators $\hat{S}_y^{out}(t)$ and $\hat{S}_z^{out}(t)$ that satisfy eqs. (C.4.b-c); and the LO in the present case is the probe laser light with the assumption that the quantum fluctuations of this light are neglected. Since by observing figure 13 we see that the phase difference between the signal field and the LO is zero, then by figure C1 (b) (i) and eqs. (C.2) and (C.7.a) we have that the balanced homodyne detection will yield the subtracted photocurrent $i(t) \equiv i_2(t) - i_1(t) \propto \langle \hat{S}_y^{out}(t) \rangle \propto \langle \hat{J}_x(t) \rangle$, where $\langle . \rangle$ refers to the mean value, and $i_1(t)$ and $i_1(t)$ are the photocurrents resulting from the photodetectors Det1 and Det2, respectively, such that

$$i(t) = \alpha \langle \hat{J}_x(t) \rangle = \alpha Re\{A(t)\} = \alpha[Re\{A(\omega_{RF})\}\cos(\omega_{RF}t) - Im\{A(\omega_{RF})\}\sin(\omega_{RF}t)] \quad , \quad (3.2.4.13)$$

where α is a constant that depends on experimental parameters, and $A(t) \equiv A(\omega_{RF})e^{i\omega_{RF}t} = (Re\{A(\omega_{RF})\} + iIm\{A(\omega_{RF})\})\left(\cos(\omega_{RF}) + i\sin(\omega_{RF})\right)$ is the mean value of the expression in the curly brackets in eq. (3.2.4.10.a).

Experimentally, a lock-in amplifier can provide us with the amplitudes of the sine and cosine components in $i(t)$ in eq. (3.2.4.13). By taking the sum of the squared amplitudes of the sine and cosine components in $i(t)$ in eq. (3.2.4.13) yields the magneto-optical resonance signal

$$MORS(\omega_{RF}) \equiv \alpha^2 |A(\omega_{RF})|^2 \quad . \quad (3.2.4.14)$$

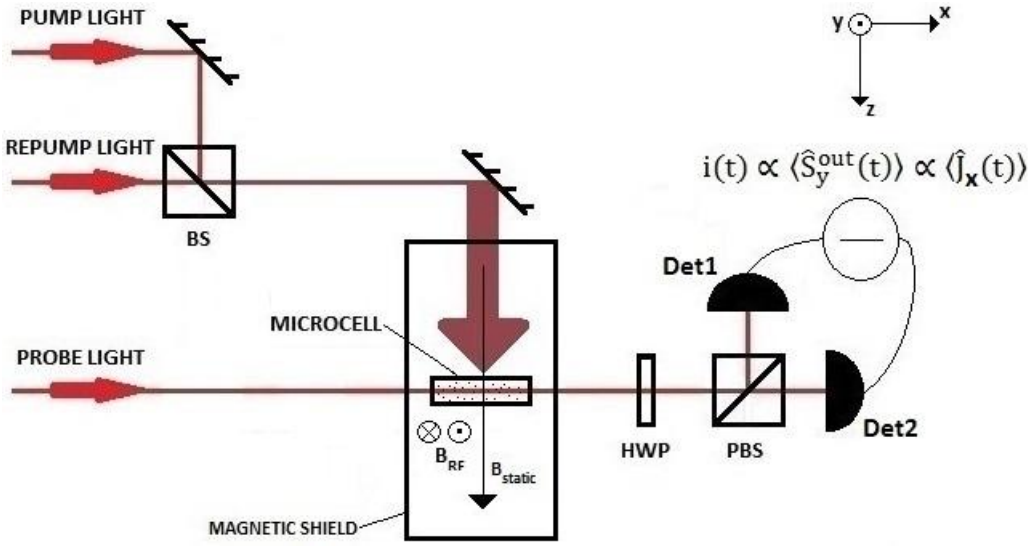

Figure 13. A diagrammatic representation of the experimental setup used for the measurement of the magneto-optical resonance signal (MORS) given by eq. (3.2.4.14). Photocurrents from the photodetectors Det1 and Det2 are subtracted to yield the photocurrent $i(t) \propto \langle \hat{S}_y^{out}(t) \rangle \propto \langle \hat{J}_x(t) \rangle$, where $\langle . \rangle$ at refers to the mean value, which is then fed to a lock-in amplifier and then the MORS signal can be read out. In the figure we have that BS stands for beam splitter, PBS stands for polarizing beam splitter, HWP stands for half-wave plate, and $\mathbf{B}_{static}$ and $\mathbf{B}_{RF}$ are respectively the static magnetic field pointing along the z-axis and a radio frequency (RF) magnetic field oscillating on the x-axis, that the Cesium-133 atoms in the microcell are subject to. The mircocell is placed inside a magnetic shield described in section 3.3.

The MORS measurement results for F = 4 using the microcell G2 are seen in figure 14. Figure 14 (a) displays a case, where the pump laser is blocked; here we see that eight peaks are visible, which indicates that the atoms are distributed among all nine $m_F -$ levels. Figure 14 (b) displays a case, where the pump laser becomes unblocked; here we see that only one peak is visible and it is almost at the same position in frequency as the first peak in figure 14 (a), which indicates that the atoms are in the energy level $m_F = 4$. In figure 14 (a) we have that $p = 0.55$, which indicates an average polarization of the Cesium-133 atomic ensemble total angular momentum vector operator $\hat{\mathbf{J}}(t)$ along the z-axis (the quantization-axis in this experiment); and in figure 14 (b) we have that $p = 0.96$, which indicates a strong polarization of $\hat{\mathbf{J}}(t)$ along the z-axis. The MORS measurements presented in this section thus show us that it is possible for us to put the majority of the atoms in the microchannel into the coherent spin state $|4,4>$ such that κ^2 becomes greatly increased.

Note that during the MORS measurement the repump laser is always on, because we wish to draw the atoms out from the energy level $6^2S_{1/2}$, F = 3; and also note that in the MORS measurements we need to have $\Gamma_{m_F+1,m_F} < \omega_{QZ}$ in order to clearly resolve the peaks.

Now, since $\Gamma_{4,3} = \left(\pi T_{2,4\to3}\right)^{-1} = (\pi T_2)^{-1}$, where the last equality holds if $\hat{\mathbf{J}}(t)$ is well-polarized along the quantization-axis, we know that we can extract *the* transverse spin-coherence time T_2 of the Cesium-133 atoms from the MORS measurements, when $\hat{\mathbf{J}}(t)$ is well-polarized along the quantization-axis. In figures 15 (a), (b) and (c) we can see how the inverse of T_2 varies for different Larmor frequencies, RF magnetic field $\mathbf{B}_{RF}$ powers and probe light powers, respectively. The data seen in these figures was obtained using the microcell G2. We see that using a higher probe light

power will decrease T_2; the explanation to that is the same as it is for the T_1 measurements seen in section 3.2.3: for higher probe light power there is a higher chance of the depumping of the Cesium-133 atoms from $|4,4>$, because of the power broadening. Assuming that we may fit a linear curve to the data points in figure 15 (c), we can extract T_2 for the microcell G2, when there is no probe light; in such a case we obtain $T_2 \sim 1.72$ ms. As understood from eqs. (3.2.4.10.a-b), the longer T_2 is, the longer time the atoms stay in the coherent spin state $|4,4>$.

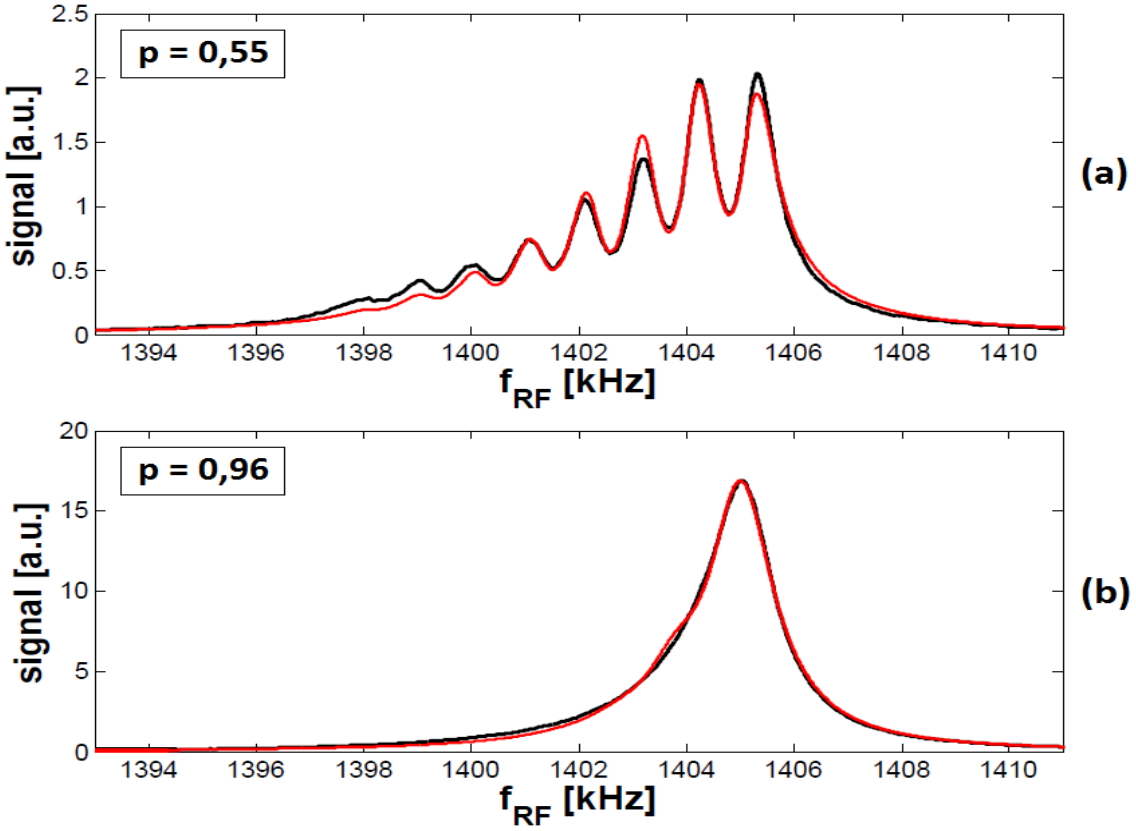

Figure 14. Experimentally obtained graphs, seen as black lines, showing the magneto-optical resonance signal (MORS), in cases where (a) the pump laser is blocked, and (b) the pump laser becomes unblocked. In both cases the repump laser is on. f_{RF} is the frequency of the RF magnetic field. The red lines are the fits to the experimentally obtained graphs. The fits are used to find the polarization parameter p defined in eq. (3.2.4.12). In the legend seen in (a) we see that $p = 0.55$; and in the legend seen in (b) we see that $p = 0.96$. The fitting in (a) is seen to be of not a good quality, and since the right-most peak is higher and also the third peak from the right is lower than the fit proposes, the value for p in the case of (a) may be slightly larger than $p = 0.55$. Note in the figures how the height of the peak in (b) is about nine times bigger than that of the right-most peak in (a).

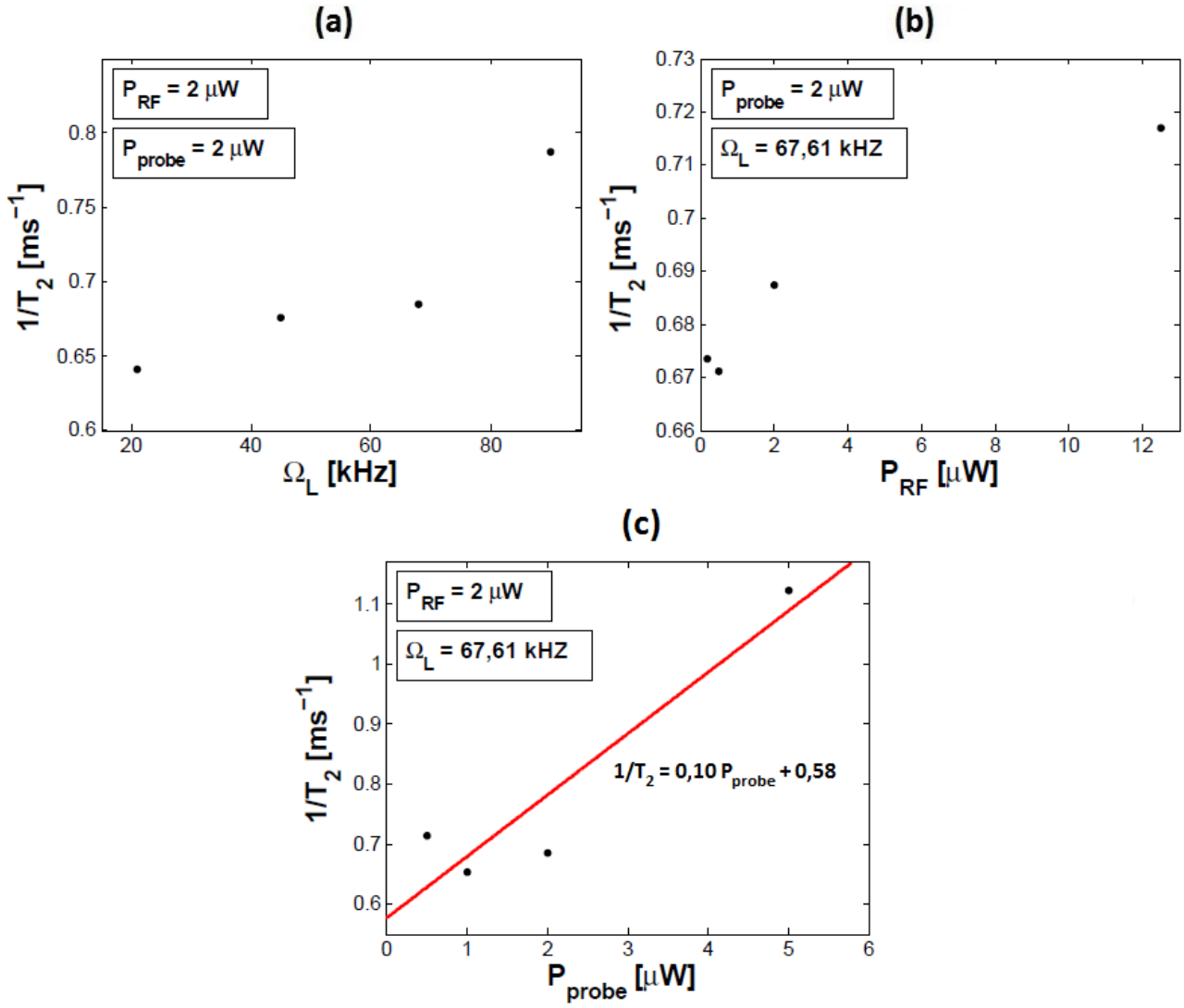

Figure 15. Experimentally obtained data points, seen as black dots, showing how the inverse of the transverse spin-coherence time T_2 varies for different (a) Larmor frequencies Ω_L, (b) radio frequency (RF) magnetic field $\mathbf{B}_{RF}$ powers P_{RF}, and (c) probe light powers P_{probe}. The measurements were performed using the microcell G2. The fixed parameters used in the different measurements are seen in the legends of the figures. Curve fitting is only performed in (c). Assuming that we may fit a linear curve to the data points in (c), seen as a red line, with the fit being $1/T_2 = 0.10P_{probe} + 0.58$, we can extract T_2 for the microcell G2, when there is no probe light; in such a case we obtain $T_2 \sim 1.72$ ms.

3.3 Shielding from stray magnetic fields and generating useful magnetic fields

In highly sensitive experiments such as the MORS experiment described in section 3.2.4, and the atom-membrane entanglement experiment described in chapter 4, we do not wish the Cesium-133 atoms in the microchannel of a microcell to be exposed to stray magnetic fields from the outside, because in such a case the optical pumping becomes compromised. Note that in the Faraday angle experiment described in section 3.2.3, the atoms should not be exposed to stray magnetic fields either; since it was done the other way around, it might've been one of the reasons why the Faraday angle $\theta_F(t = 0)$ was not constant with respect to probe light power, as seen in figure 12 (a).

In the MORS experiment and the atom-membrane entanglement experiment we shield the atoms from stray magnetic fields by placing the microcell inside cylinders as the one seen in figure 16; this cylinder together with endcaps attached to its ends acts as a magnetic shield. When making the shields one keeps in mind that magnetic shields do not really block magnetic fields but rather alter the path that magnetic fields take. The materials that magnetic shields should be made of have high magnetic permeability; this allows magnetic shields to conduct magnetic fields better than e.g. air such that magnetic fields will prefer to travel inside of the layers of magnetic shields rather than air. We see that magnetic shields that we use are of cylindrical shape and they are multilayered with the different layers being spaced. The reason for their cylindrical shape is because magnetic field lines resist to make sharp turns and cylindrical shape alters the path of the stray magnetic fields entering from the side such that it becomes harder for these fields to penetrate through; note that a spherical magnetic shield is of course the best option in our experiments, because stray magnetic fields may enter from all the sides of the shield. The reason why our magnetic shields are multilayered is because the stronger the stray magnetic field, the easier it is for this field to penetrate through; and the reason why the different layers are spaced is because the magnetic field lines in the gaps between the layers do not follow straight lines, and so the cost of the shields is reduced, because otherwise the thickness of the layers has to increased. Now, the outermost layer in the shields that we use is made out of iron and the remaining three layers are made out of mu-metal, which is a nickel-iron alloy. All the layers high have magnetic permeability with iron having a larger magnetic permeability than mu-metal ($2{,}5 \cdot 10^{-1}\mathrm{H/m}$ versus $2{,}5 \cdot 10^{-2}\mathrm{H/m}$, respectively [34]); this is the reason why the outermost layer is made out of iron.

Note that one strategically places holes in the magnetic shields that we use to allow us to position the microcell into the shield and enable laser-beam access.

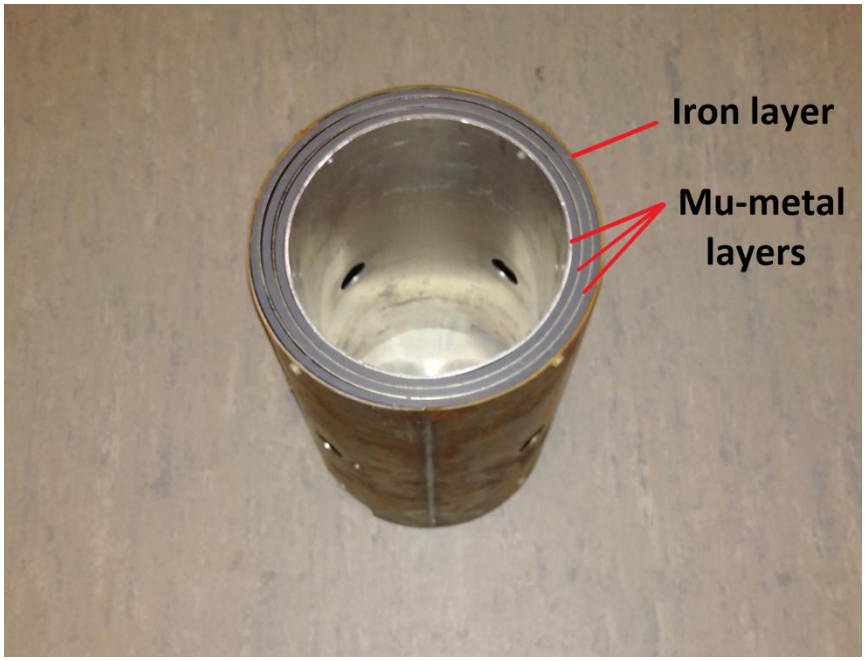

Figure 16. A multilayered cylinder which is placed around a microcell. This cylinder together with endcaps (not shown in the figure) attached to its ends acts as a magnetic shield that protects the microcell from stray magnetic fields from the outside. One strategically places holes in the magnetic shield to allow us to position the microcell into the shield and enable laser-beam access.

Inside the magnetic shield we place a wire-coil system. This wire-coil system subjects the Cesium-133 atoms to a static magnetic field that homogeneously points along the direction of the longitudinal-axis of the magnetic shield. This is exactly what we need, because the microcell is placed inside the magnetic shield such that the microchannel points along the radial direction of the magnetic shield. Note that if the magnetic field is of different strength in the region, where the microcell is placed, and in that region it is not be homogeneously pointing along the same direction, then according to eq. (3.2.4.11) *the* transverse spin-coherence time T_2 of the Cesium-133 atoms will decrease; this is true because the cause for the decay rate Γ_{com} includes the fact that the different atoms in the microchannel may be subject to a different magnetic field, as mentioned in section 3.2.3.

The schematic for the wire-coil system is seen in figure 17. The wire-coil system is wound on an aluminum cylinder, and it consists of four different wire-coil subsystems. One of the wire-coil subsystems is wound around six equally spaced aluminum rings placed on the aluminum cylinder. This wire-coil subsystem creates a magnetic field that nearly homogeneously points along the longitudinal-axis of the magnetic shield. To compensate for the inhomogeneities along the longitudinal direction, two more wire-coil subsystems are wound around the aluminum rings: one of them is a Helmholtz wire-coil subsystem and another one is an anti-Helmholtz wire-coil subsystem. To compensate for the inhomogeneities along the radial direction one winds double-saddle wire-coil subsystem; this wire-coil subsystem consists of eight 120° circular arcs wound on the aluminum cylinder beneath the aluminum rings. When all of the wire-coil subsystems are in use, one can in the region, where the microcell resides, create a nearly static magnetic field.

In order to produce a time-varying radio frequency (RF) magnetic field in the radial direction, one uses Helmholtz wire-coil system wound on a plastic spool that is placed inside the aluminum cylinder.

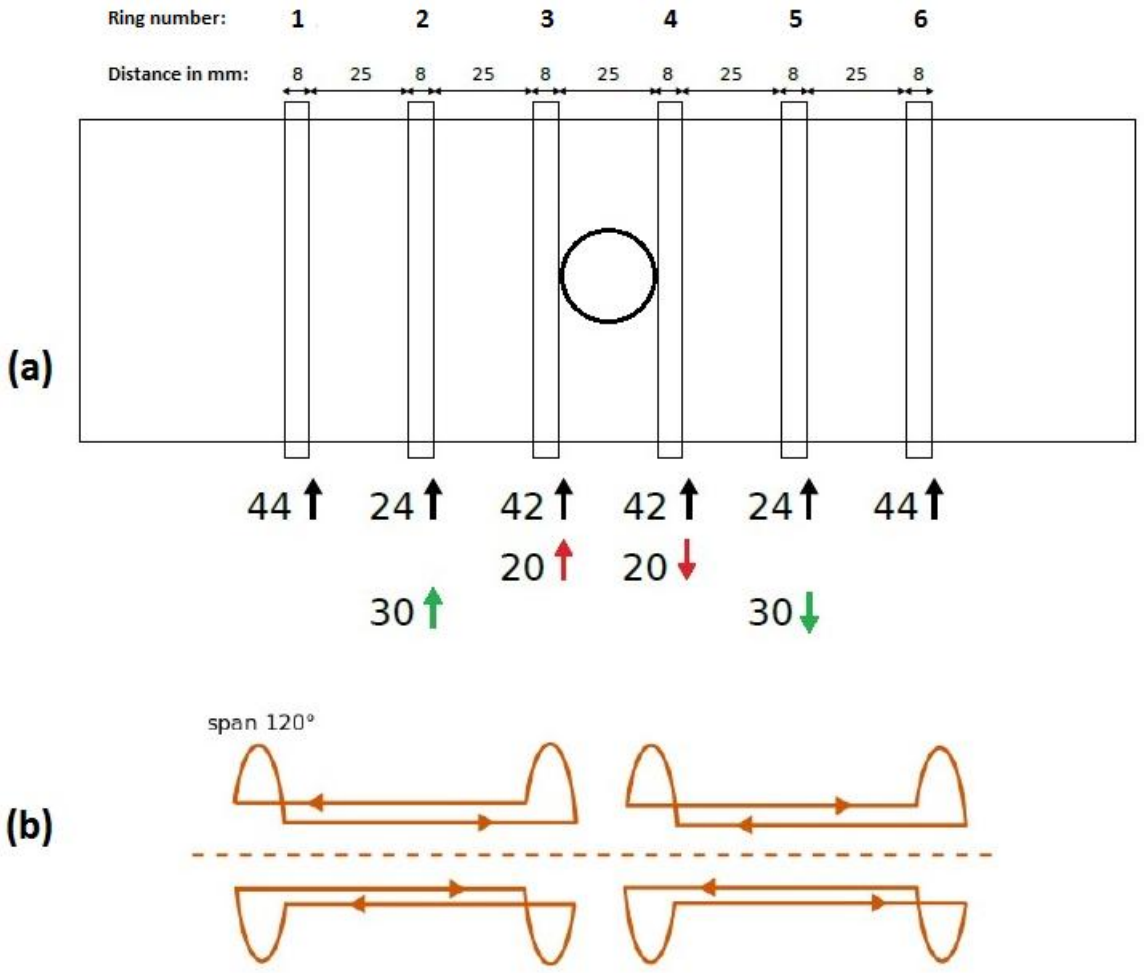

Figure 17. (a) and (b) Schematics for the wire-coil system used for subjecting the Cesium-133 atoms to a static magnetic field that homogeneously points along the longitudinal-axis of the magnetic shield. In (a): the wire-coil subsystem wound around the rings at positions 1-6 creates a magnetic field that nearly homogeneously points along the longitudinal-axis, and the wire-coil subsystems wound around the rings at positions 3 and 4 (Helmholtz wire-coil subsystem) and positions 2 and 5 (anti-Helmholtz wire-coil subsystem) compensate for the inhomogeneities along the longitudinal direction; the number of windings needed for each wire-coil subsystem and the direction of the windings is shown in the figure. In (b): the double-saddle wire-coil subsystem concentric with the wire-coil subsystems seen in (a) compensates for the inhomogeneities along the radial direction. The schematics for the wire-coil system are adapted from [21].

In figures 18 (a) and (b) we can see experimentally obtained data showing how the magnetic field strength varies in the radial direction of the magnetic shield, in the region, where the microcell resides, for respectively the wire-coil subsystem wound around the six equally spaced aluminum rings and the double-saddle wire-coil subsystem; and in figure 18 (c) we can see experimentally obtained data showing how the magnetic field strength varies in the radial direction of the magnetic shield, in that same region, when both of these wire-coil subsystems are in use. According to figure 8 (a), the microchannel of the microcell is 10 mm long, so if the microcell would be positioned around the center of the magnetic shield, then the region, where the microchannel would reside, would be $[-5; 5]$ mm. Note, however, that our microcells are positioned by translational mounts that can move the microcells along all three orthogonal axes, such that good light transmission through the microchannel could be achieved; ergo the measurements are performed in a larger

region $[-9; 9]$ mm. Note that the transverse cross-section of the microcell is very small according to figure 8 (a), and the microcells are usually translated very little along the directions that are different from the radial direction, and so it is not necessary to perform measurements along the remaining two orthogonal axes in order to understand how the strength of the magnetic field varies in the region, where the mircrocell resides. By changing the size of the current that flows through a given wire-coil subsystem, the given wire-coil subsystem will produce a magnetic field of different strength, and so it becomes important to know which current settings to use such that a nearly static magnetic field in the region, where the microcell resides, could be created. Using the current settings seen in figure 18 (c), we thus see from figure 18 (c) that when both of these wire-coil subsystems are in use, we can in the region, where the microcell resides, create a nearly static magnetic field.

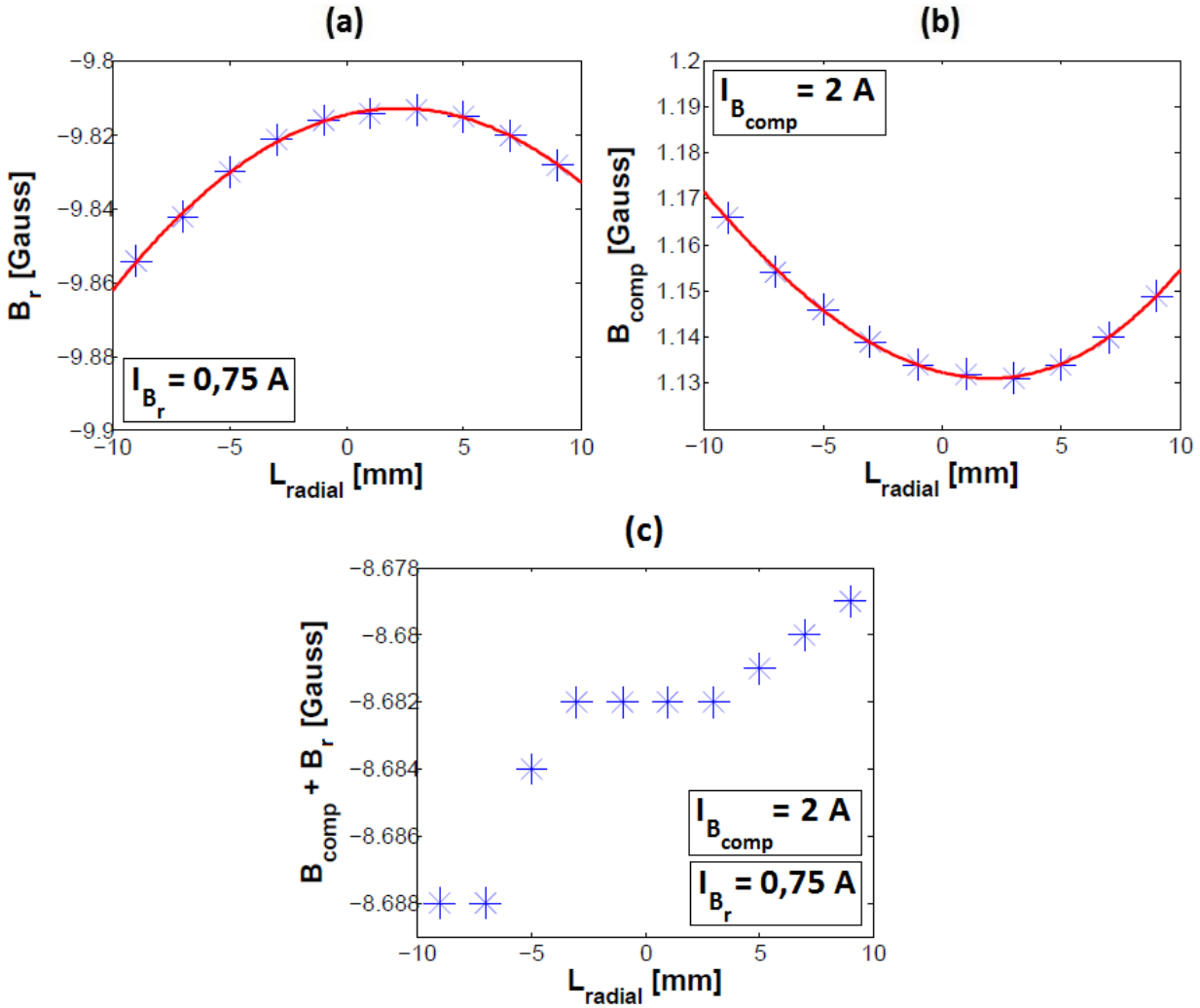

Figure 18. Experimentally obtained data points, seen as blue stars, showing how the magnetic field strengths (a) B_r, (b) B_{comp}, (c) $B_{comp} + B_r$ vary in the radial direction of the magnetic shield, in the region, where the microcell resides. Here $\mathbf{B}_r$ is the magnetic field produced by the wire-coil subsystem wound around the six equally spaced aluminum rings seen in figure 17 (a), and $\mathbf{B}_{comp}$ is the magnetic field produced by the double-saddle wire-coil subsystem seen in figure 17 (b). $L_{radial} = 0$ mm denotes the position of the center of the magnetic shield, and $L_{radial} > 0$ mm and $L_{radial} < 0$ mm denote the positions away from the center in the opposite directions. In the legends of the figures we can see that the particular currents that were used for the generation of respectively $\mathbf{B}_r$ and

$\mathbf{B}_{\mathrm{comp}}$ were $I_{B_r} = 0.75$ A and $I_{B_{comp}} = 2$ A. Quadratic curve fitting is performed in (a) and (b); the fits are seen as red lines. The experimentally obtained data points are seen to fit nicely with the fit.

3.4 The optomechanical system

The optomechanical system used in the atom-membrane entanglement experiment described in chapter 4 is contained inside a copper structure that can been seen in figure 19 (a). The optomechanical system consists of a semi-monolithic, high-finesse cavity that can be operated at cryogenic temperatures and a high-Q silicon nitride (SiN) nanomechanical membrane resonator that is shielded from the environment by a phononic crystal structure; a closer view of the nanomechanical membrane resonator can be seen in figure 19 (b). The nanomechanical membrane resonator is specially designed by our group. The nanomechanical membrane resonator can transmit laser light and therefore splits the cavity into two separate Fabry-Perot type cavities that are similar to the one seen in figure 2; the situation is depicted in figure 19 (c). Note in figure 19 (c) that the transmitted laser light field with the complex amplitude α_{trans} is picked up by the photodetector Det5 seen in figure 20, which shows a diagrammatic representation of the experimental setup used for the atom-membrane experiment.

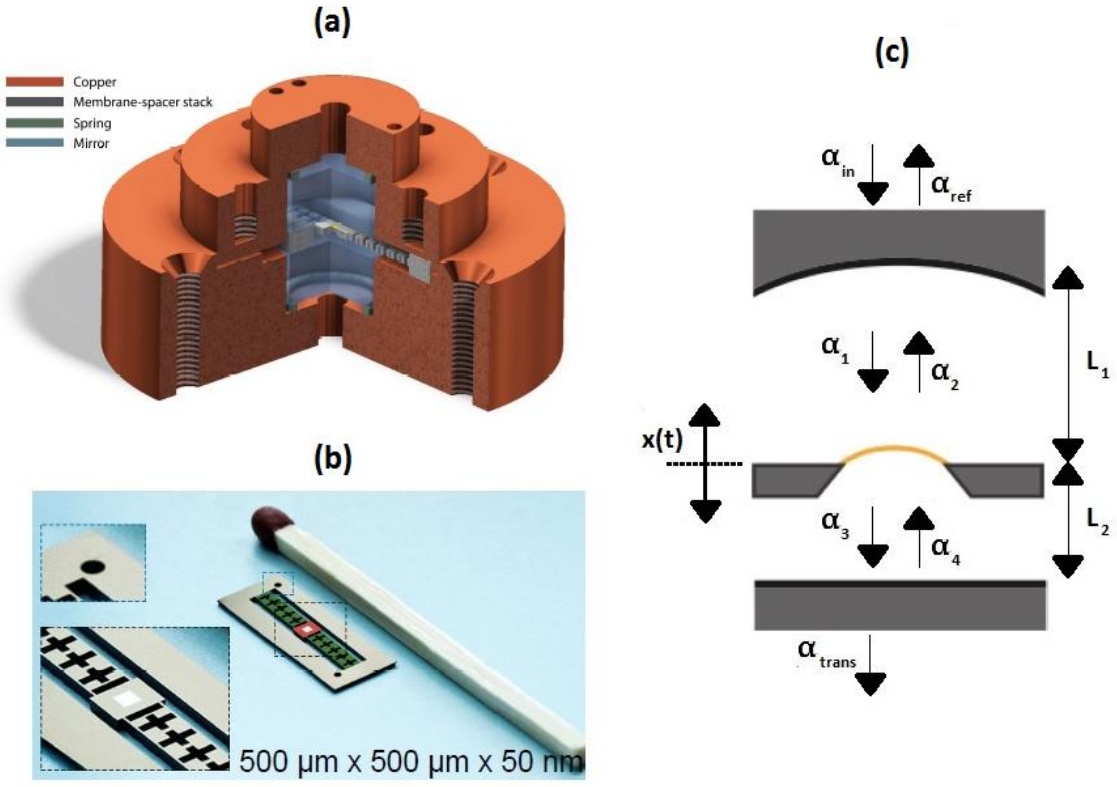

Figure 19. (a) An artist's impression of the optomechanical system used in our group's Cesium-133 atomic ensemble-nanomechanical membrane resonator interfacing experimental setup. The optomechanical system is contained inside a copper structure. The silicon nitride (SiN) nanomechanical membrane resonator chip is stacked with two silicon spacers on both sides thus ensuring that the chip is firmly clamped between the two mirrors. The metallic springs ensure parallelity between the mirrors and are the reason why the cavity is semi-monolithic. (b) Photos of the silicon nitride (SiN) nanomechanical membrane resonator chip. It consists of a silicon nitride membrane resonator (white square), a silicon frame (highlighted in red), and a phononic crystal structure (highlighted in green). The phononic crystal structure shields the membrane resonator from the environment. As indicated by the

figure, the membrane resonator is 500 μm wide, 500 μm long and 50 nm thick. (c) A diagrammatic representation of the optomechanical system seen in (a). As understood here, the copper structure allows a laser beam to enter from one end and to exit from another end of the optomechanical system. One can see that the membrane resonator (highlighted in yellow) can transmit laser light and therefore splits the cavity into two separate Fabry-Perot type cavities that are similar to the one seen in figure 2. The complex amplitudes α of the different laser light fields are shown in the figure. The output mirror has much higher reflectivity than the input mirror, and so the light entering the cavity has much higher probability to be reflected out of the cavity than to be transmitted. The figures are adapted from [9].

The big focus of this thesis is the atomic part of the atom-membrane entanglement experiment, and for that reason the experiments characterizing our optomechanical system are not included in this thesis. The interested reader can find the experiments characterizing our optomechanical system in e.g. [9, 10]. In [9] it is reported that we have achieved the cavity finesse of $\sim 5.6 \cdot 10^4$ and that the nanomechanical membrane resonator used in the experiments described in [9] has a Q-factor of $\sim 6 \cdot 10^6$. In [9] it is also reported that we are capable of cooling the membrane resonator to $T = 3$ mK, which gives the probability of 4% for the membrane resonator to be in the ground state. The membrane resonator that we use in our atom-membrane entanglement experiment is designed such that it would show significant response at frequencies around $\Omega_m = 610$ kHz. Using the formula for the mean thermal occupation of the membrane resonator in thermal equilibrium at temperature T, $\bar{n}_{th} \equiv \frac{k_B T}{2\pi\hbar\Omega_m}$, seen in chapter 2, we see that for $T = 3$ mK and $\Omega_m = 610$ kHz the initial thermal occupation $\bar{n}_{th,i}$, which we now set to be equal to $\bar{n}_{th}$, becomes $\bar{n}_{th,i} \approx 103$, where $k_B = 1.38 \cdot 10^{-23} J \cdot K^{-1}$ and $\hbar = 1.05 \cdot 10^{-34} J \cdot s$ are used.

As understood from section 2.2, due to the thermalization decay of the membrane resonator the practical requirement for the time period $t_1 \approx \tau$ of the entanglement protocol becomes $\tau \ll \frac{1}{\eta_m \bar{n}_{th}} = \frac{Q_m \hbar}{k_B T}$. Using the reported values $Q_m = 6 \cdot 10^6$ and $T = 3$ mK we see that in such a case we would need to perform the measurements much faster than 15 ms.

3.5 The atom-light coupling strength for the atom-membrane entanglement experiment

In this section I will express $\kappa^2 \equiv \frac{a}{2} S_x J_z \tau$, defined in section 1.4.5, in terms of parameters that are convenient from the point of view of our atom-membrane entanglement experiment.

Observing eq. (3.2.3.1) for the Faraday angle $\theta_F \equiv \theta_F(t)$, and expressing S_x as $S_x = -\frac{P_{probe}\lambda_{D2}}{4\pi\hbar c}$, where P_{probe} is the probe light power, and making the replacement $A \to A_{eff}$ in the definition of $a \equiv -\frac{\xi\lambda_{D2}^2}{16\pi A \Delta_5}$, where $A_{eff} < A$ is the effective transverse cross-sectional area of the probe laser beam, which we use, because as seen from section 3.2.1 the probe laser beam doesn't fill the whole microchannel, we obtain

$$\kappa^2 = \frac{\xi\lambda_{D2}^3}{32\pi^2 A_{eff}|\Delta_5|\hbar c} \cdot P_{probe} \cdot \theta_F \cdot \tau =$$

$$= \frac{56.4}{A_{eff}[cm^2]\cdot|\Delta_5|[MHz]} \cdot P_{probe}[mW] \cdot \theta_F[deg] \cdot \tau[ms] \quad , \qquad (3.5.1)$$

where $\xi = 2\pi \cdot 5.22$ MHz and $\lambda_{D2} = 852$ nm are used.

By making use of experimental data and parameters that characterize our atom-membrane experiment let us now from eq. (3.5.1) estimate what values for κ^2 we can expect to obtain in the case of our atom-membrane interfacing experimental setup. Now:

1. observing figure 8 (b) we see that $A = \pi \cdot (150 \cdot 10^{-4}\ \text{cm})^2$, and by assuming that we may set $A_{eff} = \frac{A}{2}$ we obtain $A_{eff} = \pi \cdot 1.125 \cdot 10^{-4}\ \text{cm}^2$.

2. observing section 3.1.1 we see that $|\Delta_5| = 2\pi \cdot 1600$ MHz.

3. observing section 3.2.3 we make use of the experimentally obtained value for $\theta_F(t = 0)$, being $\theta_F(0) = 1.38\ °$, and equate it with θ_F in eq. (3.5.1) such that $\theta_F = 1.38\ °$.

4. observing section 4.2 we see that during the measurements performed using our atom-membrane interfacing experimental setup the atoms were probed with laser powers being $P_{probe,a} = 0.120\ \text{mW}, 0.122\ \text{mW}, 0.600\ \text{mW}$; such that in the present case we set $P_{probe} = P_{probe,a}$. We also see that during these measurements $\tau = 0.1$ ms.

Plugging now the values seen above into eq. (3.5.1) we see that

$$\kappa^2 = 0.263, 0.267, 1.314 \quad . \qquad (3.5.2)$$

Assuming that the estimates for κ^2 seen in eq. (3.5.2) are correct, we understand that in the case of our atom-membrane interfacing experimental setup we can obtain moderate values of $\kappa^2 \gtrsim 0.25$ noted in the atom-membrane entanglement proposal [12].

Chapter 4: Experimental work towards entanglement genration between Cesium-133 atomic ensemble and nanomechanical membrane resonator

In this chapter I present the experimental setup that we use for working towards entanglement generation between Cesium-133 atomic ensemble and nanomechanical membrane resonator, and I demonstrate how this setup can allow us to satisfy the entanglement protocol described in chapter 2. I also present measurements done using this setup.

4.1 Atom-membrane interfacing experimental setup

In figure 20 we can see a diagrammatic representation of our group's owned experimental setup that, via laser light, interfaces a Cesium-133 atomic ensemble contained inside our specially designed microcells described in section 3.2 and our specially designed nanomechanical membrane resonator that is part of a cryogenic optomechanical system described in section 3.4. This setup is an actual realization of a schematic of the setup seen in figure 3.

We experimentally realize the filter seen in figure 3 by building a Mach-Zehnder-type interferometer. A diagrammatic representation of the Mach-Zehnder interferometer that we build is enclosed in a dashed blue contour in figure 20. As explained in the text of figure 3, the filter's function is to convert the light that becomes polarization modulated by the Cesium-133 atoms into amplitude modulated light; and this is exactly what the interferometer does. Recall from chapter 2, that mathematically, the filter allows us to equate the pairs of the light operators $\hat{x}_L^{out}$ and $\hat{x}'^{in}_L$, and $\hat{p}_L^{out}$ and $\hat{p}'^{in}_L$ as $\hat{x}'^{in}_L = -\hat{x}_L^{out}$ and $\hat{p}'^{in}_L = -\hat{p}_L^{out}$ as seen in eqs. (2.1.10.a-b).

In order to see why our interferometer satisfies the role of the filter, and also why our atom-membrane interfacing experimental setup can allow us to satisfy the entanglement protocol described in chapter 2, let us now make use of Jones matrix calculus introduced in appendix D and thoroughly analyze the whole experimental setup. By making use of Jones matrix calculus, we will need to treat the probe laser light classically.

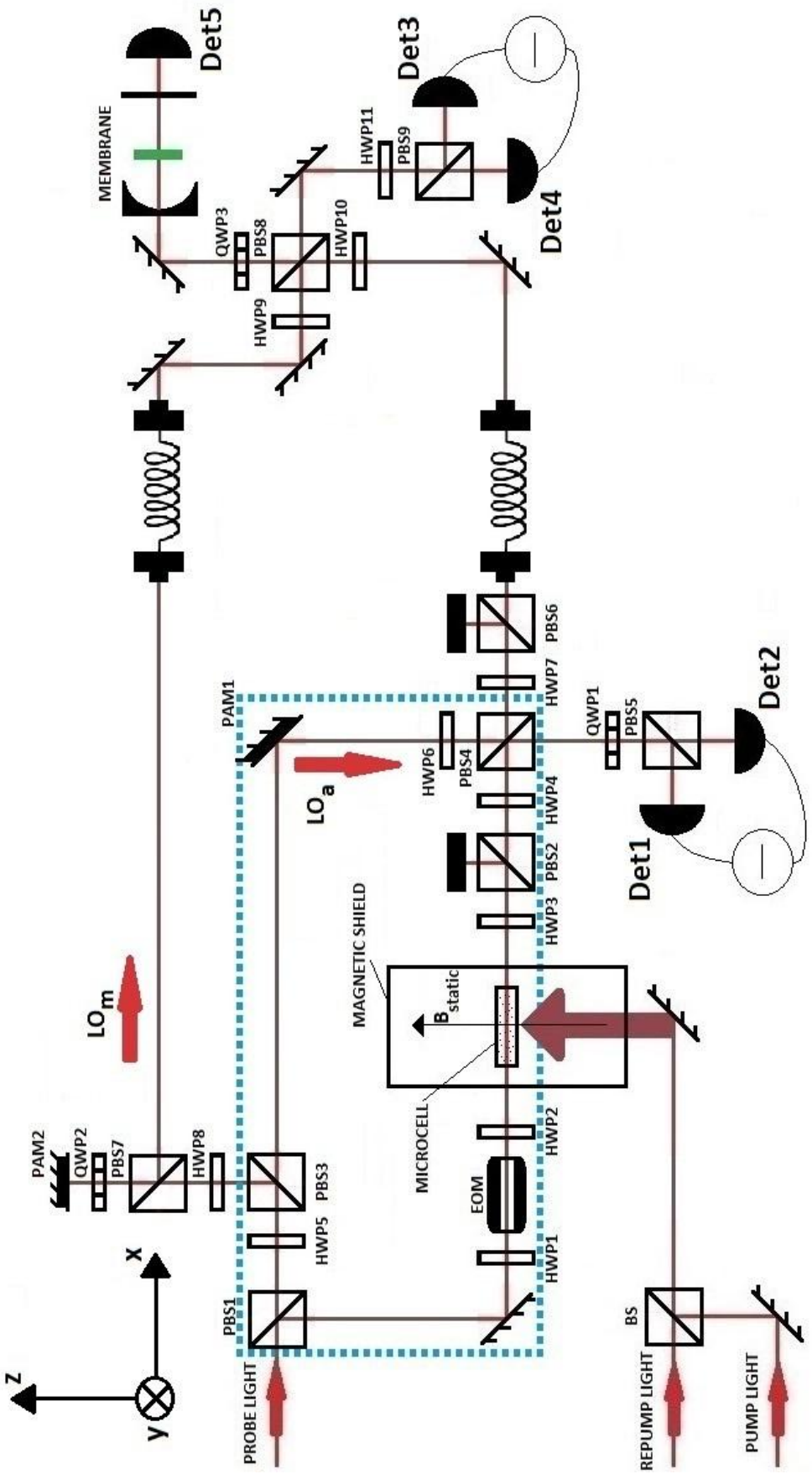
Det5
MEMBRANE
Det3
HWP11
PBS9
Det4
QWP3
PBS8
HWP10
HWP9
PAM1
PBS6
HWP7
QWP1
PBS5
Det2
HWP6
PBS4
HWP4
LO_a
Det1
PBS2
HWP3
MAGNETIC SHIELD
B_static
LO_m
MICROCELL
EOM
HWP2
PAM2
QWP2
PBS7
HWP8
PBS3
HWP5
HWP1
PBS1
BS
x
z
y
PROBE LIGHT
REPUMP LIGHT
PUMP LIGHT

Figure 20. A diagrammatic representation of our group's owned experimental setup that, via laser light, interfaces a Cesium-133 atomic ensemble contained inside our specially designed microcells described in section 3.2 and our specially designed nanomechanical membrane resonator that is part of a cryogenic optomechanical system described in section 3.4. Enclosed in a dashed blue contour is a Mach-Zehnder-type interferometer, which satisfies the role of the filter seen in figure 3. In the figure we have that BS stands for beam splitter, PBS stands for polarizing beam splitter, HWP stands for half-wave plate, QWP stands for quarter-wave plate, PAM stands for piezoelectric-actuated mirror, EOM stands for electro-optic modulator, Det1, Det2, Det3, Det4 and Det5 are photodetectors, $\mathbf{B}_{\text{static}}$ is the static magnetic field pointing along the z-axis that the Cesium-133 atoms in the microcell are subject to, and LO_a and LO_m are the local oscillators used for balanced homodyne detection realized by respectively Det1, Det2 and Det3, Det4. The mircocell is placed inside a magnetic shield described in section 3.3.

From eq. (D.1) we have that the Jones vector for the probe light before the polarizing beam splitter PBS1 in figure 20 is

$$\mathbf{V}_{\text{in}} \equiv \begin{bmatrix} \text{E}_\text{H} \\ \text{E}_\text{V} \end{bmatrix} = \begin{bmatrix} \text{E}_{0\text{H}} e^{\text{i}(\varphi_\text{H} - \omega_0 \text{t})} \\ \text{E}_{0\text{V}} e^{\text{i}(\varphi_\text{V} - \omega_0 \text{t})} \end{bmatrix} \quad , \tag{4.1.1}$$

where E_H and E_V are the (complex) horizontal and vertical polarization components, respectively, of the electric field $\mathbf{E}(\text{x}, \text{t}) = \mathbf{V}_{\text{in}} e^{\text{ikx}}$ of a monochromatic plane wave of light, which in the present case describes the probe laser light, which travels along the x-axis, where k is the angular wave number and ω_0 is the angular frequency of the probe laser light with $\text{k} = \omega_0/\text{c}$, and $\text{E}_{0\text{H}}$ and $\text{E}_{0\text{V}}$ are the amplitudes of respectively E_H and E_V with φ_H and φ_V being the respective phases.

The Jones matrices that we will use in the present case are: $\bar{\bar{\mathbf{M}}}_\text{R}(\theta)$, $\bar{\bar{\mathbf{M}}}_\text{RWP}(\varphi, \theta)$, $\bar{\bar{\mathbf{M}}}_\text{LPOL}(\text{p}_\text{H}, \text{p}_\text{V})$ and $\bar{\bar{\mathbf{M}}}_\text{PAM}\big(\varphi_\text{H} \to \varphi_{\text{H},*}(\text{t}), \varphi_\text{V} \to \varphi_{\text{V},*}(\text{t})\big)$, which respectively are the Jones matrix for a rotator defined in eq. (D.3.a), the Jones matrix for a rotated wave plate defined in eq. (D.3.b), the Jones matrix for a perfect linear polarizer defined in eq. (D.3.c) and the Jones matrix for a piezoelectric-actuated mirror defined in eq. (D.3.d). Here θ is the angle of the fast axis of a wave plate with respect to the horizontal axis; $\varphi \equiv \varphi_\text{H} - \varphi_\text{V}$; $\text{p}_\text{H}, \text{p}_\text{V} = 0$ or 1; and $\bar{\bar{\mathbf{M}}}_\text{PAM}\big(\varphi_\text{H} \to \varphi_{\text{H},*}(\text{t}), \varphi_\text{V} \to \varphi_{\text{V},*}(\text{t})\big)$ transforms the phases φ_H and φ_V in the Jones vector $\mathbf{V}_{\text{in}}$ in eq. (4.1.1) into time dependent phases $\varphi_{\text{H},*}(\text{t})$ and $\varphi_{\text{V},*}(\text{t})$.

Note that in appendix E we can see how the Jones matrices for the different optical elements seen in figure 20 are defined using the Jones matrices given by eqs. (D.3.a-d), and also how they look like in a completely written out form.

Observing figure 20 we now find the Jones vector for the light exiting the lower output port of the polarizing beam splitter PBS1:

$$\mathbf{V}_{\text{PBS1,lp}} = \bar{\bar{\mathbf{M}}}_{\text{PBS1,r}} \mathbf{V}_{\text{in}} + \bar{\bar{\mathbf{M}}}_{\text{PBS1,tr}} \mathbf{V}_{\text{noise}} = \begin{bmatrix} \hat{\alpha}_\text{n} \cos(\Omega_\text{L} \text{t})\, e^{\text{i}\varphi_\text{r}} \\ \text{E}_{0\text{V}} e^{\text{i}(\varphi_\text{V} - \omega_0 \text{t})} \end{bmatrix} \quad . \tag{4.1.2}$$

The first term of the sum in eq. (4.1.2) and the second term of the sum in eq. (4.1.2) deal with respectively the probe light entering the right input port of the PBS1 and the fluctuating vacuum field entering the upper input port of the PBS1. The Jones vector for the fluctuating vacuum field is

$\mathbf{V}_{\text{noise}} = \begin{bmatrix} \hat{\alpha}_n \cos(\Omega_L t)\, e^{i\varphi_r} \\ 0 \end{bmatrix}$, where $\hat{\alpha}_n$ is an operator representing the fluctuating vacuum field, Ω_L is the Larmor frequency of the Cesium-133 atoms, which in the experimental case is 610 kHz, and φ_r is the phase of $\hat{\alpha}_n$. The reason why $\mathbf{V}_{\text{noise}}$ is included, is because the PBS1 has an unused port, through which fluctuating vacuum field can enter. In figure 20 we see that most of the PBSs have unused ports; however, for simplicity we shall assume that vacuum fluctuations only enter the PBS1. From $\mathbf{V}_{\text{noise}}$ we see that the fluctuating vacuum field is of horizontal polarization; this is, however, only an assumption that allows us to simplify the forthcoming calculations. Now, observing the Cesium-133 atom Hamiltonian $\hat{H}_{\text{atoms}}$ in eq. (2.1.4.a) and the membrane resonator Hamiltonian $\hat{H}_{\text{membrane}}$ in eq. (2.1.4.b), we see that the atoms will show significant response at the Larmor frequency Ω_L and the membrane resonator will show a significant response at the angular frequency Ω_m; this is true, because Ω_L and Ω_m denote the resonance frequencies of the two oscillators, and oscillators are known to show significant response at their resonance frequencies. Observing section 3.4 we see that our membrane resonator is designed such that it would show significant response at frequencies around $\Omega_L = 610$ kHz such that we can set $\Omega_m = \Omega_L$. Because the fluctuating vacuum field propagates through the atoms and eventually enters the cavity, where the membrane resonator resides, and both the atoms and the membrane resonator show significant response at Ω_L, one multiplies $\hat{\alpha}_n e^{i\varphi_r}$ in $\mathbf{V}_{\text{noise}}$ by a forcing term $\cos(\Omega_L t)$**.** Now, since the polarizing beam splitters used in our experiments transmit the horizontally-polarized component of the light and reflect the vertically-polarized component of the light, and since we need to find the Jones vector exiting the lower output port of the PBS1, we multiply $\mathbf{V}_{\text{in}}$ and $\mathbf{V}_{\text{noise}}$ by respectively the Jones matrix for the PBS1 reflecting the light and the Jones matrix for the PBS1 transmitting the light.

Observing figure 20 we now find the Jones vector for the light entering the microcell:

$$\mathbf{V}_{\text{microcell,in}} = \bar{\bar{\mathbf{M}}}_{\text{tot}_a} \mathbf{V}_{\text{PBS1,lp}} \approx \begin{bmatrix} E_{y,a}^{\text{in}} \\ E_{z,a}^{\text{in}} \end{bmatrix} \quad , \tag{4.1.3}$$

where $\bar{\bar{\mathbf{M}}}_{\text{tot}_a} \equiv \bar{\bar{\mathbf{M}}}_{\text{HWP2}} \bar{\bar{\mathbf{M}}}_{\text{EOM}} \bar{\bar{\mathbf{M}}}_{\text{HWP1}}$, and

$$E_{y,a}^{\text{in}} \equiv \hat{\alpha}_n \cos(\Omega_L t)\, e^{i\varphi_r} + \left(\frac{i}{2} \beta_1 \cos\left(\Omega_{\beta_1} t\right) + \frac{i}{2} \beta_2 \cos(\Omega_L t) \right) E_{0V} e^{i(\varphi_V - \omega_0 t)} \quad ,$$

$$E_{z,a}^{\text{in}} \equiv \left(1 - \frac{i}{2} \beta_1 \cos\left(\Omega_{\beta_1} t\right) - \frac{i}{2} \beta_2 \cos(\Omega_L t) \right) E_{0V} e^{i\left(\varphi_V - \omega_0 t + \frac{\pi}{2}\right)} \quad .$$

Eq. (4.1.3) deals with the light exiting the lower output port of the PBS1, i.e. the light described the Jones vector $\mathbf{V}_{\text{PBS1,lp}}$ in eq. (4.1.2). Here the light first travels in succession through the HWP1, the EOM and the HWP2. It is assumed that the effects of HWP1 and HWP2 can be neglected, and the collective effect on the polarization in this case can be described by the EOM. The EOM is assumed to behave as a $\frac{\pi}{4}$-rotated wave plate ($\theta = \frac{\pi}{4}$) with $\varphi = \beta_1 \cos\left(\Omega_{\beta_1} t\right) + \beta_2 \cos(\Omega_L t)$, where β_1 and β_2 are small amplitudes of sinusoidally varying voltages of frequencies Ω_{β_1} and Ω_L, respectively, that we apply to the EOM. Note that we make sure in the experiment that $\Omega_\beta \neq \Omega_L$; in particular, we set $\Omega_\beta = 400$ kHz. The sinusoidally varying voltages of amplitudes β_1 and β_2 are applied to the EOM,

because we here wish to create horizontally-polarized Ω_β-sidebands centered around the carrier angular frequency ω_0 and horizontally-polarized Ω_L-sidebands also centered around ω_0. The Ω_β-sidebands are later used for stabilizing the phases of the local oscillators LO_a and LO_m seen in figure 20. The Ω_β- and Ω_L-sidebands propagate through the atoms and eventually enter the cavity, where the membrane resonator resides. Note that it is intentional that the atoms and the membrane resonator are driven by both the relatively large Ω_L-sidebands in addition with the fluctuating vacuum field. The Ω_L-sidebands are added, because, as shown in section 4.2, these can help us to combat the mismatch between the atomic and the membrane resonator parameters, i.e. when $\kappa\sqrt{\frac{2}{\tau}} \neq g_{m,c}\sqrt{\frac{2}{\eta_c}}$. The idea in the end is not use the *classical* Ω_L-sidebands, and drive the Cesium-133 atoms and the membrane resonator with purely the fluctuating vacuum field; but until we do not come close to matching the atomic and the membrane resonator parameters, the Ω_L-sidebands stay added. Note that $E_{z,a}^{in}$ acquires an additional phase of $e^{i\frac{\pi}{2}} = i$; this is done, because in the present case we have that eqs. (1.4.5.2.a-c) hold, where it is assumed that the operators $\hat{a}_z(x,t) \rightarrow \langle \hat{a}_z(x,t)\rangle = i|\alpha_z(x,t)|$, $\hat{a}_z^\dagger(x,t) \rightarrow \langle \hat{a}_z^\dagger(x,t)\rangle = -i|\alpha_z(x,t)|$. Note as well that $\mathbf{V}_{\text{microcell,in}}$ in eq. (4.1.3) is an approximation, because the terms proportional to $\widehat{\alpha}_n\beta_1$ and $\widehat{\alpha}_n\beta_2$ are neglected, as these proportionality factors are much smaller than $\widehat{\alpha}_n$, β_1 and β_2.

Now, the light will propagate through the microcell, where it will interact with the atoms. The light's interaction with the atoms will transform the scaled Stokes operators $\hat{x}_L(z)$ and $\hat{p}_L(z)$ according to the input-output relations (2.1.8.a-b). In order to find the Jones vector for the light exiting the microcell, we need to know how to express the $\hat{x}_L(z)$ and $\hat{p}_L(z)$ in terms of the (complex) horizontal and vertical polarization components of the light seen in a Jones vector. Now, since $\hat{x}_L(z) \propto \hat{S}_z(t)$ and $\hat{p}_L(z) \propto \hat{S}_y(t)$, where $\hat{S}_y(t)$ and $\hat{S}_z(t)$ are the *regular* Stokes operators that satisfy eqs. (1.4.5.2.b-c), and since the classical Stokes operators may because of eqs. (1.4.5.2.b-c) be defined as $S_y \equiv \frac{1}{i2}\left(\overline{E}_{y,a}E_{z,a} - E_{y,a}\overline{E}_{z,a}\right)$ and $S_z \equiv \frac{1}{2}\left(\overline{E}_{y,a}E_{z,a} + E_{y,a}\overline{E}_{z,a}\right)$, where $E_{y,a}$ and $E_{z,a}$ are the horizontal and vertical polarization components of the light in a Jones vector for the light in the atom-light system, respectively, then in our case

$$\hat{x}_L(z) \rightarrow \frac{1}{\sqrt{2}}\left(\overline{E}_{y,a}E_{z,a} + E_{y,a}\overline{E}_{z,a}\right) \quad , \tag{4.1.4.a}$$

$$\hat{p}_L(z) \rightarrow \frac{1}{i\sqrt{2}}\left(\overline{E}_{y,a}E_{z,a} - E_{y,a}\overline{E}_{z,a}\right) \quad . \tag{4.1.4.b}$$

Note the similarities between $\hat{x}_L(z)$ and $\hat{p}_L(z)$ in eqs. (4.1.4.a-b) and the Stokes operators given by eqs. (1.4.5.1.c-d), when eqs. (1.4.5.2.a-c) are used.

Using eqs. (4.1.4.a-b), we have that the input-output relations (2.1.8.a-b) will in our case therefore read as

$$\left.\begin{aligned}\hat{x}_L^{out} &= -\hat{x}_L^{in} \\ \hat{p}_L^{out} &= -\hat{p}_L^{in} + K_{\hat{x}_a,\hat{p}_a}\end{aligned}\right\} <=>$$

$$\left(\overline{E}_{y,a}^{out}E_{z,a}^{out} + E_{y,a}^{out}\overline{E}_{z,a}^{out}\right) = -\left(\overline{E}_{y,a}^{in}E_{z,a}^{in} + E_{y,a}^{in}\overline{E}_{z,a}^{in}\right) \quad , \tag{4.1.5.a}$$

$$\frac{1}{i\sqrt{2}}\left(\overline{E}_{y,a}^{out}E_{z,a}^{out} - E_{y,a}^{out}\overline{E}_{z,a}^{out}\right) = \frac{-1}{i\sqrt{2}}\left(\overline{E}_{y,a}^{in}E_{z,a}^{in} - E_{y,a}^{in}\overline{E}_{z,a}^{in}\right) + K_{\hat{X}_a,\hat{P}_a} \quad , \tag{4.1.5.b}$$

where $E_{y,a}^{in}$ and $E_{z,a}^{in}$ are the horizontal and vertical polarization components of the light seen in the Jones vector for the light entering the microcell, i.e. $\mathbf{V}_{microcell,in}$ in eq. (4.1.3), $E_{y,a}^{out}$ and $E_{z,a}^{out}$ are the horizontal and vertical polarization components of the light seen in the Jones vector for the light exiting the microcell, and

$$K_{\hat{X}_a,\hat{P}_a} \equiv -\kappa\sqrt{\frac{2}{\tau}}\left(-\hat{P}_a^* \sin\left(\Omega_{L,n}t\right) + \hat{X}_a^* \cos\left(\Omega_{L,n}t\right)\right) \quad ,$$

where $\Omega_{L,n} \equiv -\Omega_L$ is the negative Larmor frequency, as defined in section 2.1.

Using eqs. (4.1.3) and (4.1.5.a-b) we have that $\hat{x}_L^{out}$ and $\hat{p}_L^{out}$ are

$$\hat{x}_L^{out} \approx \sqrt{2}E_{0V}\hat{\alpha}_n \cos(\Omega_L t) - \frac{E_{0V}^2}{\sqrt{2}}\beta_1 \cos\left(\Omega_{\beta_1}t\right) - \frac{E_{0V}^2}{\sqrt{2}}\beta_2 \cos(\Omega_L t) \quad , \tag{4.1.6.a}$$

$$\hat{p}_L^{out} \approx \sqrt{2}E_{0V}\hat{\alpha}_n \cos(\Omega_L t) + K_{\hat{X}_a,\hat{P}_a} \quad , \tag{4.1.6.b}$$

where approximation signs are used, because the terms proportional to $\hat{\alpha}_n\beta_1$, $\hat{\alpha}_n\beta_2$, β_1^2, β_2^2, $\beta_1\beta_2$ are neglected, as these proportionality factors are much smaller than $\hat{\alpha}_n$, β_1 and β_2.

Using eqs. (4.1.5.a-b) and (4.1.6.a-b) we thus obtain the Jones vector for the light exiting the microcell:

$$\mathbf{V}_{microcell,out} = \begin{bmatrix} E_{y,a}^{out} \\ E_{z,a}^{out} \end{bmatrix} = \begin{bmatrix} -K_{\hat{X}_a,\hat{P}_a}e^{i\left(\varphi_V - \omega_0 t + \frac{\pi}{2}\right)} - \tilde{E}_{y,a}^{in} \\ -K_{\hat{X}_a,\hat{P}_a}e^{i\left(\varphi_V - \omega_0 t + \frac{\pi}{2}\right)} - E_{z,a}^{in} \end{bmatrix} \quad , \tag{4.1.7}$$

where $\tilde{E}_{y,a}^{in}$ is $E_{y,a}^{in}$ with $\hat{\alpha}_n \to E_{0V}\hat{\alpha}_n$, and an added phase of $e^{i\frac{\pi}{2}} = i$. Note that $E_{y,a}^{out}$ and $E_{z,a}^{out}$ acquire phases of $e^{i\frac{\pi}{2}} = i$ for the same reason as $E_{z,a}^{in}$ does.

Observing figure 20 we now find:

1. The Jones vector for the light incident on the photodetector Det1:

$$\mathbf{V}_1 = \bar{\bar{\mathbf{M}}}_{tot1}\mathbf{V}_{microcell,out} + \bar{\bar{\mathbf{M}}}_{tot1}\mathbf{V}_{in} = \begin{bmatrix} 0 \\ \overline{K}_{k,a}E_{0H}e^{i\left(\varphi_{H,1}(t) - \omega_0 t + \frac{\pi}{2}\right)} + K_{k,a}E_{x,a}^{out} \end{bmatrix} \quad , \tag{4.1.8.a}$$

2. The Jones vector for the light incident on the photodetector Det2:

$$\mathbf{V}_2 = \bar{\bar{\mathbf{M}}}_{tot2}\mathbf{V}_{microcell,out} + \bar{\bar{\mathbf{M}}}_{tot2}\mathbf{V}_{in} = \begin{bmatrix} K_{k,a}E_{0H}e^{i\left(\varphi_{H,1}(t) - \omega_0 t + \frac{\pi}{2}\right)} + \overline{K}_{k,a}E_{x,a}^{out} \\ 0 \end{bmatrix} \quad . \tag{4.1.8.b}$$

In eqs. (4.1.8.a-b) we have $K_{k,a} \equiv \frac{\sqrt{2}}{4}(1-i)$, $\bar{\bar{\mathbf{M}}}_{tot1} \equiv \bar{\bar{\mathbf{M}}}_{PBS5,r}\bar{\bar{\mathbf{M}}}_{QWP1}\bar{\bar{\mathbf{M}}}_{PBS4,r}\bar{\bar{\mathbf{M}}}_{HWP4}\bar{\bar{\mathbf{M}}}_{PBS2,tr}\bar{\bar{\mathbf{M}}}_{HWP3}$, $\bar{\bar{\mathbf{M}}}_{tot1'} \equiv \bar{\bar{\mathbf{M}}}_{PBS5,r}\bar{\bar{\mathbf{M}}}_{QWP1}\bar{\bar{\mathbf{M}}}_{PBS4,tr}\bar{\bar{\mathbf{M}}}_{HWP6}\bar{\bar{\mathbf{M}}}_{PAM1}\bar{\bar{\mathbf{M}}}_{PBS3,tr}\bar{\bar{\mathbf{M}}}_{HWP5}\bar{\bar{\mathbf{M}}}_{PBS1,tr}$, and $\bar{\bar{\mathbf{M}}}_{tot2}$ and $\bar{\bar{\mathbf{M}}}_{tot2'}$ are respectively $\bar{\bar{\mathbf{M}}}_{tot1}$ and $\bar{\bar{\mathbf{M}}}_{tot1'}$ with $\bar{\bar{\mathbf{M}}}_{PBS5,r} \rightarrow \bar{\bar{\mathbf{M}}}_{PBS5,tr}$. Note that $\bar{K}_k$ is the complex conjugate of K_k.

The first terms of the sum in eqs. (4.1.8.a) and (4.1.8.b) deal with the light exiting the microcell. Here the light first travels in succession through the HWP3 and the PBS2. The HWP3 is assumed to behave as a non-rotated half-wave plate, which introduces the phase shift $\varphi = \pi$ between the horizontal and vertical components of the light. The PBS2 transmits the horizontally-polarized component of the light and reflects the vertically-polarized component of the light; the horizontally-polarized component is the one we are interested in, because it includes the fluctuating vacuum field, Ω_β-sidebands, the Ω_L-sidebands, and the *important* atomic signal expressed by $K_{\hat{X}_a,\hat{P}_a}$, while the vertically-polarized component includes all of these components except for the atomic signal. The horizontally-polarized component of the light then travels in succession through the HWP4 and the PBS4. The HWP4 is assumed to behave as a $\frac{\pi}{8}$-rotated half-wave plate, which will make the PBS4 to send equal amounts of the light into the part of the setup that includes Det1 and Det2 and also into the part of the setup that includes the membrane resonator; note that the rotation angle of $\frac{\pi}{8}$ is in the present case picked in order to simplify the calculations, as in reality we here wish to send a smaller amount of the atomic signal into the part of the setup that includes Det1 and Det2 and a larger amount of the atomic signal into the part of the setup that includes the membrane resonator. The light then travels in succession through the QWP1 and the PBS5. The QWP1 is assumed to behave as a $\frac{\pi}{4}$-rotated quarter-wave plate, which will make the PBS5 to send the light in equals amounts into the Det1 and also into the Det2, when the right output port of the PBS1 is blocked, such that the detection becomes *balanced*. Note as understood from appendix C and also from the calculations seen further below in this section we have that when both output ports of the PBS1 become unblocked, then Det1 and Det2 will in general detect different intensities; the physical explanation for that is the light interference phenomenon.

The second terms of the sum in eqs. (4.1.8.a) and (4.1.8.b) deal with the light exiting the right output port of the PBS1. Here the light is horizontally-polarized, because our polarizing beam splitters transmit horizontally polarized components of light. Here the light first travels in succession through the HWP5 and the PBS3. The HWP5 is assumed to behave as a $\frac{\pi}{8}$-rotated half-wave plate, which will make the PBS3 to send equal amounts of the light into the part of the setup that includes the PAM1 and also into the part of the setup that includes the PAM2. The light that is transmitted by the PBS3 is horizontally-polarized, and when it is reflected by PAM1, its phase φ_H is transformed into the time dependent phase $\varphi_{H,1}(t) + \frac{\pi}{2}$, because the path length of the reflected light will change in time as the piezoelectric-actuated mirror actuates in time, and a factor of $\frac{\pi}{2}$ is added for the same reason as it is for $E_{z,a}^{in}$. The light then travels in succession through the HWP6 and the PBS4. The HWP6 is assumed to behave as a $\frac{\pi}{8}$-rotated half-wave plate, which will make the PBS4 to send equal amounts of the light into the part of the setup that includes Det1 and Det2 and

also into the part of the setup that includes the membrane resonator; note that the rotation angle of $\frac{\pi}{8}$ is in the present case picked in order to simplify the calculations, as in reality we here wish to send a larger amount of the light into the part of the setup that includes Det1 and Det2 and a smaller amount of the light into the part of the setup that includes the membrane resonator. The light then travels in succession through the QWP1 and the PBS5. The QWP1 is assumed to behave as explained in the paragraph above, and thus it will make the PBS5 to send the light in equals amounts into the Det1 and also into the Det2, when the lower output port of the PBS1 is blocked.

Note that the QWP1, the PBS1, and the photodetectors Det1 and Det2 realize the balanced homodyne detection scheme seen in figure C1 (b) (ii) in appendix C. In the language of appendix C, we have that the light entering the right input port of the PBS4 and then exiting through the lower output port of the PBS4 is the signal field, and the light entering the upper input port of the PBS4 and then exiting through the lower output port of the PBS4 is the local oscillator (LO). In the present case we will call the signal field as the *atomic signal field* and the LO as $\mathrm{LO_a}$.

From eqs. (4.1.8.a-b) and (D.2) we now find the difference in the intensities I_2 and I_1 of the electric fields that are picked up by the photodetectors Det2 and Det1, respectively, to be

$$\begin{aligned} &I_{2,1} \equiv I_2 - I_1 \propto \mathbf{V}_2^* \bullet \mathbf{V}_2 - \mathbf{V}_1^* \bullet \mathbf{V}_1 = \\ &= \hat{\tilde{x}}_L^{out} \cos\big(\varphi_1(t)\big) + \hat{\tilde{p}}_L^{out} \sin\big(\varphi_1(t)\big) \end{aligned} \quad , \qquad (4.1.9)$$

where $\hat{\tilde{x}}_L^{out}$ is the scaled $\hat{x}_L^{out}$ in eq. (4.1.6.a) with $\hat{\alpha}_n \rightarrow \frac{-E_{0H}}{2}\hat{\alpha}_n$, $\beta_1 \rightarrow \frac{E_{0H}}{\sqrt{8}E_{0V}}\beta_1$, $\beta_2 \rightarrow \frac{E_{0H}}{\sqrt{8}E_{0V}}\beta_2$; $\hat{\tilde{p}}_L^{out}$ is the scaled $\hat{p}_L^{out}$ in eq. (4.1.6.b) with $\hat{\alpha}_n \rightarrow \frac{-E_{0H}}{2}\hat{\alpha}_n$, $K_{\hat{X}_a,\hat{P}_a} \rightarrow \frac{-E_{0H}}{\sqrt{2}}K_{\hat{X}_a,\hat{P}_a}$; and $\varphi_1(t) \equiv \varphi_V - \varphi_{H,1}(t)$.

Observing appendix C, we see that the result of eq. (4.1.9) is exactly what we would expect by making use of this particular balanced homodyne detection scheme: by adjusting the $\mathrm{LO_a}$ phase $\varphi_{H,1}(t) + \frac{\pi}{2}$ to be such that $\varphi_{H,1}(t) = \varphi_V$ => $\varphi_1(t) = 0$, then the intensity $I_{2,1}$ will yield $\hat{\tilde{x}}_L^{out}$, and if the $\mathrm{LO_a}$ phase is adjusted such that $\varphi_{H,1}(t) = \varphi_V - \frac{\pi}{2}$ => $\varphi_1(t) = \frac{\pi}{2}$, then intensity $I_{2,1}$ will yield $\hat{\tilde{p}}_L^{out}$, which according to eq. (4.1.6.b) carries the *important* atomic signal expressed by $K_{\hat{X}_a,\hat{P}_a}$.

Observing figure 20 we now find the Jones vector for the light entering the cavity, where the membrane resonator resides:

$$\mathbf{V}_{\mathrm{membrane,in}} = \bar{\bar{\mathbf{M}}}_{\mathrm{tot_m}} \mathbf{V}_{\mathrm{PBS4,rp}} = \begin{bmatrix} E_{y,m}^{in} \\ 0 \end{bmatrix} \quad , \qquad (4.1.10)$$

where $\bar{\bar{\mathbf{M}}}_{\mathrm{tot_m}} \equiv \bar{\bar{\mathbf{M}}}_{\mathrm{QWP3}} \bar{\bar{\mathbf{M}}}_{\mathrm{PBS8,tr}} \bar{\bar{\mathbf{M}}}_{\mathrm{HWP10}} \bar{\bar{\mathbf{M}}}_{\mathrm{PBS6,tr}} \bar{\bar{\mathbf{M}}}_{\mathrm{HWP7}}$, and $\mathbf{V}_{\mathrm{PBS4,rp}}$ is the Jones vector for the light exiting the right output port of the PBS4, which is the same as the Jones vector for the light exiting the lower output port of the PBS4 with the horizontally-polarized component of the light and the vertically-polarized component of the light having switched places, and

$$E_{y,m}^{in} \equiv \frac{E_{y,a}^{out}}{2} + \frac{E_{0H}}{\sqrt{8}} e^{i\left(\varphi_{H,1}(t) - \omega_0 t + \frac{\pi}{2}\right)} \quad .$$

Eq. (4.1.10) deals with the light exiting the right output port of the PBS4, i.e. the light described the Jones vector $\mathbf{V}_{PBS4,rp}$. As understood from before, the light here includes the fluctuating vacuum field, Ω_β-sidebands, the Ω_L-sidebands, the *important* atomic signal expressed by $K_{\hat{X}_a,\hat{P}_a}$, and the relatively large LO_a. Here the light first travels in succession through the HWP7 and the PBS6. The HWP7 is assumed to behave as a $\frac{\pi}{8}$-rotated half-wave plate, and so, when the light will pass HWP7, the fluctuating vacuum field, Ω_β-sidebands, the Ω_L-sidebands, and the atomic signal will lie in the vertically- and the horizontally-polarized components of the light in equal amounts, when the right output port of the PBS1 is blocked, and also the LO_a will lie in the vertically- and the horizontally-polarized components of the light in equal amounts, when the lower output port of the PBS1 is blocked; and thus the PB6 will transmit the fluctuating vacuum field, Ω_β-sidebands, the Ω_L-sidebands, the atomic signal, and the LO_a. The light here then travels in succession through the fiber, HWP10 and the PBS8. The HWP10 is assumed to behave as a non-rotated half-wave plate, which introduces the phase shift $\varphi = \pi$ between the horizontal and vertical components of the light; note that the rotation angle of 0 is in the present case picked in order to simplify the calculations, as in reality the HWP10 *might* be rotated, because the fiber *can* rotate the polarization of the light that enters the fiber, and HWP10 corrects for that rotation such that the light that exits HWP10 is horizontally-polarized as it was when it has passed the PBS6. Note that, alternatively, the fiber itself can be used to correct for polarization mismatches. The PBS8 will thus transmit the same light as the PBS6 and at the same time reflect nothing, thereby not disturbing the light signal that enters the left input port of the PBS8. The light then travels through the QWP3 before entering the cavity, where the membrane resonator resides. The effect of the QWP3 is here neglected in order to simplify the forthcoming calculations. Note that one can neglect the effect of the QWP3, because as understood from section 1.6.3, cavity optomechanical resonators do not distinguish between different polarizations of light.

Now, the light will propagate into the cavity, where it will interact with the membrane resonator. The light's interaction with the membrane resonator will transform the "outside-of-cavity" light operators $\hat{x}'_L(z)$ and $\hat{p}'_L(z)$ according to the input-output relations (2.1.9.a-b). In order to express $\hat{x}'_L(z)$ and $\hat{p}'_L(z)$ in terms of the (complex) horizontal and vertical polarization components of the light seen in a Jones vector, we observe the definitions of the rotated in-phase and out-of-phase quadrature operators of a signal field expressed respectively as $\hat{x}_{S,\varphi_{LO}} \equiv \frac{1}{\sqrt{2}}\left(\hat{a}_S e^{-i\varphi_{LO}} + \hat{a}_S^\dagger e^{i\varphi_{LO}}\right)$ and $\hat{p}_{S,\varphi_{LO}} \equiv \frac{1}{i\sqrt{2}}\left(\hat{a}_S e^{-i\varphi_{LO}} - \hat{a}_S^\dagger e^{i\varphi_{LO}}\right)$, as seen in appendix C, and also eqs. (C.6.a-b) in appendix C, and thus we know that in our case we may write $\hat{x}'_L(z)$ and $\hat{p}'_L(z)$ as

$$\hat{x}'_L(z) = \frac{1}{\sqrt{2}}\left(E_{y,m} e^{-i(\varphi_{H,*}(t) - \omega_0 t)} + \overline{E}_{y,m} e^{i(\varphi_{H,*}(t) - \omega_0 t)}\right) \quad , \qquad (4.1.11.a)$$

$$\hat{p}'_L(z) = \frac{1}{i\sqrt{2}}\left(E_{y,m} e^{-i(\varphi_{H,*}(t) - \omega_0 t)} - \overline{E}_{y,m} e^{i(\varphi_{H,*}(t) - \omega_0 t)}\right) \quad , \qquad (4.1.11.b)$$

where $E_{y,m}$ is the horizontal polarization component of the light in a Jones vector for the light outside of the cavity, and $e^{-i(\varphi_{H,*}(t)-\omega_0 t)}$ is its phase. The reason why $E_{y,m}$ and $e^{-i(\varphi_{H,*}(t)-\omega_0 t)}$ are used is because in the present case it is assumed that the effect of the QWP3 is neglected such that horizontally-polarized light enters and also leaves the cavity.

Using eqs. (4.1.11.a-b) with $E_{y,m} = E_{y,m}^{in}$ from eq. (4.1.10) and $e^{-i(\varphi_{H,*}(t)-\omega_0 t)} = e^{i\left(\varphi_{H,1}(t)-\omega_0 t+\frac{\pi}{2}\right)}$ we have that the input "outside-of-cavity" light operators $\hat{x}_L'^{in}$ and $\hat{p}_L'^{in}$ are

$$\hat{x}_L'^{in} = -\frac{E_{0V}}{\sqrt{2}}\hat{\alpha}_n \cos(\Omega_L t) + \frac{E_{0V}}{\sqrt{8}}\beta_1 \cos\left(\Omega_{\beta_1} t\right)\sin\left(\varphi_1(t)\right) + \frac{E_{0V}}{\sqrt{8}}\beta_2 \cos(\Omega_L t)\sin\left(\varphi_1(t)\right) - \frac{K_{\hat{X}_a,\hat{P}_a}}{\sqrt{2}}\cos\left(\varphi_1(t)\right) + \frac{E_{0H}}{2} \quad , \quad (4.1.12.a)$$

$$\hat{p}_L'^{in} = -\frac{E_{0V}}{\sqrt{2}}\hat{\alpha}_n \cos(\Omega_L t) - \frac{E_{0V}}{\sqrt{8}}\beta_1 \cos\left(\Omega_{\beta_1} t\right)\cos\left(\varphi_1(t)\right) - \frac{E_{0V}}{\sqrt{8}}\beta_2 \cos(\Omega_L t)\cos\left(\varphi_1(t)\right) - \frac{K_{\hat{X}_a,\hat{P}_a}}{\sqrt{2}}\sin\left(\varphi_1(t)\right) \quad . \quad (4.1.12.b)$$

Now, as seen in eqs. (2.1.10.a-b) the filter seen in figure 3 allows us to equate the pairs of the light operators $\hat{x}_L^{out}$ and $\hat{x}_L'^{in}$, and $\hat{p}_L^{out}$ and $\hat{p}_L'^{in}$ as $\hat{x}_L'^{in} = -\hat{x}_L^{out}$ and $\hat{p}_L'^{in} = -\hat{p}_L^{out}$. From eqs. (4.1.12.a-b) we have that by adjusting the LO_a phase $\varphi_{H,1}(t) + \frac{\pi}{2}$ to be such that $\varphi_{H,1}(t) = \varphi_V - \frac{\pi}{2}$ => $\varphi_1(t) = \frac{\pi}{2}$, we obtain

$$\hat{x}_L'^{in} = -\frac{E_{0V}}{\sqrt{2}}\hat{\alpha}_n \cos(\Omega_L t) + \frac{E_{0V}}{\sqrt{8}}\beta_1 \cos\left(\Omega_{\beta_1} t\right) + \frac{E_{0V}}{\sqrt{8}}\beta_2 \cos(\Omega_L t) + \frac{E_{0H}}{2} \quad , \quad (4.1.12.a)$$

$$\hat{p}_L'^{in} = -\frac{E_{0V}}{\sqrt{2}}\hat{\alpha}_n \cos(\Omega_L t) - \frac{K_{\hat{X}_a,\hat{P}_a}}{\sqrt{2}} \quad . \quad (4.1.12.b)$$

Comparing eqs. (4.1.6.a-b) with eqs. (4.1.12.a-b) we see that $\hat{x}_L'^{in}$ is $-\hat{x}_L^{out}$ with the scalings $\hat{\alpha}_n \to \frac{\hat{\alpha}_n}{2}$, $\beta_1 \to \frac{\beta_1}{2E_{0V}}$, $\beta_2 \to \frac{\beta_2}{2E_{0V}}$ and an added static term $\frac{E_{0H}}{2}$; and $\hat{p}_L'^{in}$ is $-\hat{p}_L^{out}$ with the scalings $\hat{\alpha}_n \to \frac{\hat{\alpha}_n}{2}$ and $K_{\hat{X}_a,\hat{P}_a} \to \frac{K_{\hat{X}_a,\hat{P}_a}}{\sqrt{2}}$. Since the scalings do not invert signs and the added term is *static*, we may therefore by observing eqs. (2.1.10.a-b) conclude that our interferometer, which is enclosed in a dashed blue contour in figure 20, satisfies the role of the filter seen in figure 3, when $\varphi_1(t) = \frac{\pi}{2}$.

Note that the reason why $E_{y,m}^{in}$ has the phase $e^{-i\left(\varphi_{H,1}(t)-\omega_0 t+\frac{\pi}{2}\right)}$ is because, as seen from before, LO_a is horizontally-polarized and so must carry this particular phase.

Note that when $\varphi_1(t) = \frac{\pi}{2}$, then eq. (4.1.9) tells us that

$$I_{2,1} \propto \hat{\tilde{p}}_L^{out} = \frac{-E_{0H}E_{0V}}{\sqrt{2}}\hat{\alpha}_n \cos(\Omega_L t) + \frac{-E_{0H}}{\sqrt{2}}K_{\hat{X}_a,\hat{P}_a} \quad ; \quad (4.1.13)$$

from which we observe that as our interferometer satisfies the role of the filter, we simultaneously keep track of the fluctuating vacuum field and the atomic signal by the use of the balanced homodyne detection scheme realized by the QWP1, the PBS1, and the photodetectors Det1 and Det2.

Note that we stabilize the LO_a phase via a feedback-mechanism. We first send the subtracted photocurrent $i_{2,1} \equiv i_2 - i_1$, where i_1 and i_2 are the photocurrents provided by the photodetectors Det1 and Det2, respectively, to a lock-in amplifier. The lock-in amplifier demodulates the signal carried by $i_{2,1}$ at the sideband frequency Ω_β, and then provides this demodulated signal to a proportional-integral (PI) controller. The signal generated by the PI controller then travels to the PAM1, and this completes the LO_a phase stabilizing feedback-mechanism.

Note that in the forthcomming calculations we shall assume that the LO_a phase is stabilized such that $\varphi_{H,1}(t) = \varphi_V - \frac{\pi}{2} \Rightarrow \varphi_1(t) = \frac{\pi}{2}$.

Now, using eqs. (4.1.11.a-b) we have that the input-output relations (2.1.9.a-b) for the "outside-of-cavity" light operators $\hat{x}'_L(z)$ and $\hat{p}'_L(z)$ in our case read as

$$\left.\begin{aligned} \hat{x}'^{out}_L &= -\hat{x}'^{in}_L \\ \hat{p}'^{out}_L &= -\hat{p}'^{in}_L + K_{\hat{X}_m,\hat{P}_m} \end{aligned}\right\} <=>$$

$$\frac{1}{\sqrt{2}}\left(E^{out}_{y,m} e^{-i(\varphi_{H,2}(t)-\omega_0 t)} + \bar{E}^{out}_{y,m} e^{i(\varphi_{H,2}(t)-\omega_0 t)}\right) = \frac{-1}{\sqrt{2}}\left(E^{in}_{y,m} e^{-i\left(\varphi_{H,1}(t)-\omega_0 t+\frac{\pi}{2}\right)} + \bar{E}^{in}_{y,m} e^{i\left(\varphi_{H,1}(t)-\omega_0 t+\frac{\pi}{2}\right)}\right), \quad (4.1.14.a)$$

$$\frac{1}{i\sqrt{2}}\left(E^{out}_{y,m} e^{-i(\varphi_{H,2}(t)-\omega_0 t)} - \bar{E}^{out}_{y,m} e^{i(\varphi_{H,2}(t)-\omega_0 t)}\right) = \frac{-1}{i\sqrt{2}}\left(E^{in}_{y,m} e^{-i\left(\varphi_{H,1}(t)-\omega_0 t+\frac{\pi}{2}\right)} - \bar{E}^{in}_{y,m} e^{i\left(\varphi_{H,1}(t)-\omega_0 t+\frac{\pi}{2}\right)}\right) + K_{\hat{X}_m,\hat{P}_m}, \quad (4.1.14.b)$$

where $E^{in}_{y,m}$ is the horizontal component of the light seen in the Jones vector for the light entering the cavity, i.e. $\mathbf{V}_{membrane,in}$ in eq. (4.1.10), $E^{out}_{y,m}$ is the horizontal component of the light seen in the Jones vector for the light exiting the cavity, $e^{-i\left(\varphi_{H,1}(t)-\omega_0 t+\frac{\pi}{2}\right)}$ is the phase of $E^{in}_{y,m}$, $e^{-i(\varphi_{H,2}(t)-\omega_0 t)}$ is the phase of $E^{out}_{y,m}$, and

$$K_{\hat{X}_m,\hat{P}_m} \equiv -g_{m,c}\sqrt{\frac{2}{\eta_c}}\left(-\hat{P}^*_m \sin(\Omega_m t) + \hat{X}^*_m \cos(\Omega_m t)\right) = -g_{m,c}\sqrt{\frac{2}{\eta_c}}\left(\hat{P}^*_m \sin\left(\Omega_{L,n} t\right) + \hat{X}^*_m \cos\left(\Omega_{L,n} t\right)\right),$$

where $\Omega_m = -\Omega_{L,n}$ is used, i.e. the equality in eq. (2.1.11.b), which is justified in our case, because as already mentioned, our membrane resonator is designed such that it would show significant response at frequencies around Ω_L. Note that $E^{out}_{y,m}$ has the phase $e^{-i(\varphi_{H,2}(t)-\omega_0 t)}$, where it is seen that $\varphi_{H,1}(t) \to \varphi_{H,2}(t) - \frac{\pi}{2}$ after the interaction with the membrane resonator; this happens because the membrane resonator vibrates, and so, the path length of the reflected light will change in time and by the same token the phase $e^{i\frac{\pi}{2}} = i$ can be dropped. Note that $\hat{x}'^{out}_L$ and $\hat{p}'^{out}_L$ in the present case describe the light that is reflected out of the cavity; this is in accord with the assumption that nothing will get transmitted through the cavity. This is a valid assumption, because as mentioned in the text of figure 19, the output mirror of the cavity has much higher reflectivity than the input

mirror of the cavity, and so the light entering the cavity has much higher probability to be reflected out of the cavity than to be transmitted. Note that the small amount of the light that does get transmitted, gets picked up by the photodetector Det5 seen in figure 20.

Using eqs. (4.1.10) and (4.1.14.a-b) we thus obtain the Jones vector for the light exiting the cavity:

$$\mathbf{V}_{\text{membrane,out}} = \begin{bmatrix} E_{y,m}^{out} \\ 0 \end{bmatrix} = \begin{bmatrix} \frac{i}{\sqrt{2}} K_{\hat{X}_m,\hat{P}_m} e^{i(\varphi_{H,2}(t)-\omega_0 t)} + \tilde{E}_{y,m}^{in} \\ 0 \end{bmatrix} , \quad (4.1.15)$$

where $\tilde{E}_{y,m}^{in} = \frac{1}{\sqrt{8}} E_{0H} e^{i(\varphi_{H,2}(t)-\omega_0 t)} + \tilde{E}_{y,a}^{out}$, where $\tilde{E}_{y,a}^{out}$ is $E_{y,a}^{out}$ in eq. (4.1.7) with the phases $e^{i(\varphi_{H,2}(t)-\omega_0 t)}$ instead of $e^{i\left(\varphi_V-\omega_0 t+\frac{\pi}{2}\right)}$, and $K_{\hat{X}_a,\hat{P}_a} \to i\frac{-K_{\hat{X}_a,\hat{P}_a}}{2}$, $\hat{\alpha}_n \to \frac{E_{0V}}{2}\hat{\alpha}_n$, $\beta_1 \to i\frac{\beta_1}{2}$, and $\beta_2 \to i\frac{\beta_2}{2}$. Notice that $K_{\hat{X}_a,\hat{P}_a}$, β_1 and β_2 in eq. (4.1.15) acquire the phase $e^{i\frac{\pi}{2}} = i$, just as $K_{\hat{X}_m,\hat{P}_m}$ does.

Observing figure 20 we now find:

1. The Jones vector for the light incident on the photodetector Det3:

$$\mathbf{V}_3 = \bar{\bar{\mathbf{M}}}_{tot3}\mathbf{V}_{\text{membrane,out}} + \bar{\bar{\mathbf{M}}}_{tot3},\mathbf{V}_{in} = \begin{bmatrix} 0 \\ K_{k,m}E_{0H}e^{i(\varphi_{H,3}(t)-\omega_0 t)} + K_{k,m}E_{y,m}^{out} \end{bmatrix} , \quad (4.1.16.a)$$

2. The Jones vector for the light incident on the photodetector Det4:

$$\mathbf{V}_4 = \bar{\bar{\mathbf{M}}}_{tot4}\mathbf{V}_{\text{membrane,out}} + \bar{\bar{\mathbf{M}}}_{tot4},\mathbf{V}_{in} = \begin{bmatrix} K_{k,m}E_{0H}e^{i(\varphi_{H,3}(t)-\omega_0 t)} - K_{k,m}E_{y,m}^{out} \\ 0 \end{bmatrix} . \quad (4.1.16.b)$$

In eqs. (4.1.16.a-b) we have $K_{k,m} \equiv \frac{1}{\sqrt{2}}$, $\bar{\bar{\mathbf{M}}}_{tot3} \equiv \bar{\bar{\mathbf{M}}}_{PBS9,r}\bar{\bar{\mathbf{M}}}_{HWP11}\bar{\bar{\mathbf{M}}}_{PBS8,tr}\bar{\bar{\mathbf{M}}}_{QWP3}$, $\bar{\bar{\mathbf{M}}}_{tot3}$, $\equiv \bar{\bar{\mathbf{M}}}_{PBS9,r}\bar{\bar{\mathbf{M}}}_{HWP11}\bar{\bar{\mathbf{M}}}_{PBS8,tr}\bar{\bar{\mathbf{M}}}_{HWP9}\bar{\bar{\mathbf{M}}}_{PBS7,r}\bar{\bar{\mathbf{M}}}_{QWP2}\bar{\bar{\mathbf{M}}}_{PAM2}\bar{\bar{\mathbf{M}}}_{QWP2}\bar{\bar{\mathbf{M}}}_{PBS7,tr}\bar{\bar{\mathbf{M}}}_{HWP8}\bar{\bar{\mathbf{M}}}_{PBS3,r}\bar{\bar{\mathbf{M}}}_{HWP5}\bar{\bar{\mathbf{M}}}_{PBS1,tr}$, and $\bar{\bar{\mathbf{M}}}_{tot4}$ and $\bar{\bar{\mathbf{M}}}_{tot4}$, are respectively $\bar{\bar{\mathbf{M}}}_{tot3}$ and $\bar{\bar{\mathbf{M}}}_{tot3}$, with $\bar{\bar{\mathbf{M}}}_{PBS9,r} \to \bar{\bar{\mathbf{M}}}_{PBS9,tr}$.

The first terms of the sum in eqs. (4.1.16.a) and (4.1.16.b) deal with the light reflected out of the cavity by the membrane resonator. Here the light first travels in succession through the QWP3 and the PBS8. As noted from before, the effect of the QWP3 was here neglected in order to simplify the calculations above. In reality, QWP3 should be assumed to behave as a $\frac{\pi}{4}$-rotated quarter-wave plate, which would make the horizontally-polarized light exiting the upper output port of the PBS8 to be converted to circularly-polarized light. If such circularly-polarized light then becomes reflected on the membrane resonator, the handedness of the circular polarization changes because of the orthogonal angle of incidence, and so, when such light propagates through QWP3 again, this light then becomes vertically-polarized. The PBS8 will thus reflect all of the light and at the same time transmit nothing, thereby not disturbing the light signal that enters the lower input port of the PBS8. If the effect of the QWP3 is neglected, or, equivalently, the QWP3 is not placed after the PBS8, this will, however, no longer hold, because then PBS8 will actually transmit everything and reflect nothing as no polarization changes will happen upon reflection on the membrane resonator. Nevertheless, eq. (4.1.15) still holds, since as mentioned before, cavity optomechanical resonators

do not distinguish between different polarizations of light; and for that reason we shall rightfully assume that the light described by $\mathbf{V}_{\mathrm{membrane,out}}$ in eq. (4.1.15) is totally reflected by the PBS8, where it then travels in succession through the HWP11 and the PBS9. The HWP11 is assumed to behave as a $\frac{\pi}{8}$-rotated half-wave plate, which will make the PBS9 to send the light in equals amounts into the Det3 and also into the Det4, when the left input port of the PBS8 is blocked, such that the detection becomes balanced.

The second terms of the sum in eqs. (4.1.16.a) and (4.1.16.b) deal with the light exiting the right output port of the PBS1. Here the light is horizontally-polarized, because our polarizing beam splitters transmit horizontally-polarized components of light. Here the light first travels in succession through the HWP5 and the PBS3. The HWP5 is assumed to behave as explained below eqs. (4.1.8.a-b); this will make the PBS3 to send equal amounts of the light through its right output port and through its upper output port. In the present case we deal with the light exiting the upper output port of the PBS3. Here the light first travels in succession through the HWP8 and the PBS7. The HWP8 is assumed to behave as a π-rotated half-wave plate, which will make the vertically-polarized light exiting the upper output port of the PBS3 to be converted to horizontally-polarized light such that the PBS7 can transmit all of the light. The light then travels through the QWP2, is reflected by the PAM2, and then travels through the QWP3 again. The QWP2 is assumed to behave as a $\frac{\pi}{4}$-rotated quarter-wave plate, which will make the horizontally-polarized light exiting the upper output port of the PBS7 to be converted to circularly-polarized light. When the light is reflected by PAM2, its phase φ_{H} is transformed into the time dependent phase $\varphi_{\mathrm{H},3}(\mathrm{t})$, because the path length of the reflected light will change in time as the piezoelectric-actuated mirror actuates in time, and also the handedness of the circular polarization of the light changes, because of the orthogonal angle of incidence, and so, when the light propagates through QWP2 again, the light will become vertically-polarized. The PBS7 will thus reflect all of the light and at the same time transmit nothing, thereby not disturbing the light signal that enters the lower input port of the PBS7. The light then travels in succession through the fiber, HWP9 and the PBS8. The HWP9 is assumed to behave as a π-rotated half-wave plate, which will make the vertically-polarized light exiting the fiber to be converted to horizontally-polarized light such that the PBS8 can transmit all of the light. The PBS8 will thus transmit the same light that is reflected by the PBS7, and also at the same time reflect nothing, thereby not disturbing the light signal that enters the lower input port of the PBS8. The light then travels in succession through the HWP11 and the PBS9. The HWP11 is assumed to behave as explained in the paragraph above, and thus it will make the PBS9 to send the light in equals amounts into the Det3 and also into the Det4, when the lower input port of the PBS8 is blocked.

Note that the HWP11, the PBS9, and the photodetectors Det3 and Det4 realize the balanced homodyne detection scheme seen in figure C1 (b) (i) in appendix C. In the language of appendix C, we have that the light entering the upper input/output port of the PBS8 and then exiting through the right output port of the PBS8 is the signal field, and the light entering the left input port of the PBS4 and then exiting through the right output port of the PBS8 is the local oscillator (LO). In the present case we will call the signal field as the *membrane signal field* and the LO as $\mathrm{LO_m}$.

From eqs. (4.1.16.a-b) and (D.2) we now find the difference in the intensities I_4 and I_3 of the electric fields that are picked up by the photodetectors Det4 and Det3, respectively, to be

$$\begin{aligned} I_{4,3} \equiv I_4 - I_3 \propto \mathbf{V}_4^* \bullet \mathbf{V}_4 - \mathbf{V}_3^* \bullet \mathbf{V}_3 = \\ = \hat{\tilde{x}}'^{out}_L \cos(\varphi_2(t)) + \hat{\tilde{p}}'^{out}_L \sin(\varphi_2(t)) \end{aligned} \quad , \qquad (4.1.17)$$

where

$$\hat{\tilde{x}}'^{out}_L = -\hat{\tilde{x}}^{in}_L + \frac{1}{\sqrt{2}} E^2_{0H} \quad , \qquad (4.1.18.a)$$

$$\hat{\tilde{p}}'^{out}_L = -\hat{\tilde{p}}^{in}_L + \tilde{K}_{\hat{X}_a,\hat{P}_a} + \tilde{K}_{\hat{X}_m,\hat{P}_m} \quad , \qquad (4.1.18.b)$$

where $\hat{\tilde{x}}^{in}_L$ is the scaled $\hat{x}^{in}_L$ in eq. (4.1.6.a) and $\hat{\tilde{p}}^{in}_L$ is the scaled $\hat{p}^{in}_L$ in eq. (4.1.6.b) with $\hat{\alpha}_n \to \sqrt{2}E_{0H}\hat{\alpha}_n$, $\beta_1 \to \frac{E_{0H}}{\sqrt{2E_{0V}}}\beta_1$, $\beta_2 \to \frac{E_{0H}}{\sqrt{2E_{0V}}}\beta_2$; and $\tilde{K}_{\hat{X}_a,\hat{P}_a} \equiv -E_{0H}K_{\hat{X}_a,\hat{P}_a}$, $\tilde{K}_{\hat{X}_m,\hat{P}_m} \equiv -\sqrt{2}E_{0H}K_{\hat{X}_m,\hat{P}_m}$. Note that the different scalings in $\hat{\tilde{x}}^{in}_L$ and $\hat{\tilde{p}}^{in}_L$ do not invert signs, and in the definitions of $\tilde{K}_{\hat{X}_a,\hat{P}_a}$ and $\tilde{K}_{\hat{X}_m,\hat{P}_m}$ we have that both $K_{\hat{X}_a,\hat{P}_a}$ and $K_{\hat{X}_m,\hat{P}_m}$ are negated.

Observing eq. (C.7.b) in appendix C, we see that the result of eq. (4.1.17) is exactly what we would expect by making use of this particular balanced homodyne detection scheme: by adjusting the LO_m phase $\varphi_{H,3}(t)$ to be $\varphi_{H,3}(t) = \varphi_{H,2}(t) \Rightarrow \varphi_2(t) = 0$, then the intensity $I_{4,3}$ will yield $\hat{\tilde{x}}'^{out}_L$, and if the LO_m phase $\varphi_{H,3}(t) = \varphi_{H,2}(t) - \frac{\pi}{2} \Rightarrow \varphi_2(t) = \frac{\pi}{2}$, then intensity $I_{4,3}$ will yield $\hat{\tilde{p}}'^{out}_L$, which according to eq. (4.1.14.b) carries the *important* membrane signal expressed by $K_{\hat{X}_a,\hat{P}_a}$ and $K_{\hat{X}_m,\hat{P}_m}$.

Now, observing the definitions of $K_{\hat{X}_a,\hat{P}_a}$ and $K_{\hat{X}_m,\hat{P}_m}$, and the above paragraph, and figure 3, and eqs. (2.1.12.a-b), (4.1.17), (4.1.18.a-b), and section 2.2, where the atomic and the membrane resonator parameter mismatch is mentioned, i.e. when $\kappa\sqrt{\frac{2}{\tau}} \neq g_{m,c}\sqrt{\frac{2}{\eta_c}}$, we see that $\hat{\tilde{p}}'^{out}_L$ can be used to derive a similar expression of the modified version of the reduced EPR variance, i.e. $\sum_{EPR} + [\epsilon\kappa(\bar{n}_{th} + 2)]^2$ (seen in section 2.2), that includes the atomic and the membrane resonator parameter mismatch, such that we can conclude that our atom-membrane interfacing experimental setup can allow us to satisfy the entanglement protocol described in chapter 2.

4.2 Matching of the atomic and the membrane resonator parameters

According to section 2.2, when the atomic and the membrane resonator parameters are mismatched, i.e. when $\kappa\sqrt{\frac{2}{\tau}} \neq g_{m,c}\sqrt{\frac{2}{\eta_c}}$, the EPR variance $\sum_{EPR}$ given by eq. (2.1.19) becomes modified such that a practical limit to the initial thermal occupation of the membrane resonator is set. Since controlling the initial thermal occupation of the membrane resonator involves controlling the temperature of the resonator, and when the atomic and the membrane resonator parameters are very mismatched, we may need to cool the resonator to temperatures close to zero Kelvin, which is experimentally challenging to perform, it then starts to make sense *experimentally* to minimize the mismatch between the atomic and the membrane resonator parameters as much as possible.

Now, in order to find out experimentally, when the atomic and the membrane resonator parameters become matched, i.e. when $\kappa\sqrt{\frac{2}{\tau}} = g_{m,c}\sqrt{\frac{2}{\eta_c}}$ (see eq. (2.1.11.a)), we use an electro-optic modulator (EOM) to create Larmor frequency Ω_L-sidebands centered around the carrier angular frequency ω_0 of the probe laser, and let these sidebands propagate through the atoms and eventually enter the cavity, where the membrane resonator resides. As mentioned in section 4.1, both the relatively large Ω_L-sidebands and the fluctuating vacuum field drive the atoms and the resonator. Now, the Ω_L-sidebands are different from the fluctuating vacuum field in a sense that the Ω_L-sidebands are *classical* and the fluctuating vacuum field is *quantum*. Let us now try to understand why this is not a trivial statement.

In order to gain access to $\hat{P}_m^* - \hat{P}_a^*$ and $\hat{X}_m^* + \hat{X}_a^*$ in our atom-membrane entanglement experiment we first stabilize the LO_m phase $\varphi_{H,3}(t)$ such that $\varphi_{H,3}(t) = \varphi_{H,2}(t) - \frac{\pi}{2}$ => $\varphi_2(t) = \frac{\pi}{2}$ such that the subtracted intensity $I_{4,3}$ in eq. (4.1.17) yields $\hat{\tilde{p}}'^{out}_L$. Then the photocurrent that carries with itself information about $\hat{\tilde{p}}'^{out}_L$ is fed to a lock-in amplifier. The lock-in amplifier demodulates the signal carried by the photocurrent at the Larmor frequency Ω_L, and provides us with signals that carry with themselves information about

$$\hat{p}'^{out}_{L,cos} = \hat{p}^{in}_{L,cos} + g_{m,c}\sqrt{\frac{\tau}{\eta_c}}\hat{X}_m^* + \kappa\hat{X}_a^* \quad , \tag{4.2.1.a}$$

$$\hat{p}'^{out}_{L,sin} = \hat{p}^{in}_{L,sin} + g_{m,c}\sqrt{\frac{\tau}{\eta_c}}\hat{P}_m^* - \kappa\hat{P}_a^* \quad , \tag{4.2.1.b}$$

which are the atomic and the membrane resonator parameter mismatched versions of $\hat{p}'^{out}_{L,cos}$ and $\hat{p}'^{out}_{L,sin}$ seen in eqs. (2.1.14.a) and (2.1.14.b), respectively. Eqs. (4.2.1.a-b) are obtained by making use of eqs. (2.1.14.a-b) with $\hat{p}'^{out}_L$ in eq. (2.1.12.b) in a case, where $\kappa\sqrt{\frac{2}{\tau}} \neq g_{m,c}\sqrt{\frac{2}{\eta_c}}$, with the assumptions $\int_0^\tau dt\,\hat{X}_j^*(t)\cos^2(\Omega_{L,n}t) \approx \int_0^\tau dt\,\hat{X}_j^*(t)\sin^2(\Omega_{L,n}t) \approx \hat{X}_j^*(t)\frac{\tau}{2}$, and
$\int_0^\tau dt\,\hat{P}_j^*(t)\cos^2(\Omega_{L,n}t) \approx \int_0^\tau dt\,\hat{P}_j^*(t)\sin^2(\Omega_{L,n}t) \approx \hat{P}_j^*(t)\frac{\tau}{2}$, and
$\int_0^\tau dt\,\hat{X}_j^*(t)\sin(\Omega_{L,n}t)\cos(\Omega_{L,n}t) \approx 0$, and $\int_0^\tau dt\,\hat{P}_j^*(t)\sin(\Omega_{L,n}t)\cos(\Omega_{L,n}t) \approx 0$, where j = a, m, and $\hat{X}_j^* = \hat{X}_j^*(t)$ and $\hat{P}_j^* = \hat{P}_j^*(t)$ are solutions to eqs. (2.1.8.c-d) and (2.1.9.c-d):

$$\hat{X}_a^* = \hat{X}_a^*(0) - \kappa\sqrt{\frac{2}{\tau}}\int_0^t dt'\,\hat{x}_L^{in}(t')\sin(\Omega_L t') \quad , \tag{4.2.2.a}$$

$$\hat{P}_a^* = \hat{P}_a^*(0) + \kappa\sqrt{\frac{2}{\tau}}\int_0^t dt'\,\hat{x}_L^{in}(t')\cos(\Omega_L t') \quad , \tag{4.2.2.b}$$

$$\hat{X}_m^* = \hat{X}_m^*(0) + g_{m,c}\sqrt{\frac{2}{\eta_c}}\int_0^t dt'\,\hat{x}_L^{in}(t')\sin(\Omega_L t') \quad , \tag{4.2.2.c}$$

$$\hat{P}_m^* = \hat{P}_m^*(0) + g_{m,c}\sqrt{\frac{2}{\eta_c}}\int_0^t dt'\,\hat{x}_L^{in}(t')\cos(\Omega_L t') \quad . \tag{4.2.2.d}$$

where $\Omega_{L,n} \equiv -\Omega_L$, $\Omega_m = \Omega_L$, and $\hat{x}'^{in}_L = \hat{x}^{in}_L$ are used. Note that the aforementioned assumptions are justified if the time period of the protocol, $t_1 \approx \tau$, is much longer than $1/\Omega_L$, i.e. $\tau \gg 1/\Omega_L$, which indeed is the case in our atom-membrane entanglement experiment.

With $\hat{\tilde{x}}^{in}_L$ in eq. (4.1.18.a) being $\hat{\tilde{x}}^{in}_L \to \hat{x}^{in}_L = -\sqrt{2}E_{0V}\hat{\alpha}_n \cos(\Omega_L t) + \frac{E^2_{0V}}{\sqrt{2}}\beta_1 \cos(\Omega_{\beta_1} t) + \frac{E^2_{0V}}{\sqrt{2}}\beta_2 \cos(\Omega_L t) \to -\hat{\alpha}_n \cos(\Omega_L t) + \beta_2 \cos(\Omega_L t)$ we calculate the mean values of $\hat{p}'^{out}_{L,cos}$ and $\hat{p}'^{out}_{L,sin}$:

$$\left.\begin{aligned}\langle \hat{p}'^{out}_{L,cos}\rangle &= \langle \hat{p}^{in}_{L,cos}\rangle + g_{m,c}\sqrt{\frac{\tau}{\eta_c}}\langle \hat{X}^*_m(0)\rangle + g^2_{m,c}\sqrt{\frac{2\tau}{\eta_c^2}}\left(\int_0^\tau dt\, \hat{x}^{in}_L(t)\sin(\Omega_L t)\right) + \kappa\langle \hat{X}^*_a(0)\rangle - \kappa^2\sqrt{\frac{2}{\tau}}\left(\int_0^\tau dt\, \hat{x}^{in}_L(t)\sin(\Omega_L t)\right)\\ \langle \hat{p}'^{out}_{L,sin}\rangle &= \langle \hat{p}^{in}_{L,sin}\rangle + g_{m,c}\sqrt{\frac{\tau}{\eta_c}}\langle \hat{P}^*_m(0)\rangle + g^2_{m,c}\sqrt{\frac{2\tau}{\eta_c^2}}\left(\int_0^\tau dt\, \hat{x}^{in}_L(t)\cos(\Omega_L t)\right) - \kappa\langle \hat{P}^*_a(0)\rangle - \kappa^2\sqrt{\frac{2}{\tau}}\left(\int_0^\tau dt\, \hat{x}^{in}_L(t)\cos(\Omega_L t)\right)\end{aligned}\right\} =>$$

$$\langle \hat{p}'^{out}_{L,cos}\rangle = K_{cos}\beta_2\left(g^2_{m,c}\sqrt{\frac{2\tau}{\eta_c^2}} - \kappa^2\sqrt{\frac{2}{\tau}}\right) \quad , \tag{4.2.3.a}$$

$$\langle \hat{p}'^{out}_{L,sin}\rangle = K_{sin}\beta_2\left(g^2_{m,c}\sqrt{\frac{2\tau}{\eta_c^2}} - \kappa^2\sqrt{\frac{2}{\tau}}\right) \quad , \tag{4.2.3.b}$$

where $\langle . \rangle$ refers to the mean value in this section, and $\int_0^\tau dt \cos(\Omega_L t)\sin(\Omega_L t) = K_{cos}$ and $\int_0^\tau dt \cos^2(\Omega_L t) = K_{sin}$, where $K_{cos} \equiv \frac{1-\cos^2(\Omega_L \tau)}{\Omega_L}$ and $K_{sin} \equiv \frac{\cos(\Omega_L\tau)\sin(\Omega_L\tau)+\Omega_L\tau}{\Omega_L}$ are the solutions to the integrals, and $K_{cos} \ll K_{sin}$, when $\tau \gg 1/\Omega_L$.

In eqs. (4.2.3.a-b) we have that $\langle \hat{p}^{in}_{L,cos}\rangle = \langle \hat{p}^{in}_{L,sin}\rangle = \langle \hat{X}^*_m(0)\rangle = \langle \hat{X}^*_a(0)\rangle = \langle \hat{P}^*_m(0)\rangle = \langle \hat{P}^*_a(0)\rangle = \langle \hat{\alpha}_n\rangle = 0$, because here we are dealing with quantum operators; and $\langle \beta_2\rangle \neq 0$, because β_2 is a classical amplitude. Also, in the same eqs. (4.2.3.a-b) we have that if the atomic and the membrane resonator parameters are matched, i.e. when $\kappa\sqrt{\frac{2}{\tau}} = g_{m,c}\sqrt{\frac{2}{\eta_c}}$, then $\langle \hat{p}'^{out}_{L,cos}\rangle = 0$ and $\langle \hat{p}'^{out}_{L,sin}\rangle = 0$; however, if the atomic and the membrane resonator parameters are mismatched, i.e. when $\kappa\sqrt{\frac{2}{\tau}} \neq g_{m,c}\sqrt{\frac{2}{\eta_c}}$, then $\langle \hat{p}'^{out}_{L,cos}\rangle \neq 0$ and $\langle \hat{p}'^{out}_{L,sin}\rangle \neq 0$. We see now that the classical Ω_L-sidebands introduce *classical* light back-action noise into our measurements, and that by cancelling this noise we can match the atomic and the membrane resonator parameters.

Note as well that $\hat{x}^{in}_L \to \hat{\alpha}_n \cos(\Omega_L t) - \beta_2 \cos(\Omega_L t)$, because as mentioned in section 4.1, the atoms and the membrane resonator show significant response at the Larmor frequency Ω_L, and so the term $E^2_{0V}\beta_1 \cos(\Omega_{\beta_1} t)$ appearing in $\hat{x}^{in}_L$ in eq. (4.1.6.a) can be neglected.

Let us now define

$$\langle \hat{p}'^{out}_{L,cos,a} \rangle \equiv \langle \hat{p}^{in}_{L,cos} + \kappa \hat{X}^{*}_{a} \rangle = -K_{cos}\beta_2 \kappa^2 \sqrt{\frac{2}{\tau}} \quad , \tag{4.2.4.a}$$

$$\langle \hat{p}'^{out}_{L,sin,a} \rangle \equiv \langle \hat{p}^{in}_{L,sin} - \kappa \hat{P}^{*}_{a} \rangle = -K_{sin}\beta_2 \kappa^2 \sqrt{\frac{2}{\tau}} \quad , \tag{4.2.4.b}$$

$$\langle \hat{p}'^{out}_{L,cos,m} \rangle \equiv \langle \hat{p}^{in}_{L,cos} + g_{m,c}\sqrt{\frac{\tau}{\eta_c}} \hat{X}^{*}_{m} \rangle = K_{cos}\beta_2 g^2_{m,c} \sqrt{\frac{2\tau}{\eta_c^2}} \quad , \tag{4.2.4.c}$$

$$\langle \hat{p}'^{out}_{L,sin,m} \rangle \equiv \langle \hat{p}^{in}_{L,sin} + g_{m,c}\sqrt{\frac{\tau}{\eta_c}} \hat{P}^{*}_{m} \rangle = K_{sin}\beta_2 g^2_{m,c} \sqrt{\frac{2\tau}{\eta_c^2}} \quad , \tag{4.2.4.d}$$

where in the equalities one uses eqs. (4.2.3.a-b).

Eqs. (4.2.4.a-b) refer to a case, when the cavity, where the membrane resonator resides, is off-resonantly tuned such that the light that is incident on the cavity will get reflected, such that the photodetectors Det3 and Det4 seen in figure 20 will only pick up the atomic signal; and eqs. (4.2.4.c-d) refer to a case, where the pump and repump lasers are turned off, such that the atoms are not optically pumped to the coherent spin state $|4,4>$, such that the photodetectors Det3 and Det4 will only pick up the membrane resonator signal.

Note that we will say that eqs. (4.2.4.a-b) refer to a case, where the membrane resonator is "turned off", and eqs. (4.2.4.c-d) refers to a case, where the atomic ensemble is "turned off".

Note that by observing the definitions for $\langle \hat{p}'^{out}_{L,cos,a} \rangle$, $\langle \hat{p}'^{out}_{L,sin,a} \rangle$, $\langle \hat{p}'^{out}_{L,cos,m} \rangle$ and $\langle \hat{p}'^{out}_{L,sin,m} \rangle$ seen in eqs. (4.2.4.a-d), we cannot, however, conclude that if $\langle \hat{p}'^{out}_{L,cos,a} \rangle + \langle \hat{p}'^{out}_{L,cos,m} \rangle = 0$ or $\langle \hat{p}'^{out}_{L,sin,a} \rangle + \langle \hat{p}'^{out}_{L,sin,m} \rangle = 0$, when the EOM is producing the classical Ω_L-sidebands, then the atomic and the membrane resonator parameters become matched, because, as mentioned earlier, these equations refer to cases where either the atomic ensemble or the membrane resonator is "turned off", such that the information about two connected systems becomes lost. Nevertheless, this does not translate to that measurements of $\langle \hat{p}'^{out}_{L,cos,a} \rangle$, $\langle \hat{p}'^{out}_{L,cos,m} \rangle$, $\langle \hat{p}'^{out}_{L,sin,a} \rangle$, and $\langle \hat{p}'^{out}_{L,sin,m} \rangle$ would be of little value, because by comparing by how much the mean values in the atomic and also in the membrane case are shifted away from the zero-mean we *expect* to obtain a rough estimate that could show us how good we are at matching the atomic and the membrane resonator parameters.

Now, we will say that

$$\langle \hat{p}'^{out}_{L,cos,+} \rangle \quad , \tag{4.2.4.e}$$

$$\langle \hat{p}'^{out}_{L,sin,+} \rangle \quad , \tag{4.2.4.f}$$

$$\langle \hat{p}'^{out}_{L,cos,a+} \rangle \quad , \tag{4.2.4.g}$$

$$\langle \hat{p}'^{out}_{L,sin,a+} \rangle \tag{4.2.4.h}$$

refer to the mean values of $\hat{p}'^{out}_{L,cos}$, $\hat{p}'^{out}_{L,sin}$, $\hat{p}'^{out}_{L,cos,a}$, $\hat{p}'^{out}_{L,sin,a}$, respectively, in a case, when the Cesium-133 atoms are optically pumped to the coherent spin state $|4,-4>$. This can be achieved by letting the static magnetic field $\mathbf{B}_{static}$ seen in figure 20 to point in the negative direction of the z-direction. According to section 2.1, we have that, when the atoms are optically pumped to the

coherent spin state $|4,-4>$, the atomic ensemble is modeled as a positive-mass (single-mode) harmonic oscillator, just as it is the case for the membrane resonator.

Note that to complement $\langle \hat{p}'^{out}_{L,cos,+} \rangle$, $\langle \hat{p}'^{out}_{L,sin,+} \rangle$, $\langle \hat{p}'^{out}_{L,cos,a+} \rangle$ and $\langle \hat{p}'^{out}_{L,sin,a+} \rangle$ we also define

$$\langle \hat{p}'^{out}_{L,cos,-} \rangle \equiv \langle \hat{p}'^{out}_{L,cos} \rangle \quad , \tag{4.2.4.i}$$

$$\langle \hat{p}'^{out}_{L,sin,-} \rangle \equiv \langle \hat{p}'^{out}_{L,sin} \rangle \quad , \tag{4.2.4.j}$$

$$\langle \hat{p}'^{out}_{L,cos,a,-} \rangle \equiv \langle \hat{p}'^{out}_{L,cos,a} \rangle \quad , \tag{4.2.4.k}$$

$$\langle \hat{p}'^{out}_{L,sin,a,-} \rangle \equiv \langle \hat{p}'^{out}_{L,sin,a} \rangle \quad , \tag{4.2.4.l}$$

where $\langle \hat{p}'^{out}_{L,cos} \rangle$, $\langle \hat{p}'^{out}_{L,sin} \rangle$, $\langle \hat{p}'^{out}_{L,cos,a} \rangle$ and $\langle \hat{p}'^{out}_{L,sin,a} \rangle$ are given by eqs. (4.2.3.a), (4.2.3.b), (4.2.4.a) and (4.2.4.b), respectively.

Note that we will say that eqs. (4.2.4.e-f) and (4.2.4.i-j) refer to a case, where the atomic ensemble and the membrane resonator are both "turned on".

In figures 21, 22 and 23 we can see experimental data obtained using the atom-membrane interfacing experimental setup seen in figure 20. This kind of data can show us how good we are at matching the atomic and the membrane resonator parameters. The kind of measurements that provide the data seen in these figures define the very first steps on our quest towards atom-membrane entanglement. The measurements were not performed on the same day, and they were also performed with different settings as the idea is to find out which settings can best minimize the mismatch between the atomic and the membrane resonator parameters. The common feature of these measurements is that the membrane resonator was not cooled.

For the data seen in figure 21 the probe laser power $P_{Probe,a}$ that the atoms were subjected to was $P_{Probe,a} = 0.600$ mW, and the probe laser power $P_{Probe,m}$ that the membrane resonator was subjected to was $P_{Probe,m} = 0.174$ mW. Here the probe laser was running in a continuous regime and the EOM was being switched on and off to produce the classical Ω_L-sidebands; the on-off switching time period was 0.100 ms long.

For the data seen in figure 22 $P_{Probe,a} = 0.120$ mW, and $P_{Probe,m} = 0.006$ mW. Here the probe laser was running in a continuous regime and the EOM was being switched on and off to produce the classical Ω_L-sidebands; the on-off switching time period was 0.100 ms long.

For the data seen in figure 23 $P_{Probe,a} = 0.122$ mW, and $P_{Probe,m} = 0.003$ mW. A data point on the graphs seen in figure 23 at one specific angular frequency was obtained by setting the EOM to produce sidebands of that specific angular frequency, then sending a large amount of pulses of probe laser light each being 0.100 ms long and finally averaging the data.

Note that in figures 22 and 23 we make use of the following definition:

$$m_{data,*} \equiv \sqrt{\langle \hat{p}'^{out}_{L,cos,*} \rangle^2 + \langle \hat{p}'^{out}_{L,sin,*} \rangle^2} \quad , \tag{4.2.5}$$

where * = −, +, m, and a,− and a,+; such that $m_{data,a,-}$ refers to a case, where the membrane resonator is "turned off" and the atoms reside in $|4,4>$, $m_{data,a,+}$ refers to a case, where the membrane resonator is "turned off" and the atoms reside in $|4,-4>$, $m_{data,m}$ refers to a case, where the atomic ensemble is "turned off", $m_{data,-}$ refers to a case, where both the atomic ensemble and the membrane resonator are "turned on" and the atoms reside in $|4,4>$, and $m_{data,+}$ refers to a case, where both the atomic ensemble and the membrane resonator are "turned on" and the atoms reside in $|4,-4>$.

In figure 21 we see that by taking the mean values of the experimental data, i.e. $\langle \hat{p}'^{out}_{L,cos,a} \rangle$, $\langle \hat{p}'^{out}_{L,sin,a} \rangle$, $\langle \hat{p}'^{out}_{L,cos,m} \rangle$ and $\langle \hat{p}'^{out}_{L,sin,m} \rangle$, to be where the fitted bell-shaped curves are at their highest, the mean values corresponding to the *coherent* cases become shifted further away from the zero-mean compared to the *thermal* cases. Observing the coherent cases, we see that in the atomic case the mean values are shifted away from the zero-mean on the order of 10^{-4}, while in the membrane case the shift is on the order of 10^{-3}. Since the difference in the shifts is on the order of 10, we conclude that the data presented here indicates that the atomic and the membrane resonator parameter matching is of poor quality.

In figure 22 we see that the measured values for $m_{data,a,-}$ and $m_{data,m}$ are shifted away from zero on the same order, and that the measured values for $m_{data,+}$ are further away from zero than the measured values for $m_{data,-}$. We observe that the measured values for $m_{data,-}$ become the ones that are closest to zero as the averaging progresses. Observing the definition of $m_{data,-}$ given by eq. (4.2.5), we see that this demonstrates that by coupling the two systems, when the atomic ensemble is modeled as a negative-mass harmonic oscillator and the membrane resonator is modeled as positive-mass harmonic oscillator, classical light back-action noise of the measurement becomes reduced. We also observe that the measured values for $m_{data,+}$ are furthest away from zero. This makes good sense, because according to the definition of $m_{data,+}$ given by eq. (4.2.5) $m_{data,+}$ refers to a case, where both the atomic ensemble and the membrane resonator are modeled as positive-mass harmonic oscillators.

In figure 23 we see that $m_{data,*}$, where * = −, +, m, and a,− and a,+, are largest close to the Larmor frequency $\Omega_L = 610$ kHz and become progressively smaller for frequencies smaller or larger than Ω_L in a Lorentzian fashion. This is expected, because from section 2.1 we know that the atoms and the membrane resonator are modeled as harmonic oscillators, and from section 2.1 we know that the atoms will show significant response at Ω_L, and from section 4.1 we know that the membrane resonator is designed such that it would show significant response at Ω_L. We observe that the area corresponding to $m_{data,-}$ is the smallest. Observing the definition of $m_{data,-}$, we see that again, as in the case of figure 22, this demonstrates that by coupling the two systems, when the atomic ensemble is modeled as a negative-mass harmonic oscillator and the membrane resonator is modeled as positive-mass harmonic oscillator, classical light back-action noise of the measurement becomes reduced. We also observe that the area corresponding to $m_{data,+}$ is the largest. This is attributed to the same reasons as in the case of figure 22.

Now, let us look at the atomic and the membrane resonator parameter matching condition expressed by eq. (2.1.11.a), and write it out completely by using the definitions $\kappa \equiv -a\sqrt{C_{ph,t}C_{a,t}\tau}$ and $g_{m,c} \equiv \hbar\sqrt{\frac{1}{m_{eff}\Omega_m}}G\bar{\alpha}_c$ seen in sections 1.4.5 and 1.6.4, respectively:

$$\kappa\sqrt{\frac{2}{\tau}} = g_{m,c}\sqrt{\frac{2}{\eta_c}} \quad <=>$$
$$\frac{\xi\lambda_{D2}^2}{16\pi A\Delta_5}\sqrt{C_{ph,t}C_{a,t}} = G\bar{\alpha}_c\sqrt{\frac{1}{\eta_c\Omega_m}} \quad , \tag{4.2.6}$$

where the definition $a \equiv -\frac{\xi\lambda_{D2}^2}{16\pi A\Delta_5}$ is seen in section 1.4.4, and $\hbar = m_{eff} = 1$ is assumed for $g_{m,c}$.

The parameters seen in eq. (4.2.6) that we cannot tweak are $\xi \equiv 2\pi \cdot 5.22$ MHz, which is the natural FWHM line width of the D_2 line transition (in units of radians per time), and $\lambda_{D2} = 852$ nm, which is the wavelength of the D_2 line transition. By recalling what the remaining parameters in eq. (4.2.6) stand for, we see that a perfect matching of the atomic and the membrane resonator parameters is an extremely challenging task.

From section 2.2 we understand that matching of the atomic and the membrane resonator parameters is not a requirement for generating entanglement between the atoms and the membrane resonator, because the EPR variance $\sum_{EPR}$ given by eq. (2.1.19) will due to the atomic and the membrane resonator parameter mismatch become $\sum_{EPR} \rightarrow \sum_{EPR} + [\epsilon\kappa(\bar{n}_{th} + 2)]^2$ such that entanglement still can be achieved even though the atomic and the membrane resonator parameters are mismatched under the condition that membrane resonator has to be cooled. Since from eq. (4.2.6) we can tell that it is extremely challenging to perfectly match the atomic and the membrane resonator parameters, we see that the membrane resonator *will* have to be cooled in order to achieve entanglement. As understood from section 2.2 an additional thing that we need to take into account if we want to achieve entanglement, apart from cooling the membrane resonator, is the thermalization decay of the membrane resonator, which modifies the EPR variance $\sum_{EPR}$ given by eq. (2.1.19) as $\sum_{EPR} \rightarrow \sum_{EPR} + \eta_m\tau(\bar{n}_{th} + 1)$, such that the practical requirement for the time period $t_1 \approx \tau$ of the protocol becomes $\tau \ll \frac{1}{\eta_m\bar{n}_{th}} = \frac{Q_m\hbar}{k_BT}$.

Our task for the future is thus to find the settings under which we may conclude that the mismatch between the atomic and the membrane resonator parameters is *reasonably* minimized, and then the membrane resonator will be cooled and the measurements will have to be performed much faster than $\frac{Q_m\hbar}{k_BT}$ in order to try to prove entanglement generation between Cesium-133 atoms and the membrane resonator.

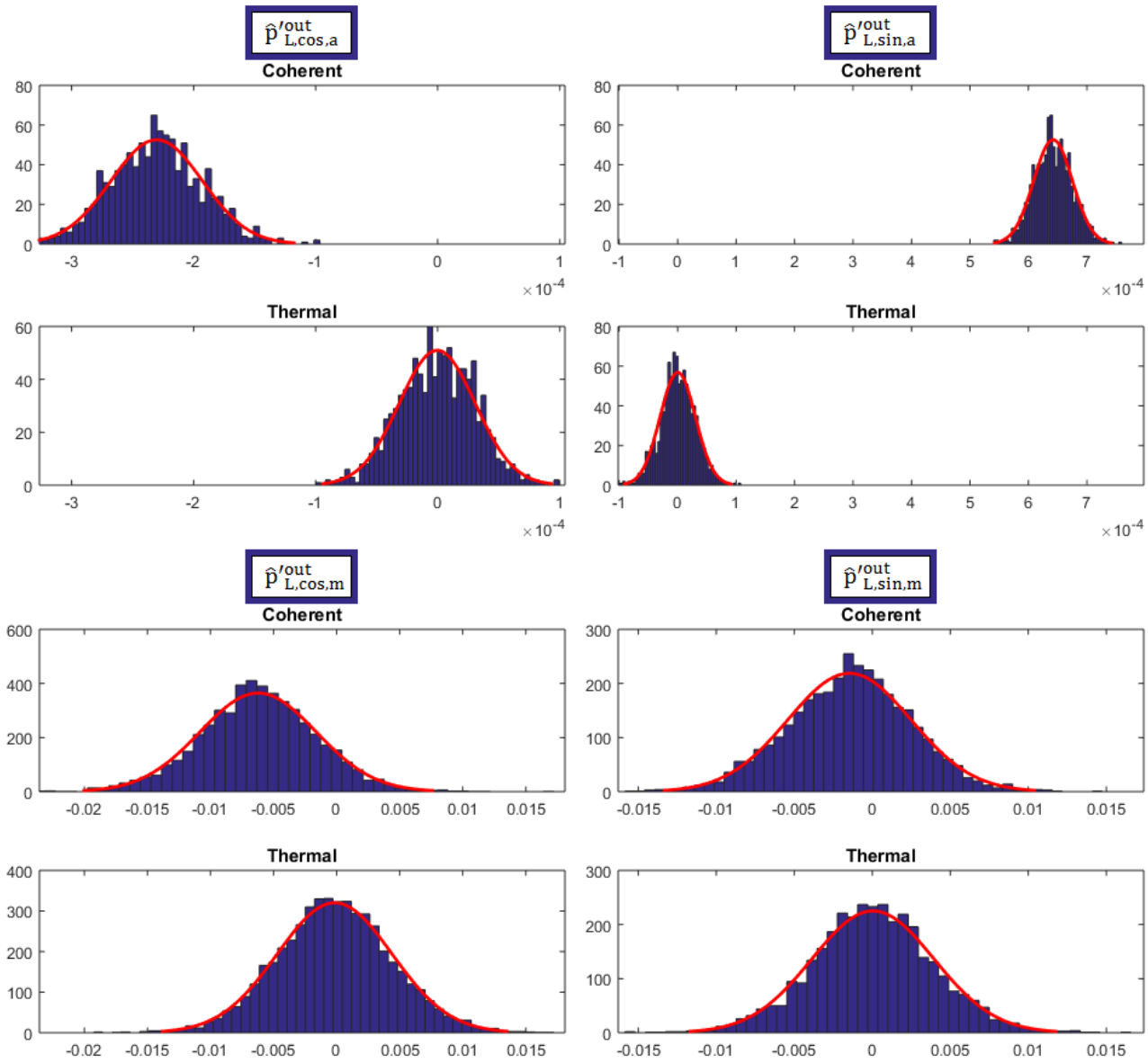

Figure 21. Histograms obtained by measuring the quantum operators $\hat{p}'^{out}_{L,cos,a}$, $\hat{p}'^{out}_{L,sin,a}$, $\hat{p}'^{out}_{L,cos,m}$ and $\hat{p}'^{out}_{L,sin,m}$ in respective cases, where the electro-optic modulator (EOM) in the atom-membrane interfacing setup is producing the classical Ω_L-sidebands, i.e. the *coherent* case in the figure, and not producing these sidebands, i.e. the *thermal* case in the figure. The data appears to be normally distributed and thus red bell-shaped curves are fitted on top of the histograms.

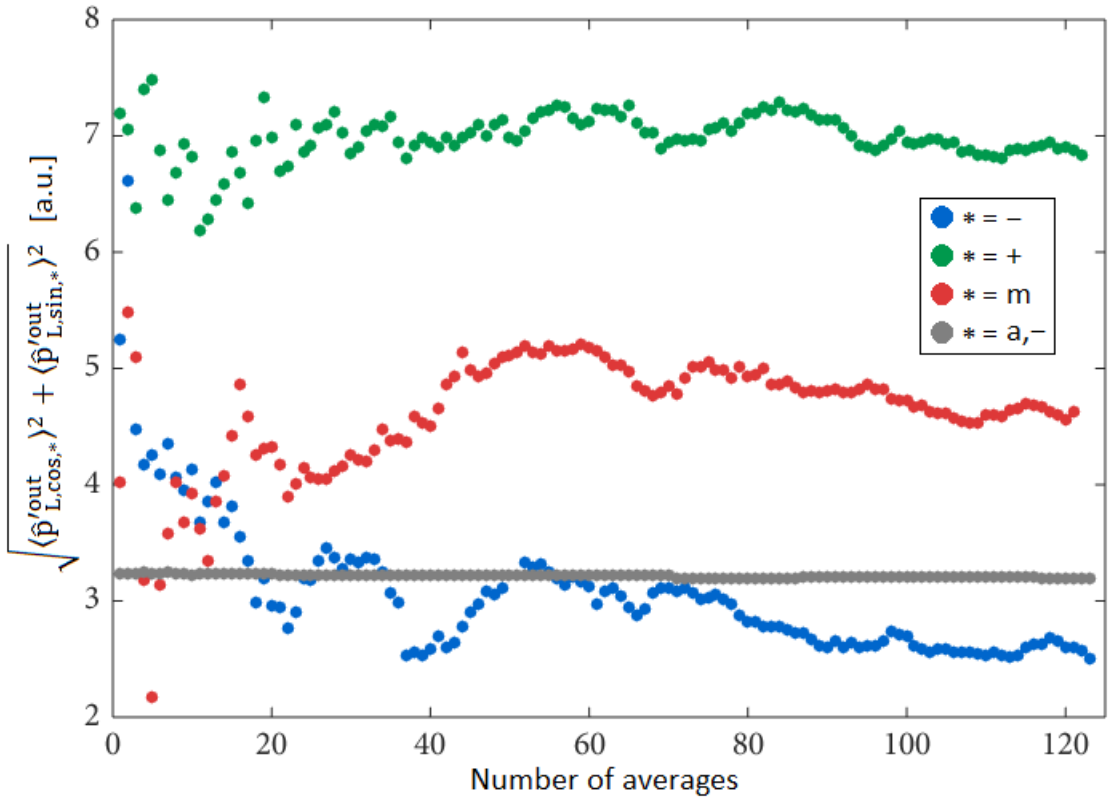

Figure 22. Experimentally obtained data points, seen as blue, green, red and grey dots, showing how $m_{data,*} \equiv \sqrt{\langle \hat{p}'^{out}_{L,cos,*} \rangle^2 + \langle \hat{p}'^{out}_{L,sin,*} \rangle^2}$, where * = –, +, m and a,–, change as the older data becomes averaged with the newer data in a case, where the electro-optic modulator (EOM) in the atom-membrane interfacing setup is producing the classical Ω_L-sidebands.

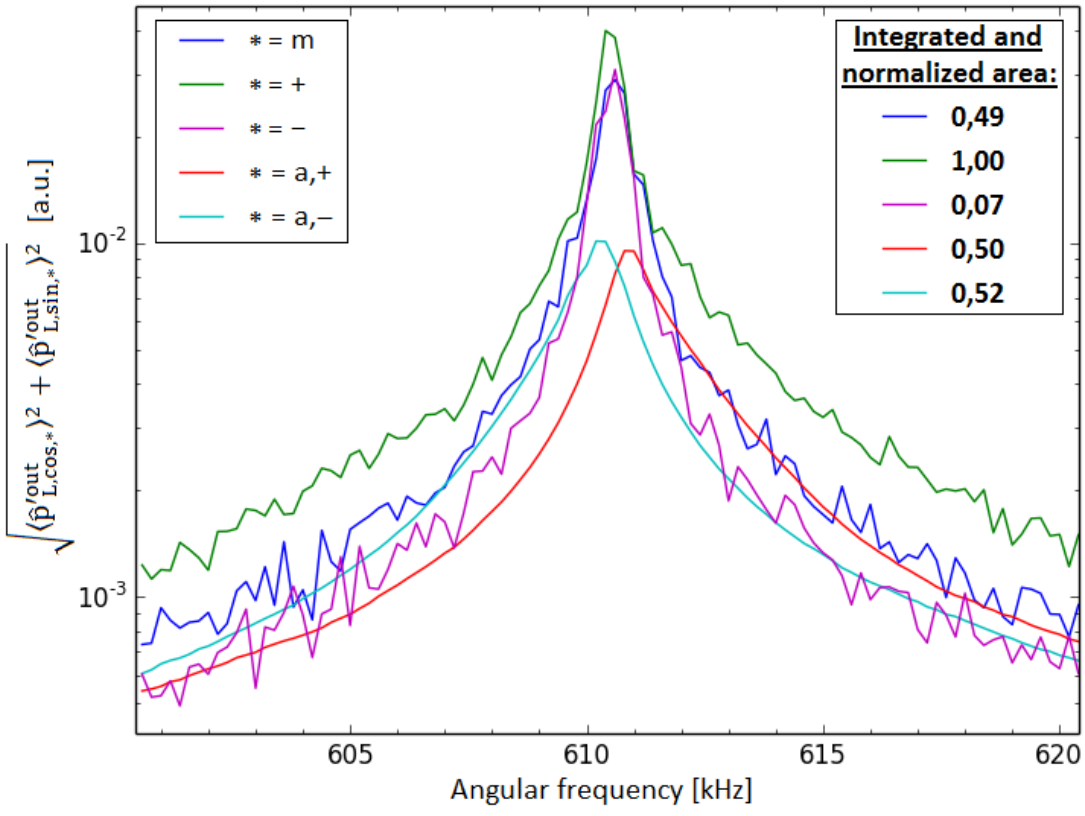

Figure 23. Experimentally obtained graphs, seen as dark blue, green, violet, and red and light blue lines, showing how $m_{data,*} \equiv \sqrt{\langle \hat{p}'^{out}_{L,cos,*} \rangle^2 + \langle \hat{p}'^{out}_{L,sin,*} \rangle^2}$, where * = m, +, − and a,− and a,+, respectively vary with different frequencies of the classical sidebands that the electro-optic modulator (EOM) in the atom-membrane interfacing setup is producing. The different graphs are integrated over angular frequency and the areas that are obtained by integrating and normalizing to unity are seen in the legend.

Summary of the main results and outlook

By making use of experimental data and parameters that characterize our atom-membrane entanglement experiment values for κ^2 were estimated for the case of our atom-membrane interfacing experimental setup. Assuming that these estimates are correct, they show us that in the case of our atom-membrane interfacing experimental setup we can obtain moderate values of $\kappa^2 \lesssim 0.25$ noted in the atom-membrane entanglement proposal [12].

By considering the dominant impairing effects that would alter the expression for the reduced EPR variance $\sum_{EPR}$ given by eq. (2.1.19), we saw that by minimizing the atomic and the membrane parameter mismatch as much as possible we could lower the practical limit imposed on the initial thermal occupation of the membrane resonator. We saw both theoretically and experimentally how classical Ω_L-sidebands introduce classical light back-action noise into our measurements. By cancelling this noise we can match the atomic and the membrane resonator parameters. It was demonstrated how by coupling the two systems we were led to reduction of classical light back-action noise of the measurement.

The measurements involving the reduction of classical light back-action noise of the measurement define the very first steps on our quest towards atom-membrane entanglement. The next steps of the experiment are in the order as follows: (i) doing the same measurements but with the membrane resonator now cooled, (ii) improving the membrane resonator and performing the same measurements, where the membrane resonator is first not cooled and then cooled, and finally (iii) characterizing how close to the standard quantum limit we are.

When and if the entanglement generation is successful, it can then serve as a basis for teleporting collective spin states onto the membrane resonator [12]. This can open a curious possibility to cool the membrane resonator by teleporting a ground state onto it.

Appendix A: The effect of an externally applied static magnetic field on a Cesium-133 atom and quadratic Zeeman splitting frequency

The effect of an externally applied static magnetic field **B** on an alkali atom such as a Cesium-133 atom is described by the Hamiltonian

$$\hat{H}_B = \hat{H}_{HFS} + \hat{H}_Z \quad , \tag{A.1}$$

where

$$\hat{H}_{HFS} = hA_{HFS}\hat{\mathbf{j}} \bullet \hat{\mathbf{i}} \quad , \tag{A.2.a}$$

$$\hat{H}_Z = -\left(\frac{\mu_J}{j}\hat{\mathbf{j}} \bullet \mathbf{B} + \frac{\mu_I}{I}\hat{\mathbf{i}} \bullet \mathbf{B}\right) \tag{A.2.b}$$

are the hyperfine structure interaction Hamiltonian and the Zeeman interaction Hamiltonian, respectively, where h is the Planck's constant, A_{HFS} is the zero-magnetic field hyperfine structure constant describing the strength of the magnetic interaction between the electron total angular momentum operator $\hat{\mathbf{j}}$ and the nuclear total angular momentum operator $\hat{\mathbf{i}}$, μ_J is the magnetic moment of the valence electron and μ_I is the magnetic moment of the nucleus.

Using $\hat{H}_B$ in eq. (A.1) it can be shown that the energy of a Zeeman energy level m_f for the ground state of (the valence electron of) an alkali atom, where $f = j \pm I = \frac{1}{2} \pm I$, will be given by *the Breit-Rabi formula* [25]:

$$E_{f,m_f} = -\frac{h\nu_{HFS}}{2(2I+1)} - \frac{\mu_I}{I}Bm_f \pm \frac{h\nu_{HFS}}{2}\sqrt{1 + \frac{4m_f}{2I+1}x + x^2} \quad , \tag{A.3}$$

where $B = |\mathbf{B}|$ is the strength of $\mathbf{B}$, $\nu_{HFS} \equiv \frac{A_{HFS}}{2}(2I+1)$ is the hyperfine structure splitting frequency between the two f-levels, and $x \equiv \frac{\left(-\frac{\mu_J}{j}+\frac{\mu_I}{I}\right)B}{h\nu_{HFS}}$ is a parameter describing the relative strength between the Zeeman interaction and the hyperfine structure interaction.

In figure A1 the frequency $E_{f,m_f}/h$ is plotted for the Zeeman energy levels m_f of the energy levels $6^2S_{1/2}$, f = 3 and $6^2S_{1/2}$, f = 4 of Cesium-133 atom as a function of B.

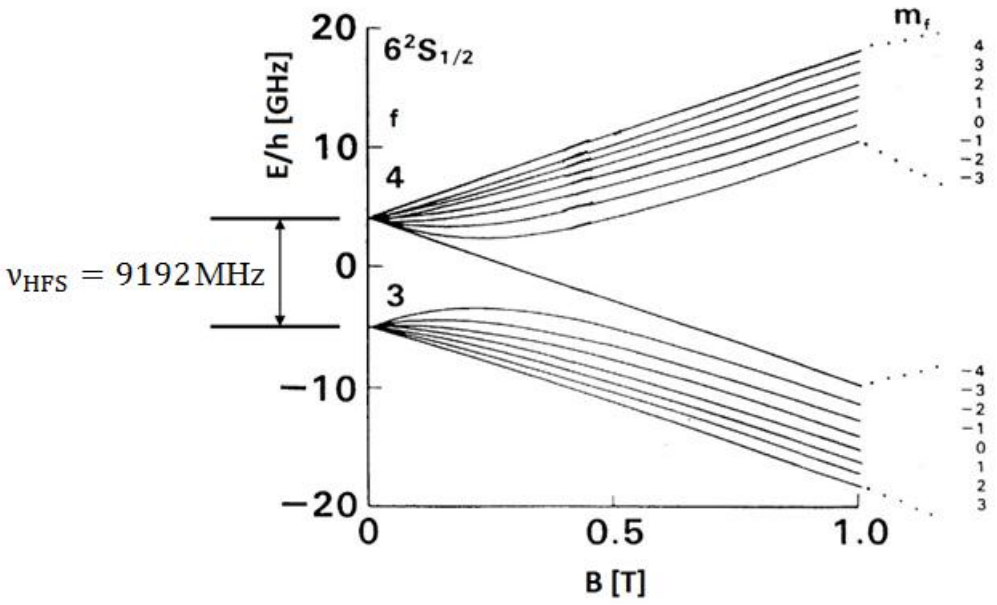

Figure A1. Graphs showing how the Zeeman energy levels m_f of the energy levels $6^2S_{1/2}$, f = 3 and $6^2S_{1/2}$, f = 4 of Cesium-133 atom are split in frequency for a given external static magnetic field strength B. Eq. (A.3) is used here in order to plot the different graphs. We see that for both small B (< 0,05 Tesla) and large B (> 0,5 Tesla), the frequencies display an approximately linear behavior with respect to B, whereas in the intermediate region the frequencies display a non-linear behavior with respect to B. The hyperfine structure effect splits the energy levels $6^2S_{1/2}$, f = 3 and $6^2S_{1/2}$, f = 4 by $\nu_{HFS} = 9192$ MHz in frequency as displayed in the figure. The figure is adapted from [11].

By performing the second order expansion of E_{f,m_f} in eq. (A.3) with the approximation $\mu_I = 0$, it can be shown that the transition frequency between the m_f'th and the $(m_f + 1)$'th Zeeman level of Cesium-133 atom is

$$\frac{E_{m_f+1} - E_{m_f}}{h} = \nu_L \left(1 - \frac{\nu_L}{\nu_{HFS}}(2m_f + 1)\right) \quad , \tag{A.4}$$

where $\nu_L \propto B$, where $\Omega_L \equiv 2\pi\nu_L$ is the Larmor frequency, which is the characteristic angular frequency at which the atomic total angular momentum vector operator $\hat{\mathbf{f}} = \hat{\mathbf{j}} + \hat{\mathbf{i}}$ will precess around the direction of the external **B**-field. From eq. (A.4) we have that the frequency difference between the two closest sets of two nearby $m_f -$ lines in figure A1 is

$$\nu_{QZ} \equiv \frac{E_{m_f+2} - E_{m_f+1}}{h} - \frac{E_{m_f+1} - E_{m_f}}{h} = \frac{2{\nu_L}^2}{\nu_{HFS}} \quad , \tag{A.5}$$

which is known as *the quadratic Zeeman splitting frequency*. ν_{QZ} is of importance in the magneto-optical resonance signal (MORS) measurements described in section 3.2.4.

Appendix B: The effect of an externally applied arbitrary magnetic field on Cesium-133 atoms, the Bloch equations and the phenomenological relaxation times T_1 and T_2

When Cesium-133 atoms sense an externally applied arbitrary magnetic field $\mathbf{B}(t) = (B_x(t), B_y(t), B_z(t))$, the evolution of the total angular momentum operators $\hat{J}_x(t)$, $\hat{J}_y(t)$, $\hat{J}_z(t)$ can be understood from the phenomenological rate equations know as *the Bloch equations* [29]:

$$\frac{d}{dt}M_x(t) = \gamma(\mathbf{M}(t) \times \mathbf{B}(t))_x - \frac{M_x(t)}{T_2} \quad , \tag{B.1.a}$$

$$\frac{d}{dt}M_y(t) = \gamma(\mathbf{M}(t) \times \mathbf{B}(t))_y - \frac{M_y(t)}{T_2} \quad , \tag{B.1.b}$$

$$\frac{d}{dt}M_z(t) = \gamma(\mathbf{M}(t) \times \mathbf{B}(t))_z - \frac{M_z(t)-M_0}{T_1} \quad , \tag{B.1.c}$$

where $\mathbf{M}(t) = (M_x(t), M_y(t), M_z(t))$ is the nuclear magnetization vector, M_0 is the steady-state nuclear magnetization, γ is the gyromagnetic ratio, and T_1 and T_2 are the phenomenological relaxation times respectively describing the approach of the longitudinal magnetization $M_z(t)$ and the transverse magnetizations $M_x(t)$ and $M_y(t)$ to equilibrium.

The Bloch equations are used to describe the evolution of the nuclear magnetization vector **M**(t) for a given arbitrary magnetic field **B**(t). **M**(t) acts as a classical analogue to the atomic ensemble total angular momentum vector operator $\hat{\mathbf{J}}(t) = (\hat{J}_x(t), \hat{J}_y(t), \hat{J}_z(t))$; and in the quantum mechanical picture the relaxation times T_1 and T_2 refer to the relaxation times of $\hat{\mathbf{J}}(t)$. If the z-axis is the quantization-axis, then in this thesis T_1 will be referred to as *the spin-depolarization time* and T_2 will be referred to as *the transverse spin-coherence time*.

Appendix C: Balanced homodyne detection

In this appendix I briefly describe balanced homodyne detection, and explain how we can measure the pairs of light operators $\hat{x}_L^{out} \propto \hat{S}_z^{out}(t)$, $\hat{p}_L^{out} \propto \hat{S}_y^{out}(t)$ and $\hat{x}'^{out}_L$, $\hat{p}'^{out}_L$, introduced in sections 1.4.5 and 1.6.4, respectively, by using this type of detection.

Note that in appendix C we have that $\langle . \rangle$ refers to the mean value.

In figure C1 (a) we can see a diagrammatic representation of an experimental setup used to realize a *prototypical* balanced homodyne detection scheme [32].

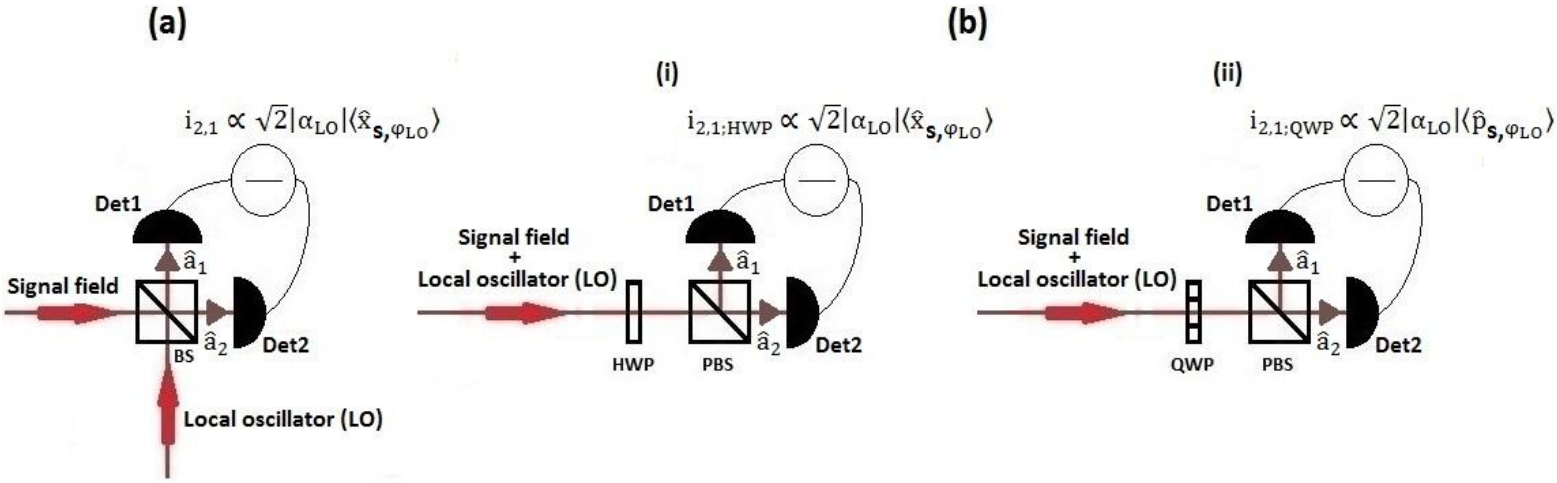

Figure C1. (a) A diagrammatic representation of an experimental setup used to realize a *prototypical* balanced homodyne detection scheme [32]. (b) (i) and (ii) Diagrammatic representations of experimental setups used to realize a balanced homodyne detection scheme in our experiments. In the figure we have that BS stands for beam splitter, PBS stands for polarizing beam splitter, HWP stands for half-wave plate, QWP stands for quarter-wave plate, and Det1 and Det2 are photodetectors**.** See the text for the remaining details.

Here a light field known as the signal field is described by the operators $\hat{x}_S \equiv \frac{1}{\sqrt{2}}\left(\hat{a}_S + \hat{a}_S^\dagger\right)$ and $\hat{p}_S \equiv \frac{1}{i\sqrt{2}}\left(\hat{a}_S - \hat{a}_S^\dagger\right)$, where $\hat{a}_S$ and $\hat{a}_S^\dagger$ are the photonic annihilation and creation operators of the signal field that are dimensionless and satisfy the commutation relation $\left[\hat{a}_S(t), \hat{a}_S^\dagger(t)\right] = 1$; and a light field known as the local oscillator (LO) is described by the operators $\hat{x}_{LO,\varphi_{LO}} \equiv \frac{1}{\sqrt{2}}\left(\hat{a}_{LO}e^{-i\varphi_{LO}} + \hat{a}_{LO}^\dagger e^{i\varphi_{LO}}\right)$ and $\hat{p}_{LO,\varphi_{LO}} \equiv \frac{1}{i\sqrt{2}}\left(\hat{a}_{LO}e^{-i\varphi_{LO}} - \hat{a}_{LO}^\dagger e^{i\varphi_{LO}}\right)$, where $\hat{a}_{LO}$ and $\hat{a}_{LO}^\dagger$ are the photonic annihilation and creation operators of the LO that are dimensionless and satisfy the commutation relation $\left[\hat{a}_{LO}(t), \hat{a}_{LO}^\dagger(t)\right] = 1$ with φ_{LO} denoting the phase the LO. Note that $\hat{x}_S$ and $\hat{p}_S$ are called the in-phase and the out-of-phase quadrature operators of the signal field, respectively; while $\hat{x}_{LO,\varphi_{LO}}$ and $\hat{p}_{LO,\varphi_{LO}}$ are called the rotated in-phase and out-of-phase quadrature

operators of the local oscillator, respectively [4]. After the two fields are superimposed at a 50/50 beam splitter, each outgoing beam from the beam splitter is respectively directed to the photodetectors Det1 and Det2, which provide us with the photocurrents i_1 and i_2, respectively; and in the final step, the photocurrents i_1 and i_2 are subtracted in order to yield the photocurrent $i_{2,1} \equiv i_2 - i_1$. The annihilation operators of the light fields directed at Det1 and Det2 are respectively given by

$$\hat{a}_1 = \frac{1}{\sqrt{2}}\left(\hat{a}_S - \hat{a}_{LO}e^{-i\varphi_{LO}}\right) \quad , \tag{C.1.a}$$

$$\hat{a}_2 = \frac{1}{\sqrt{2}}\left(\hat{a}_S + \hat{a}_{LO}e^{-i\varphi_{LO}}\right) \quad . \tag{C.1.b}$$

Assuming that i_1 and i_2 are respectively proportional to the classical mean values of the photon number operators $\hat{n}_1 = \hat{a}_1^\dagger\hat{a}_1$ and $\hat{n}_2 = \hat{a}_2^\dagger\hat{a}_2$, and that the LO is intense enough to be treated classically, i.e the quantum fluctuations of the LO can be neglected, such that $\hat{a}_{LO}^\dagger \to \langle\hat{a}_{LO}^\dagger\rangle = |\alpha_{LO}|$, $\hat{a}_{LO} \to \langle\hat{a}_{LO}\rangle = |\alpha_{LO}|$, where α_{LO} is a complex number, we have that $i_{2,1}$ becomes

$$i_{2,1} \propto \langle\hat{n}_2 - \hat{n}_1\rangle = \langle\hat{a}_2^\dagger\hat{a}_2 - \hat{a}_1^\dagger\hat{a}_1\rangle = \sqrt{2}|\alpha_{LO}|\langle\hat{x}_{S,\varphi_{LO}}\rangle = \sqrt{2}|\alpha_{LO}|\left(\langle\hat{x}_S\rangle\cos(\varphi_{LO}) + \langle\hat{p}_S\rangle\sin(\varphi_{LO})\right) \quad , \tag{C.2}$$

where $\hat{x}_{S,\varphi_{LO}} \equiv \frac{1}{\sqrt{2}}\left(\hat{a}_S e^{-i\varphi_{LO}} + \hat{a}_S^\dagger e^{i\varphi_{LO}}\right)$ is called the rotated in-phase quadrature operator of the signal field. Note that $\hat{p}_{S,\varphi_{LO}} \equiv \frac{1}{i\sqrt{2}}\left(\hat{a}_S e^{-i\varphi_{LO}} - \hat{a}_S^\dagger e^{i\varphi_{LO}}\right)$ is called the rotated out-of-phase quadrature operator of the signal field.

Observing eq. (C.2) we see that the photocurrent $i_{2,1}$ measures (the mean value of) the quadrature operator $\hat{x}_{S,\varphi_{LO}}$; and by adjusting the LO phase φ_{LO} to be $\varphi_{LO} = 0$, then $i_{2,1}$ will measure the in-phase quadrature operator $\hat{x}_S$, and if $\varphi_{LO} = \pi/2$, then $i_{2,1}$ will measure the out-of-phase quadrature operator $\hat{p}_S$.

Let us now understand how we can measure the pairs of light operators $\hat{x}_L^{out} \propto \hat{S}_z^{out}(t)$, $\hat{p}_L^{out} \propto \hat{S}_y^{out}(t)$ and $\hat{x}'^{out}_L$, $\hat{p}'^{out}_L$, introduced in sections 1.4.5, and 1.6.4, respectively, by using balanced homodyne detection scheme.

From eqs. (1.4.5.1.c-d) and (1.4.5.2.a-c) it follows that the scaled Stokes operators $\hat{x}_L^{out} \propto \hat{S}_z^{out}(t)$, $\hat{p}_L^{out} \propto \hat{S}_y^{out}(t)$ can respectively be written as

$$\hat{x}_L^{out} = \frac{1}{\sqrt{2}}(\hat{a}_y^{out} + \hat{a}_y^{out\dagger}) \quad , \tag{C.3.a}$$

$$\hat{p}_L^{out} = \frac{1}{i\sqrt{2}}(\hat{a}_y^{out} - \hat{a}_y^{out\dagger}) \quad , \tag{C.3.b}$$

[4] The quadrature operators $\hat{x} = \frac{1}{\sqrt{2}}\left(\hat{a} + a^\dagger\right)$ and $\hat{p} = \frac{1}{i\sqrt{2}}\left(\hat{a} - a^\dagger\right)$ represent the real and imaginary component of the photonic annihilation operator $\hat{a}$, respectively, because, by definition, we have $\frac{1}{\sqrt{2}}\left(\hat{a} + a^\dagger\right) = \mathrm{Re}(\hat{a})$ and $\frac{1}{i\sqrt{2}}\left(\hat{a} - a^\dagger\right) = \mathrm{Im}(\hat{a})$.

where $\hat{a}_y^{out} \equiv \hat{a}_y(x = L, t)$ and $\hat{a}_y^{out\dagger} \equiv \hat{a}_y^{\dagger}(x = L, t)$ are the photonic annihilation and creation operators for y-polarized probe laser light photons at the end of the Cesium-133 sample of length L, respectively.

Note that if in eqs. (1.4.5.1.c-d) it is assumed that the operators $\hat{a}_z^{\dagger}(x, t) \rightarrow \langle \hat{a}_z^{\dagger}(x, t) \rangle = |\alpha_z(x, t)|$, $\hat{a}_z(x, t) \rightarrow \langle \hat{a}_z(x, t) \rangle = |\alpha_z(x, t)|$, then

$$\hat{S}_x(t) \rightarrow \frac{|\alpha_z(x,t)|^2}{2} \quad , \tag{C.4.a}$$

$$\hat{S}_y(t) \rightarrow \frac{|\alpha_z(x,t)|}{2}(\hat{a}_y^{\dagger}(x, t) + \hat{a}_y(x, t)) \quad , \tag{C.4.b}$$

$$\hat{S}_z(t) \rightarrow \frac{|\alpha_z(x,t)|}{2i}(\hat{a}_y^{\dagger}(x, t) - \hat{a}_y(x, t)) \quad ; \tag{C.4.c}$$

such that $\left[\frac{\hat{S}_y(t)}{\sqrt{S_x}}, \frac{\hat{S}_z(t)}{\sqrt{S_x}}\right] = \left[p_{L;new}(x, t), x_{L;new}(x, t')\right] = i\delta(t - t')$, where $p_{L;new}(x, t) \equiv \frac{\hat{S}_y(t)}{\sqrt{S_x}}$ with $\hat{S}_y(t)$ in eq. (C.4.b), and $x_{L;new}(x, t) \equiv \frac{\hat{S}_z(t)}{\sqrt{S_x}}$ with $\hat{S}_z(t)$ in eq. (C.4.c), and so

$$\hat{p}_{L;new}^{out} = \frac{1}{\sqrt{2}}(\hat{a}_y^{out} + \hat{a}_y^{out\dagger}) \quad , \tag{C.5.a}$$

$$\hat{x}_{L;new}^{out} = \frac{1}{i\sqrt{2}}(\hat{a}_y^{out} - \hat{a}_y^{out\dagger}) \quad , \tag{C.5.b}$$

where $\hat{p}_{L;new}^{out} \equiv p_{L;new}(x = L, t)$, $\hat{x}_{L;new}^{out} \equiv x_{L;new}(x = L, t)$.

The difference between eqs. (C.3.a-b) and (C.5.a-b) is that in eqs. (C.3.a-b) the signal field and the LO are assumed to acquire a phase of $e^{\frac{i\pi}{2}} = i$, whereas in eqs. (C.5.a-b) the signal field and the LO are assumed do not acquire a phase. The phase of $e^{\frac{i\pi}{2}} = i$ is acquired, because in eqs. (1.4.5.2.a-c) we have that the operators $\hat{a}_z(x, t) \rightarrow \langle \hat{a}_z(x, t) \rangle = i|\alpha_z(x, t)|$, $\hat{a}_z^{\dagger}(x, t) \rightarrow \langle \hat{a}_z^{\dagger}(x, t) \rangle = -i|\alpha_z(x, t)|$, whereas in eqs. (C.4.a-c) we have $\hat{a}_z(x, t) \rightarrow \langle \hat{a}_z(x, t) \rangle = |\alpha_z(x, t)|$, $\hat{a}_z^{\dagger}(x, t) \rightarrow \langle \hat{a}_z^{\dagger}(x, t) \rangle = |\alpha_z(x, t)|$.

Now, since from section 1.6.4 we have that the operators $\hat{x}_L'(x) = \hat{x}_L'(x, t)$ and $\hat{p}_L'(x) = \hat{p}_L'(x, t)$ satisfy the canonical commutation relation $[\hat{x}_L'(x, t), \hat{p}_L'(x, t')] = i\delta(t - t')$ for $\hbar = 1$, which, as we observe, is also the case for the scaled Stokes operators $\hat{x}_L(x)$ and $\hat{p}_L(x)$ defined in eqs. (1.4.5.1.c) and (1.4.5.1.d), respectively, then the operators $\hat{x}_L'^{out}$ and $\hat{p}_L'^{out}$ that describe the light that is transmitted by a cavity optomechanical system can respectively be written as

$$\hat{x}_L'^{out} = \frac{1}{\sqrt{2}}(\hat{a}'^{out} + \hat{a}'^{out\dagger}) \quad , \tag{C.6.a}$$

$$\hat{p}_L'^{out} = \frac{1}{i\sqrt{2}}(\hat{a}'^{out} - \hat{a}'^{out\dagger}) \quad , \tag{C.6.b}$$

where $\hat{a}'^{out}$ and $\hat{a}'^{out\dagger}$ are the photonic annihilation and creation operators for the photons transmitted by a cavity optomechanical system, respectively.

Observing eqs. (C.3.a-b), (C.5.a-b) and (C.6.a-b) we see that the pairs of light operators $\hat{x}_L^{out} \propto \hat{S}_z^{out}(t)$, $\hat{p}_L^{out} \propto \hat{S}_y^{out}(t)$ and $\hat{x}'^{out}_L$, $\hat{p}'^{out}_L$ are quadrature operators of light; and thus, by observing eq. (C.2), we know that by subjecting light described by one of these pairs of quadrature operators to balanced homodyne detection as done in figure C (a), we can measure such one pair of quadrature operators.

We make use of balanced homodyne detection in the Cesium-133 atom sample characterization measurement experiment presented in section 3.2.4 and in the atom-membrane entanglement experiment described in chapter 4. The balanced homodyne detection scheme that we use in these experiments is different from the one seen in figure C1 (a). In the sample characterization measurement experiment presented in section 3.2.4 we make use of the balanced homodyne detection seen in figure C1 (b) (i), and in the atom-membrane entanglement experiment described in chapter 4 we make use of the balanced homodyne detection seen in figures C1 (b) (i) and C1 (b) (ii). Using these schemes one can also learn about the quadrature operator pairs $\hat{x}_L^{out} \propto \hat{S}_z^{out}(t)$, $\hat{p}_L^{out} \propto \hat{S}_y^{out}(t)$ and $\hat{x}'^{out}_L$, $\hat{p}'^{out}_L$.

In the scheme seen in figure C1 (b) (i) we replace the BS seen in figure C1 (a) with a PBS and place a half-wave plate before the PBS, and send the signal field and the LO into the same port of the PBS; the half-wave plate here is rotated such that the output modes have equal powers. The scheme in figure C1 (b) (ii) depicts a similar situation as figure C1 (b) (i), but here the half-wave plate is replaced with a quarter-wave plate; the quarter-wave plate here is rotated such that the output modes have equal powers.

Using the a balanced homodyne detection scheme in figure C1 (b) (i), the subtracted photocurrent

$$i_{2,1;HWP} \propto \sqrt{2}|\alpha_{LO}|\langle\hat{x}_{S,\varphi_{LO}}\rangle = \sqrt{2}|\alpha_{LO}|\big(\langle\hat{x}_S\rangle\cos(\varphi_{LO}) + \langle\hat{p}_S\rangle\sin(\varphi_{LO})\big) \quad , \qquad \text{(C.7.a)}$$

which is the same as in figure C1 (a); and in the case of figure C1 (b) (ii), the subtracted photocurrent

$$i_{2,1;QWP} \propto \sqrt{2}|\alpha_{LO}|\langle\hat{p}_{S,\varphi_{LO}}\rangle = \sqrt{2}|\alpha_{LO}|\big(\langle\hat{p}_S\rangle\cos(\varphi_{LO}) + \langle\hat{x}_S\rangle\sin(\varphi_{LO})\big) \quad . \qquad \text{(C.7.b)}$$

i.e a $\pi/2$-phase shift is introduced.

Note that in the aforementioned experiments, the LO is the probe laser light with the assumption that the quantum fluctuations of this light are neglected.

In the atom-membrane entanglement experiment we need to stabilize the phase φ_{LO} such that it is different from zero, i.e. $\varphi_{LO} \neq 0$. In chapter 4, where this experiment is described, we can see how we stabilize φ_{LO}.

Appendix D: Jones matrix calculus

In this appendix I present Jones matrix calculus formalism [33].

The Jones matrix calculus is used to describe how the polarization of light is transformed by polarizing optical components. The light is represented by a 2×1 matrix, known as the Jones vector, and the optical components are represented by 2×2 matrices, known as the Jones matrices. When light passes an optical component, the resulting polarization of the transmitted light is found by taking a matrix product between the Jones matrix of the optical component and the Jones vector of the incident light.

Note that Jones calculus only deals with light that is fully polarized; this makes Jones calculus applicable in our experiments, because as written in section 3.1.1 we probe the atoms with linearly-polarized light.

A Jones vector may in general be written as

$$\mathbf{V}_{\text{Jones}} \equiv \begin{bmatrix} E_H \\ E_V \end{bmatrix} = \begin{bmatrix} E_{0H} e^{i(\varphi_H - \omega t)} \\ E_{0V} e^{i(\varphi_V - \omega t)} \end{bmatrix} \quad , \tag{D.1}$$

where E_H and E_V are the (complex) horizontal and vertical polarization components, respectively, of the electric field $\mathbf{E}(x,t) = \mathbf{V}_{\text{Jones}} e^{ikx}$ of a monochromatic plane wave of light travelling along the x-axis, where k is the angular wave number and ω is the angular frequency of the light with $k = \omega/c$, and E_{0H} and E_{0V} are the amplitudes of respectively E_H and E_V with φ_H and φ_V being the respective phases. Note that we define the difference between the phases φ_H and φ_V as $\varphi \equiv \varphi_H - \varphi_V$.

Since $\mathbf{E}(x,t) = \mathbf{V}_{\text{Jones}} e^{ikx}$, then it follows that the intensity of the electric field $\mathbf{E}(x,t)$ is

$$I_{\mathbf{E}} = I_{\text{Jones}} \propto \mathbf{V}^*_{\text{Jones}} \bullet \mathbf{V}_{\text{Jones}} = \begin{bmatrix} \bar{E}_H & \bar{E}_V \end{bmatrix} \begin{bmatrix} E_H \\ E_V \end{bmatrix} = \bar{E}_H E_H + \bar{E}_V E_V \quad . \tag{D.2}$$

The Jones matrices that we use in this thesis are the following ones:

1. The Jones matrix for a rotator:

$$\bar{\bar{\mathbf{M}}}_R(\theta) = \begin{bmatrix} \cos(\theta) & \sin(\theta) \\ -\sin(\theta) & \cos(\theta) \end{bmatrix} \quad , \tag{D.3.a}$$

2. The Jones matrix for a rotated wave plate:

$$\bar{\bar{\mathbf{M}}}_{RWP}(\varphi, \theta) = \bar{\bar{\mathbf{M}}}_R(-\theta) \begin{bmatrix} 1 & 0 \\ 0 & e^{-i\varphi} \end{bmatrix} \bar{\bar{\mathbf{M}}}_R(\theta) \quad , \tag{D.3.b}$$

3. The Jones matrix for a perfect linear polarizer:

$$\bar{\bar{\mathbf{M}}}_{LPOL}(p_H, p_V) = \begin{bmatrix} p_H & 0 \\ 0 & p_V \end{bmatrix} \quad , \tag{D.3.c}$$

4. The Jones matrix for a piezoelectric-actuated mirror:

$$\bar{\bar{\mathbf{M}}}_{\mathrm{PAM}}\left(\varphi_{\mathrm{H}} \rightarrow \varphi_{\mathrm{H},*}(\mathrm{t}), \varphi_{\mathrm{V}} \rightarrow \varphi_{\mathrm{V},*}(\mathrm{t})\right) \quad . \tag{D.3.d}$$

In eqs. (D.3.a-d) θ is the angle of the fast axis of a wave plate with respect to the horizontal axis; $\varphi \equiv \varphi_{\mathrm{H}} - \varphi_{\mathrm{V}}$; $\mathrm{p_H}, \mathrm{p_V} = 0$ or 1; and $\bar{\bar{\mathbf{M}}}_{\mathrm{PAM}}\left(\varphi_{\mathrm{H}} \rightarrow \varphi_{\mathrm{H},*}(\mathrm{t}), \varphi_{\mathrm{V}} \rightarrow \varphi_{\mathrm{V},*}(\mathrm{t})\right)$ transforms the phases φ_{H} and φ_{V} in the Jones vector $\mathbf{V}_{\mathrm{Jones}}$ in eq. (D.1) into time dependent phases $\varphi_{\mathrm{H},*}(\mathrm{t})$ and $\varphi_{\mathrm{V},*}(\mathrm{t})$, respectively.

Appendix E: List of Jones matrices used in calculations

In this appendix we can see the Jones matrices used in the calculations performed in chapter 4, where it is explained why our atom-membrane interfacing experimental setup can allow us to satisfy the entanglement protocol described in chapter 2.

The Jones matrices for

1. the half-wave plates are:
$\bar{\bar{\mathbf{M}}}_{\mathrm{HWP1}} = \bar{\bar{\mathbf{M}}}_{\mathrm{HWP2}} \equiv \bar{\bar{\mathbf{M}}}_{\mathrm{LPOL}}(1,1) = \begin{bmatrix} 1 & 0 \\ 0 & 1 \end{bmatrix}$, $\bar{\bar{\mathbf{M}}}_{\mathrm{HWP3}} \equiv \bar{\bar{\mathbf{M}}}_{\mathrm{RWP}}(\pi, 0) = \begin{bmatrix} 1 & 0 \\ 0 & -1 \end{bmatrix}$, $\bar{\bar{\mathbf{M}}}_{\mathrm{HWP4}} = \bar{\bar{\mathbf{M}}}_{\mathrm{HWP5}} = \bar{\bar{\mathbf{M}}}_{\mathrm{HWP6}} = \bar{\bar{\mathbf{M}}}_{\mathrm{HWP7}} \equiv \bar{\bar{\mathbf{M}}}_{\mathrm{RWP}}(\pi, \pi/8) = \frac{1}{\sqrt{2}}\begin{bmatrix} 1 & 1 \\ 1 & -1 \end{bmatrix}$, $\bar{\bar{\mathbf{M}}}_{\mathrm{HWP8}} = \bar{\bar{\mathbf{M}}}_{\mathrm{HWP9}} \equiv \bar{\bar{\mathbf{M}}}_{\mathrm{RWP}}(\pi, \pi) = \begin{bmatrix} 0 & 1 \\ 1 & 0 \end{bmatrix}$, $\bar{\bar{\mathbf{M}}}_{\mathrm{HWP10}} \equiv \bar{\bar{\mathbf{M}}}_{\mathrm{RWP}}(\pi, 0) = \begin{bmatrix} 1 & 0 \\ 0 & -1 \end{bmatrix}$, $\bar{\bar{\mathbf{M}}}_{\mathrm{HWP11}} \equiv \bar{\bar{\mathbf{M}}}_{\mathrm{RWP}}(\pi, \pi/8) = \frac{1}{\sqrt{2}}\begin{bmatrix} 1 & 1 \\ 1 & -1 \end{bmatrix}$.

2. the quarter-wave plates are:
$\bar{\bar{\mathbf{M}}}_{\mathrm{QWP1}} = \bar{\bar{\mathbf{M}}}_{\mathrm{QWP2}} \equiv \bar{\bar{\mathbf{M}}}_{\mathrm{RWP}}(\pi/2, \pi/4) = \frac{1}{2}\begin{bmatrix} 1-\mathrm{i} & 1+\mathrm{i} \\ 1+\mathrm{i} & 1-\mathrm{i} \end{bmatrix}$, $\bar{\bar{\mathbf{M}}}_{\mathrm{QWP3}} \equiv \bar{\bar{\mathbf{M}}}_{\mathrm{LPOL}}(1,1) = \begin{bmatrix} 1 & 0 \\ 0 & 1 \end{bmatrix}$.

3. the polarizing beam splitters are:
$\bar{\bar{\mathbf{M}}}_{\mathrm{PBSj}} \equiv \bar{\bar{\mathbf{M}}}_{\mathrm{PBSj,tr}} + \bar{\bar{\mathbf{M}}}_{\mathrm{PBSj,r}} = \bar{\bar{\mathbf{M}}}_{\mathrm{LPOL}}(1,0) + \bar{\bar{\mathbf{M}}}_{\mathrm{LPOL}}(0,1) = \begin{bmatrix} 1 & 0 \\ 0 & 0 \end{bmatrix} + \begin{bmatrix} 0 & 0 \\ 0 & 1 \end{bmatrix}$, where $\bar{\bar{\mathbf{M}}}_{\mathrm{PBSj,tr}} \equiv \begin{bmatrix} 1 & 0 \\ 0 & 0 \end{bmatrix}$, $\bar{\bar{\mathbf{M}}}_{\mathrm{PBSj,r}} \equiv \begin{bmatrix} 0 & 0 \\ 0 & 1 \end{bmatrix}$, where $\mathrm{j} = 1, \ldots, 9$.

4. the electro-optic modulator is:
$\bar{\bar{\mathbf{M}}}_{\mathrm{EOM}} \equiv \bar{\bar{\mathbf{M}}}_{\mathrm{RWP}}\left(\beta_1 \cos\left(\Omega_{\beta_1}\mathrm{t}\right) + \beta_2 \cos(\Omega_{\mathrm{L}}\mathrm{t}), \frac{\pi}{4}\right) =$
$\bar{\bar{\mathbf{M}}}_{\mathrm{R}}\left(-\frac{\pi}{4}\right)\begin{bmatrix} 1 & 0 \\ 0 & \mathrm{e}^{-\mathrm{i}(\beta_1 \cos(\Omega_{\beta_1}\mathrm{t}) + \beta_2 \cos(\Omega_{\mathrm{L}}\mathrm{t}))} \end{bmatrix}\bar{\bar{\mathbf{M}}}_{\mathrm{R}}\left(\frac{\pi}{4}\right) \rightarrow$
$\bar{\bar{\mathbf{M}}}_{\mathrm{R}}\left(-\frac{\pi}{4}\right)\begin{bmatrix} 1 & 0 \\ 0 & 1 - \mathrm{i}\left(\beta_1 \cos\left(\Omega_{\beta_1}\mathrm{t}\right) + \beta_2 \cos(\Omega_{\mathrm{L}}\mathrm{t})\right) \end{bmatrix}\bar{\bar{\mathbf{M}}}_{\mathrm{R}}\left(\frac{\pi}{4}\right) =$
$\begin{bmatrix} 1 - \frac{\mathrm{i}\beta_1}{4}\left(\mathrm{e}^{\mathrm{i}\Omega_{\beta_1}\mathrm{t}} + \mathrm{e}^{-\mathrm{i}\Omega_{\beta_1}\mathrm{t}}\right) - \frac{\mathrm{i}\beta_2}{4}\left(\mathrm{e}^{\mathrm{i}\Omega_{\mathrm{L}}\mathrm{t}} + \mathrm{e}^{-\mathrm{i}\Omega_{\mathrm{L}}\mathrm{t}}\right) & \frac{\mathrm{i}\beta_1}{4}\left(\mathrm{e}^{\mathrm{i}\Omega_{\beta_1}\mathrm{t}} + \mathrm{e}^{-\mathrm{i}\Omega_{\beta_1}\mathrm{t}}\right) + \frac{\mathrm{i}\beta_2}{4}\left(\mathrm{e}^{\mathrm{i}\Omega_{\mathrm{L}}\mathrm{t}} + \mathrm{e}^{-\mathrm{i}\Omega_{\mathrm{L}}\mathrm{t}}\right) \\ \frac{\mathrm{i}\beta_1}{4}\left(\mathrm{e}^{\mathrm{i}\Omega_{\beta_1}\mathrm{t}} + \mathrm{e}^{-\mathrm{i}\Omega_{\beta_1}\mathrm{t}}\right) + \frac{\mathrm{i}\beta_2}{4}\left(\mathrm{e}^{\mathrm{i}\Omega_{\mathrm{L}}\mathrm{t}} + \mathrm{e}^{-\mathrm{i}\Omega_{\mathrm{L}}\mathrm{t}}\right) & 1 - \frac{\mathrm{i}\beta_1}{4}\left(\mathrm{e}^{\mathrm{i}\Omega_{\beta_1}\mathrm{t}} + \mathrm{e}^{-\mathrm{i}\Omega_{\beta_1}\mathrm{t}}\right) - \frac{\mathrm{i}\beta_2}{4}\left(\mathrm{e}^{\mathrm{i}\Omega_{\mathrm{L}}\mathrm{t}} + \mathrm{e}^{-\mathrm{i}\Omega_{\mathrm{L}}\mathrm{t}}\right) \end{bmatrix}$
, where the assumptions that β_1 and β_2 are small are made.

5. the piezoelectric-actuated mirrors are:
$\bar{\bar{\mathbf{M}}}_{\mathrm{PAM1}} \equiv \bar{\bar{\mathbf{M}}}_{\mathrm{PAM}}\left(\varphi_{\mathrm{H}} \rightarrow \varphi_{\mathrm{H},1}(\mathrm{t}) + \frac{\pi}{2}\right)$, $\bar{\bar{\mathbf{M}}}_{\mathrm{PAM2}} \equiv \bar{\bar{\mathbf{M}}}_{\mathrm{PAM}}\left(\varphi_{\mathrm{H}} \rightarrow \varphi_{\mathrm{H},3}(\mathrm{t})\right)$.

Bibliography

General sources and theory:

[1] B. Julsgaard, "Entanglement and quantum interactions with macroscopic gas samples", PhD thesis, University of Aarhus (2003).

[2] J. Sherson, "Quantum memory and teleportation using macroscopic gas samples", PhD thesis, University of Aarhus (2006).

[3] K. Jensen, "Quantum information, entanglement and magnetometry with macroscopic gas samples and non-classical light", PhD thesis, University of Copenhagen (2011).

[4] H. Krauter, "Generation and application of entanglement of room temperature ensembles of atoms", PhD thesis, University of Copenhagen (2011).

[5] A. Schliesser, "Cavity optomechanics and optical frequency comb generation with silica whispering-gallery-mode microresonators", PhD thesis, Ludwig Maximilian University of Munich (2009).

[6] H. Shen," Spin squeezing and entanglement with room temperature atoms for quantum sensing and communication", PhD thesis, University of Copenhagen (2014).

[7] G. Vasilakis, " Precision measurements of spin interactions with high density atomic vapors", PhD thesis, Princeton University (2011).

[8] A. Fabricant, "Quantum-limited optical magnetometry with cesium microcells", MSc thesis, University of Copenhagen (2014).

[9] W. Carlsen, "Cryogenic cavity optomechanics with ultrahigh-Q membrane resonators", MSc thesis, University of Copenhagen (2015).

[10] A. Barg, "Optical characterization of micromechanical membranes", MSc thesis, University of Copenhagen (2014).

[11] B. Julsgaard, J. Sherson, J. L. Sørensen, and E. S. Polzik, "Characterizing the spin state of an atomic ensemble using the magneto-optical resonance method", J. Opt. B: Quantum Semiclassical Opt. 6 (1), 5-14 (2004).

[12] K. Hammerer, M. Aspelmeyer, E. S. Polzik, and P.Zoller, "Establishing Einstein-Podolsky-Rosen channels between nanomechanics and atomic ensembles", Phys. Rev. Lett. 102 (2), 501-504 (2009).

[13] E. S. Polzik and K. Hammerer, "Trajectories without quantum uncertainties", Ann. Phys. 527, A15 (2015).

[14] M. Tsang and C. M. Caves, "Evading quantum mechanics: engineering a classical subsystem within a quantum environment", Phys. Rev. X 2, 031016 (2012).

[15] M. Bhattacharya, P.-L. Giscard, and P. Meystre, " Entanglement of a Laguerre-Gaussian cavity mode with a rotating mirror", arXiv:0710.0687v1 (2007).

[16] E. D. Black, "An introduction to PDH laser frequency stabilization", Am. J. Phys. 69 (1), 79-87 (2001).

[17] M. Aspelmeyer, T. J Kippenberg, and F. Marquardt, "Cavity optomechanics", Rev. Mod. Phys. 86, 1391 (2014).

[18] R. I. A. Davis, R. Delbourgo, and P. D. Jarvis, "Covariance, correlation and entanglement", arXiv:quant-ph/0001076v1 (2000).

[19] G. S. Agarwal and S. Chaturvedi, "Scheme to measure quantum Stokes parameters and their fluctuations and correlations", arXiv:quant-ph/0203050v2 (2002).

[20] M. V. Balabas, T. Karaulonov, M. P. Ledbetter, and D. Budker, "Polarized alkali-metal vapor with minute-long transverse spin-relaxation time", Phys. Rev. Lett. 105 (7), 801-804 (2010).

[21] R. Turner, "Gradient coil design: A review of methods", MRI 11 (7), 903-920 (1993).

[22] D. J. Griffiths, *Introduction to quantum mechanics* (Pearson Education, India, 2005).

[23] M. O. Scully and M. Suhail Zubairy, *Quantum optics* (Oxford U. P., Cambridge, 2002).

[24] H. Yokoyama and K. Ujihara, *Spontaneous emission and laser oscillation in microcavities* (CRC press, Florida, 1995).

[25] C. J. Foot, *Atomic physics* (Oxford U. P., New York, 2005).

[26] P. W. Milonni and J. H. Eberly, *Laser physics* (John Wiley & sons, New Jersey, 2010).

[27] R. E. Taylor, *Thermal expansion of solids* (ASM International, Ohio, 1998).

[28] D. Budker and D. F. Jackson Kimball, *Optical Magnetometry* (Cambridge U. P., Cambridge, 2013).

[29] L. Allen and J. H. Eberly, *Optical resonance and two-level atoms* (Dover Publications, New York, 1987).

[30] K. L. Kaiser, *Electromagnetic shielding* (CRC Press, Boca Raton, 2006).

[31] A. E. Siegman, *Lasers* (University Science Books, California, 1986).

[32] D. L. Andrews, *Fundamentals of photonics and physics: Volume I* (John Wiley & Sons, New Jersey, 2015).

[33] A. Rogers, *Polarization in optical fibers* (Artech House, Massachusetts, 2008).

[34] D. Jiles, *Introduction to magnetism and magnetic materials, Second edition* (CRC Press, Boca Raton, 1998).

[35] O. Schmidt, K. -M. Knaak, R. Wynands, and D. Meschede, "Cesium saturation spectroscopy revisited: how to reverse peaks and observe narrow resonances", Appl. Phys. B 59, 167 178 (1994).

[36] C. E. Wieman, *Collected papers of Carl Wieman* (World Scientific, Singapore, 2008).

[37] F. Ya. Khalili, "Quantum variational measurement in the next generation gravitational-wave detectors", Phys. Rev. D 76, 102002 (2007).

[38] M. A. Taylor, J. Janousek, V. Daria, J. Knittel, B. Hage, H.-A. Bachor, and W. P. Bowen, "Biological measurement beyond the quantum limit", Nature Photonics 7, 229–233 (2013).

[39] S. S. Szigeti, B. Tonekaboni, W. Y. S. Lau, S. N. Hood, and S. A. Haine, "Squeezed-light-enhanced atom interferometry below the standard quantum limit", Phys. Rev. A 90, 063630 (2014).

[40] J. Suh, A. J. Weinstein, C. U. Lei, E. E. Wollman, S. K. Steinke, P. Meystre, A. A. Clerk, and K. C. Schwab, "Mechanically Detecting and Avoiding the Quantum Fluctuations of a Microwave Field", Science 344, 1262 (2014).

Online sources:

[41] Toptica DLpro specifications (November 3, 2015): http://www.toptica.com/products/research_grade_diode_lasers/tunable_diode_lasers/the_ultimate_tunable_diode_laser_dl_pro.html.

[42] Toptica DL100 specifications (November 3, 2015): http://www.toptica.com/products/research_grade_diode_lasers/tunable_diode_lasers/tunable_diode_lasers_370_nm_1770_nm_dl_100.html.

[43] Cesium D-line data by D. A. Steck (revision 2.1.4, December 23, 2010): http://steck.us/alkalidata.